Time-resolved study of solidification phenomena on pulsed-laser annealing of amorphous silicon

TIME-RESOLVED STUDY OF SOLIDIFICATION PHENOMENA ON PULSED-LASER ANNEALING OF AMORPHOUS SILICON

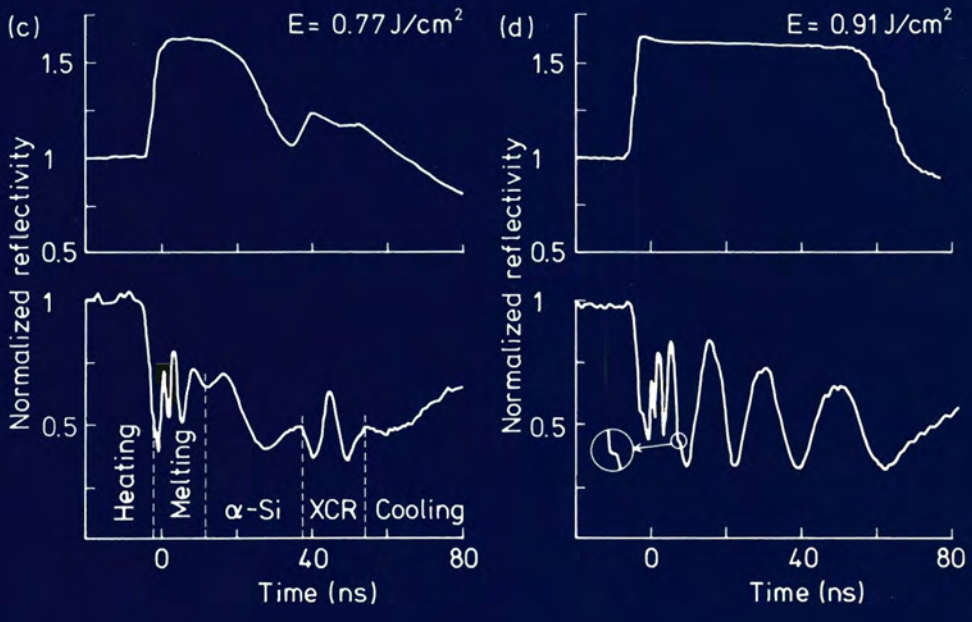

JOHANNES JOSEF PANCRASIUS (JOOP) BRUINES

TIME-RESOLVED STUDY OF SOLIDIFICATION PHENOMENA ON PULSED-LASER ANNEALING OF AMORPHOUS SILICON

proefschrift

ter verkrijging van de graad van doctor aan de Technische Universiteit Eindhoven, op gezag van de Rector Magnificus, prof. ir. M. Tels, voor een comissie aangewezen door het College van Dekanen in het openbaar te verdedigen op dinsdag 25 oktober 1988 te 16.00 uur

door

JOHANNES JOSEF PANCRASIUS (JOOP) BRUINES

geboren te Alphen aan den Rijn

Dit proefschrift is goedgekeurd door de promotoren

prof. dr. J. Wolter en prof. dr. F.W. Saris

Copromotor dr. Q.H.F. Vrehen

The work described in this thesis was performed at the Philips Research Laboratories, Eindhoven, The Netherlands

Cover: Time-resolved reflectivity measurements from the front (upper curves) and the rear (lower curves) on pulsed-laser annealing of 440 nm amorphous silicon on 60 nm crystalline silicon on sapphire. See also figure III.21.

Aan mijn ouders, Janneke,
Bram en Annelies

CONTENTS:

Parts of this thesis have been published in the following papers:

Pulsed-laser melting of amorphous silicon on glass: time-resolved reflectivity measurements, J.J.P. Bruines, R.P.M. van Hal, H.M.J. Boots, and J. Wolter
in *Energy – Beam Solid Interaction and Transient Thermal Processing* edited by V.T. Nguyen and A.G. Cullis (Les editions de physique, Les Ulis Cedex, 1986), pages 525-529.

Direct observation of resolidification from the surface upon pulsed-laser melting of amorphous silicon, J.J.P. Bruines, R.P.M. van Hal, H.M.J. Boots, W. Sinke, and F.W. Saris
Applied Physics Letters **48**(19), pages 1252-1254 (1986).

Time-resolved reflectivity measurements during explosive crystallization of amorphous silicon, J.J.P. Bruines, R.P.M. van Hal, H.M.J. Boots, A. Polman, and F.W. Saris
Applied Physics Letters **49**(18), pages 1160-1162 (1986).

Subsurface extension of explosive crystallization, M.P.A. Viegers, B.H. Koek, J.J.P. Bruines, R.P.M. van Hal, and H.M.J. Boots
Proceedings of the XIth Congres on Electron Microscopy, pages 1521-1522 (1986).

Between explosive crystallisation and amorphous regrowth: inhomogeneous solidification upon pulsed-laser annealing of amorphous silicon, J.J.P. Bruines, R.P.M. van Hal, B.H. Koek, M.P.A. Viegers, and H.M.J. Boots
Applied Physics Letters **50**(9), pages 507-509 (1987).

The transition between explosive crystallization and amorphous regrowth, J.J.P. Bruines, R.P.M. van Hal, B.H. Koek, M.P.A. Viegers, and H.M.J. Boots
Materials Research Society Symposium Proceedings **74**, pages 91-102 (1987).

GLOSSARY

α-Ge	amorphous Germanium
α-Si	amorphous Silicon
c-Si	crystalline Silicon
cw	continues wave
EDX	Energy Dispersive X-ray (analysis)
FG	Fine Grain
FWHM	Full Width at Half Maximum
HRP	High Reflectivity Plateau
HTEM	High-resolution Transmission Electron Microscopy
LG	Large Grain
LRP	Low Reflectivity Plateau
l-Si	liquid Silicon
p-Si	polycrystalline Silicon
RBS	Rutherford Backscattering Spectroscopy
SE	Static Ellipsometry
SI	Static Reflectivity
SPE	Solid Phase Epitaxy
TEM	Transmission Electron Microscopy
TC	Transient Conductivity
TRE	Time-Resolved Ellipsometry
TRR (-F, -R)	Time-Resolved Reflectivity (Front, Rear)
XCR	Explosive CRrystallization

I. INTRODUCTION

I.1. General Overview

Soon after its invention in 1960, the laser was used in materials processing. At first the applications were rather gross such as welding, cutting and drilling of metals and ceramics. Later on its applicability became more sophisticated and laser irradiation was introduced in the fields of integrated circuit processing, materials engineering, and optical data storage.

One of the steps in the fabrication of integrated circuits, "chips", is the implantation of silicon with a so called dopant to obtain its desired electrical conductivity properties. For that purpose, elements like phosphorus, arsenic, boron or aluminium are injected at great speed into the silicon. After this process the silicon has to be annealed, i.e. heated, both to electrically activate the implanted species and to repair the crystal, damaged by the bombardment. The conventional method of annealing is by heating the sample in a furnace to $\simeq$1000 °C for times on the order of tens of minutes. This has the drawback that the complete silicon wafer, with all its circuits, is heated to this temperature. Such a procedure imposes heavy constraints on the thermal stability of all previously executed process steps. The great advantage of pulsed-laser annealing is that it can be applied locally ($\simeq 1\ \mu m^2$) and that the energy is absorbed in a thin surface layer ($<1\ \mu m$). This implies that the implanted region can reach very high temperatures, or even melt, without significant heating of the surrounding area and underlying material. Therefore, this process has been studied extensively. It has been shown that a single laser pulse of the appropriate wavelength can remove all damage, a feature unsurpassed by furnace annealing. This can only be achieved by the consecutive melting and epitaxial growth of the damaged area. Unfortunately, most dopants are fast diffusers in liquid silicon thus the initial implantation profile ($\simeq$ Gaussian) will be altered after this process. The redistribution is often tolerable, however, for very short melt durations ($\ll$100 ns), obtainable with fast laser pulses ($\simeq$10 ns). On the other hand, fast laser pulses give high solidification velocities resulting in amorphization instead

of epitaxial growth. It is clear that a thorough understanding of the kinetics of melting and solidification upon pulsed-laser irradiation is essential in this case.

Not long after the first application of lasers, it was noticed that metals, when melted by a laser, often exhibited unusual properties. This resulted in an intensive study of the engineering of materials by means of lasers. Irradiation by fast light pulses can lead to heating and cooling rates several orders of magnitude higher than obtainable by conventional methods. The high heating rates make it possible to bring a solid to a temperature above its melting point or to melt an amorphous material, which would normally have crystallized long before. When melted, the high cooling rates can freeze-in the disorder of the liquid state, producing amorphous material. In this way it is possible to fabricate amorphous alloys with compositions which are only obtainable in the liquid phase, not in the solid. By choosing the right materials and the right composition, materials can be engineered to have less wear, less friction, greater hardness or superior corrosion resistance. The same properties can sometimes be obtained by implantation of metals with e.g. carbon or nitrogen. Just as with silicon, the implantation damage can be removed by means of laser annealing. Again it is necessary to understand the processes of melting and solidification in order to make new, superior materials.

The field of optical data storage is rather new. With the techniques now available, huge amounts of data (10 Giga bit = 500.000 A4 pages) can be stored on a disk with a diameter of an LP record. Present commercial systems are all of the write-once type. Information is written into the medium by melting it, thus making little dents which can not be removed. However, the process is not well controlled and does not work in the presence of a surface coating, which is needed to keep away the dust and protect the recording layer from scratches. Moreover, it will be clear that an erasable medium would open the computer market completely, enlarging the scope of the product enormously. Both requirements can be met when using so called phase change optical recording. In this concept the data is recorded by changing the phase of the medium between the amorphous and the crystalline state. To be able to select the right materials and the right experimental conditions for this application, it is of great impor-

tance to know what is happening during melting and solidification on pulsed-laser irradiation.

The application areas of pulsed-laser irradiation described above all showed the need for a better understanding of the dynamics of phase changes. This thesis reports on a study of the melting and solidification behaviour of silicon on pulsed-laser irradiation. Silicon is the prime material of integrated circuit technology and, in principle, offers the possibility for phase change optical recording. Moreover, it is an ideal model system, consisting of one element only.

The structure of this thesis is the following. Chapter I continues with the statement of the problem, giving the basic experimental observations and models found in literature. This section is succeeded by the presentation of the relevant optical and thermophysical constants of silicon. The chapter ends with a description of the kinetic theory for phase changes, introducing the concepts of superheating/undercooling and nucleation from a metastable phase.

The description of the experimental set-up in chapter II is divided into four sections. The first section deals with the elements for pulsed-laser melting. Next we describe the optical and electronical set-up to record the reflectivity in real-time. The fourth and last section presents the preparation and characterization of the amorphous silicon samples used.

The third chapter starts with the presentation of our conceptual framework describing the importance of the various experimental parameters and their consequences. The remaining part is devoted to the presentation of the bulk of the experimental data. Firstly we describe the experiments which initially show amorphous regrowth from both the interior and the surface. The results allow us to draw several conclusions concerning the influence of impurities, laser pulse duration, and amorphous silicon thickness on this solidification scheme. Moreover, it is shown that amorphous regrowth can be followed by explosive crystallization. Secondly we present the data on explosive crystallization. The time-resolved reflectivity results indicate the formation of crystalline nuclei before the melting of the amorphous material.

Chapter IV is devoted to the simulation of the phase changes in amorphous and crystalline silicon, evoked by a laser pulse. It contains a description of the basic elements of heat-flow calculations and the incorporation of superheating/undercooling, amorphous regrowth, and crystallization into the heat-flow concept. Moreover, we discuss the merits of a computer program describing explosive crystallization, which was presented to us by Wood and Geist.

The final chapter gives the synthesis of the experiments described in chapter III and the simulations introduced in chapter IV. The comparison between the various experimental observations and the computer simulations enables us to draw several conclusions concerning the proposed mechanisms for amorphous regrowth and explosive crystallization in amorphous silicon. A summary of the conclusions appears at the end of the chapter.

1.2. The Statement of the Problem

The melting and solidification behaviour of amorphous and crystalline Si upon pulsed-laser irradiation has shown many interesting phenomena. These phenomena are related with phase change kinetics as well as with differences in the melt temperature and latent heat between amorphous and crystalline Si. When (100) crystalline Si (c-Si) is melted by a short light pulse such that the rate of cooling is high enough to force the solidification front to move at a velocity >15 m/s, normal epitaxial growth can no longer take place and amorphous Si (α-Si) is formed instead (Thompson and Galvin, 1983; Thompson et al. 1983). The melting point reduction and decrease of the latent heat at the solid-liquid transition, both with respect to c-Si, play an important role in the case of α-Si (Bagley and Chen, 1979; Thompson et al. 1984; Donovan et al, 1985; Thompson et al. 1985; Sinke et al. 1988). Because of these features α-Si can show explosive crystallization (XCR).

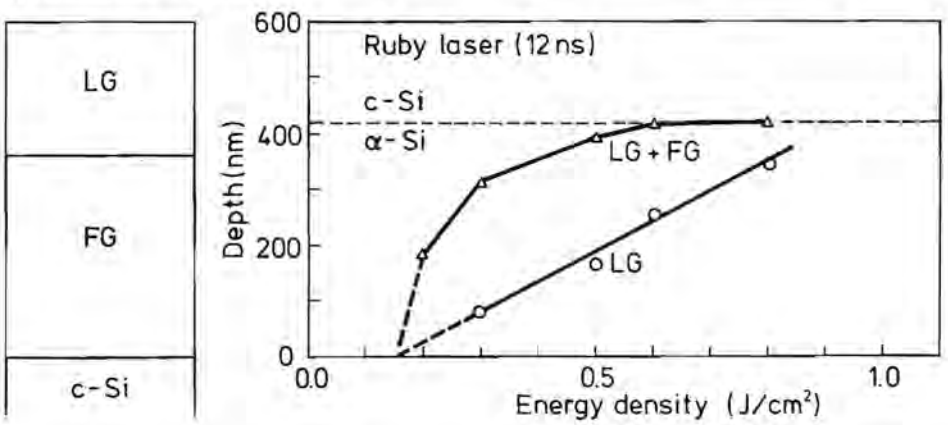

Figure 1.1. Schematic representation of the observed microcrystalline regions after in-depth XCR of ≃400 nm α-Si on c-Si and the corresponding relation between the thicknesses of the LG and FG p-Si layers as a function of energy-density, after Narayan and White (1984).

XCR of amorphous materials has been known since the last century (Gore, 1855). Recently, the process has shown a revival of interest with the advent of the laser processing of α-Ge and α-Si. The propagation of XCR has been studied

both for the planar (Chapman et al. 1980; Leamy et al. 1981; Wagner et al. 1986) and the normal direction to the surface. In the rest of this thesis we will discuss only the type of XCR perpendicular to the sample's surface (in-depth). Transmission electron microscopy (TEM) images, taken after XCR, revealed the existence of two distinct microcrystalline regions: large grain polycrystalline Si (LG p-Si) at the surface with fine grain (FG) p-Si material underneath (Cullis et al. 1980; Narayan and White, 1984; Narayan et al. 1984; Bartsch et al. 1986). The thickness of the LG p-Si layer corresponded roughly with the melt depth as calculated without XCR. The FG p-Si layer exhibits a large increase in thickness for laser energy-densities just above the threshold for melting, after which it saturates at the c-Si interface, see figure I.1.

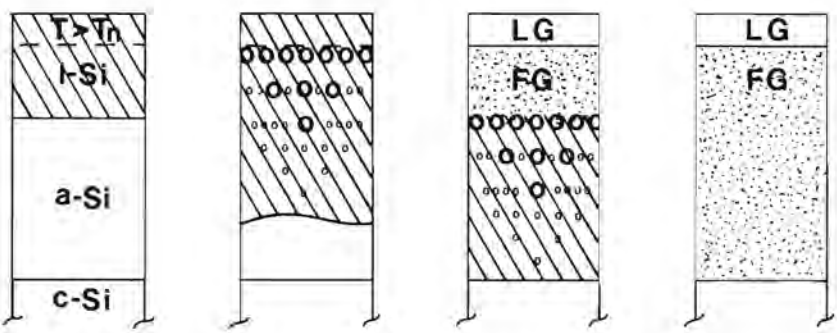

Figure I.2. Schematic drawing of the model for XCR as proposed by Wood et al. (1984). There is no clear interface between the solid and the expanding liquid because of the c-Si nuclei.

Figure I.2 schematically shows the model proposed by Wood and coworkers (1984) to explain the observed microcrystalline regions and extended melt depth. Melted α-Si forms an undercooled liquid in which homogeneous nucleation of c-Si occurs for temperatures below a critical value T_n. In this way the FG p-Si is thought to be formed even during melt-in. The release of latent heat by this process is responsible for the larger melt front penetration. The LG p-Si then grows on top of the already present FG p-Si thus taking up the space where the temperature of the liquid Si (l-Si) has been higher than T_n. However, based on undercooling experiments on l-Si droplets, Devaud and Turnbull

(1985) showed that homogeneous nucleation is highly unlikely except for l-Si temperatures appreciably below the melting point of α-Si.

Measurements of the transient conductivity (TC) and the time-resolved reflectivity (TRR) by Thompson et al. (1984) prompted them to suggest a different scheme, pictured in figure I.3.

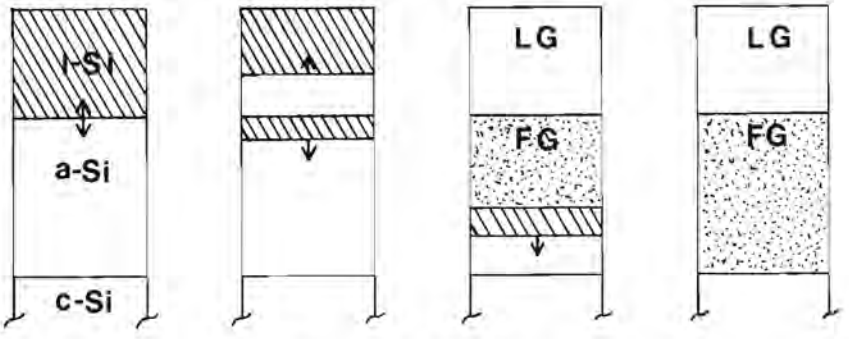

Figure I.3. The model for XCR proposed by Thompson and coworkers (1984) based on their TRR and TC measurements. In contrast with the scheme from Wood et al. (1984), see figure I.2, there is a well defined self-propagating l-Si layer moving towards the c-Si substrate.

The absorbed laser energy first melts an α-Si layer at the surface, the so called primary melt. This l-Si layer starts to solidify as LG p-Si from the primary melt depth towards the surface and the latent heat released by this solidification melts a thin layer of the underlying α-Si. Latent heat is again released during crystallization of this secondary melt and thus a thin l-Si layer moves from the primary melt depth to the interior of the sample. This self-propagating melt is quenched either at the substrate or when the latent heat released upon crystallization becomes smaller than needed to heat and melt the α-Si. This so called secondary melt is assumed to produce FG p-Si as a result of its greater undercooling with respect to the primary melt. Experimental evidence for the existence of such a self-propagating l-Si layer has been given by Rutherford backscattering spectroscopy (Sinke and Saris, 1984) and TRR measurements (Lowndes et al. 1986; Bruines et al. 1986c). The Rutherford backscattering spectroscopy (RBS) results after XCR showed two peaks of segregated impurities: one in the interior of the sample corresponding to accumulation at the

self-propagating l-Si layer, and one at the surface connected with the upward moving solidification front of the primary melt, see figure I.4.

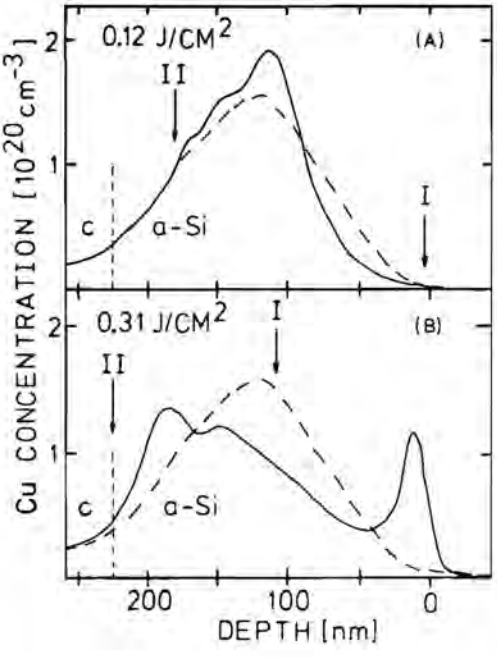

Figure I.4. RBS impurity redistribution profiles after XCR upon irradiation of 225 nm, Cu implanted α-Si with 32 ns FWHM pulses from a ruby laser at (A) 0.12 and (B) 0.31 Jcm^{-2} (after Sinke and Saris, 1984). The primary (I) and secondary (II) melt depths can be inferred from a comparison between the redistributed (full line) and the as-implanted (dashed line) profile.

From interferences in the TRR measurements, the position and velocity of the XCR front could be determined. Wood et al. (1986a, 1986b) published computer simulations of the XCR process based on the model proposed by Thompson et al. (1984), thereby implicitly abandoning their idea of homogeneous nucleation. From a theoretical point of view, however, very little is known about the fundamentals of XCR. As already mentioned, it is very unlikely that homogeneous nucleation is the force behind XCR. The model by Thompson et al. (1984), supported by much experimental evidence, does not explain how and

when the XCR process is nucleated from the primary melt. We suggested the possibility of nucleation at the l-Si / α-Si interface based on experimental results (Bruines et al. 1987a, 1987b). Tsao and Peercy (1987) have published theoretical work on this subject indicating that nucleation of p-Si at a moving l-Si / α-Si interface could result in FG p-Si. Unfortunately, it remains unclear how the difference between LG and FG p-Si comes about. Recently, experiments by Roorda et al. (1988) suggested that XCR could be initiated by nuclei which are formed in the solid phase. Their observed grain density corresponds with that of LG p-Si. The much larger grain density found in FG p-Si is explained by a tentative stabilization of sub-critical nuclei at the liquid-solid interface.

XCR is not the only phenomenon which can occur upon pulsed-laser irradiation of α-Si. From the existence of one sharp impurity band buried below the surface, Cullis et al. (1982, 1984) and Campisano et al. (1985) concluded that amorphous regrowth can occur from both the interior liquid-solid interface and the surface. They proposed that solidification starts at the interior. In view of the growth of α-Si there and the melting point depression for high impurity concentrations, the remaining l-Si is thought to become so undercooled that amorphous growth from the surface can occur, see figure I.5.

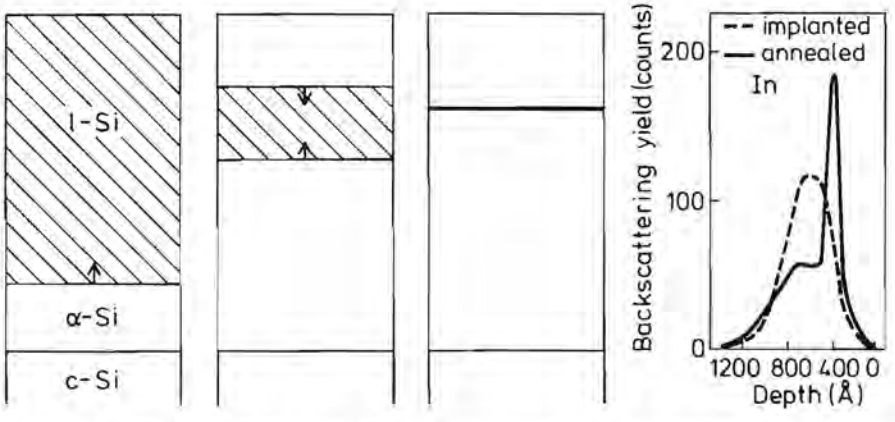

Figure I.5. Growth of α-Si from both the interior and the surface: In redistribution profile indicating this process (after Campisano et al. 1985) and a schematic picture of the model for amorphous regrowth proposed by Cullis et al. (1982).

The process of growth from the surface has been confirmed by TRR measurements (Bruines et al. 1986b; Peercy et al. 1986a). The total absence of p-Si, however, can only be positively determined by TEM. In practice this means that it is verified for a few but not all energy-densities. Moreover, the presence of In can hamper the formation of p-Si. Olson (1985) presented results on continuous wave (cw) laser irradiation of α-Si showing solid phase epitaxy (SPE), and no melting, for deduced temperatures up to 1635 K, 50 K below the melting point of c-Si. In a more recent article, Olson and coworkers (1987) reported SPE or random crystallization dominated SPE for "thin" (≃100 nm) α-Si layers, irradiated on a microsecond time scale. However, in contrast with their cw-laser results, they find the melting of "thick" (≃260 nm) α-Si samples at ≃1463 K, in agreement with the 1465±25 K determined by Thompson et al. (1985). Raman measurements by Sinke et al. (1988) suggest that the apparent melting temperature of α-Si depends on the method and rate of heating.

Results showing both p-Si formation and amorphous regrowth have also been presented. Narayan (1986) correlated the various solidification phenomena with the local energy-density across a laser spot with a Gaussian intensity profile. We observed the same mixed behaviour but now with an essentially uniform energy-density profile indicating that solidification can have a random nature under certain circumstances (Viegers et al. 1986; Bruines et al. 1987a). This signifies that care must be taken with an interpretation of the solidification phenomena based on local observations as done by Narayan (1986).

The presence of impurities, often used as an implant to amorphize c-Si, affects melting and solidification. Low concentrations (≃0.1 at.%) of insoluble elements (In,Zn,Au) and high concentrations (≃10 at.%) of soluble species (As,P,B) in c-Si can give a considerable melting point depression (Thompson and Peercy, 1986). The effect of these impurity concentrations on the melting temperature of α-Si is unclear. However, Jacobson et al. (1987) found that the solubility of Au in α-Si is $\simeq 10^{20}$ cm^{-3}, a factor 10^6 higher than in c-Si. Moreover, Peercy et al. (1986b) reported the nucleation of an internal melt during pulsed-laser annealing, resulting from a local melting point depression, for In concentrations >100 times higher than its solubility limit in c-Si. These results indicate

that the effect of impurities on the melting temperature of α-Si is probably less severe than for c-Si. Impurities can have a large effect on the growth of c-Si. Cullis et al. (1982, 1984) and Narayan (1986) have observed that epitaxial growth can be frustrated if the concentration of impurities, segregated at the liquid-solid interface, becomes too high. Recently, Roth and Olson (1987) observed that impurities such as P, As, and B all decrease the nucleation rate but increase the growth velocity of c-Si nuclei in α-Si. The opposite effect was found for O and F. A SPE rate increase by a factor of 2 was found for an In concentration of ≃0.3 at.%, ten times as high as the solubility limit in c-Si (Nygren et al. 1987). At higher In concentrations (>0.5 at.%) they observed an amorphous to polycrystalline transformation at temperatures much lower than required for SPE. Based on these last results they estimate a melting point depression for α-Si of ≃30 K per at.% In.

Many different melt and solidification phenomena have been observed under as many different experimental conditions. In this thesis we try to bring some order in the experimental multitude of melt and solidification phenomena upon pulsed-laser irradiation of implantation amorphized Si. To achieve this goal we performed TRR, RBS, and TEM measurements on Cu and Si implantation amorphized Si of various layer thicknesses, irradiated with light pulses from two different lasers and with various pulse durations to make a systematic study of the influence of the experimental conditions on the multitude of melt and solidification processes observed in α-Si. The experimental results are accompanied by heat-flow calculations of the melt depth and melt velocity, to enhance and support their understanding. Moreover, we present two new computer models, one dealing with amorphous regrowth from the surface and one to test the validity of heterogeneous nucleation as a mechanism for XCR (Tsao and Peercy, 1987). The latter one is compared with the model from Wood and Geist (1986a, 1986b), followed by a discussion on the merits and failures of the two models.

I.3. Properties of Silicon

I.3.1 Introduction

Silicon is an element which in its various phases combines the properties of many others. Solid crystalline silicon (c-Si) is a semiconductor and has the optical and thermophysical properties of an insulator. Liquid silicon (l-Si) behaves like a metal with all the corresponding features as a high optical reflectivity and a good thermal and electrical conductivity. Recently, yet another solid phase of silicon has been found to exist. Unlike other materials, silicon does not form a glassy state when rapidly solidified from the melt. Instead it assumes an amorphous phase with a lowered melting temperature and latent heat. In this phase the electrical conductivity of the silicon is still that of a semiconductor but the thermal conductivity has dramatically decreased and shows the behaviour of a glass. When α-Si is melted, the thus formed undercooled liquid behaves like a metal but is, of course, unstable against crystallization.

In order to interpret and to understand the various phenomena which occur upon pulsed-laser irradiation of silicon it is of crucial importance to know the optical and thermal properties of silicon accurately. Furthermore it is necessary to look into the theory of melting and solidification. The experiments performed on amorphous silicon (α-Si) and its undercooled liquid state prompted further theoretical work to describe solidification under non-equilibrium conditions.

The remaining part of this chapter is divided into three sections. In the first section, the optical properties of crystalline, amorphous, and liquid silicon will be presented as a function of wavelength and temperature. The second section is devoted to the relevant thermophysical properties. Finally, the third section goes into the processes of melting and solidification.

I.3.2 Optical properties of silicon

The optical properties of a material are usually given in terms of the complex dielectric constant $\varepsilon = \varepsilon_1 + i\varepsilon_2$ or as the refractive index n and the extinction coefficient k. The two different representations are related by:

$$\varepsilon_1 = n^2 - k^2 \tag{1a}$$

$$\varepsilon_2 = 2nk \tag{1b}$$

Under experimental conditions, other optical parameters such as the absorption coefficient α and the reflectance R are of more direct use. The absorption coefficient represents the absorptive power of a material and is related to the extinction coefficient k in the following way:

$$\alpha = \frac{2\pi}{\lambda}\varepsilon_2 = \frac{4\pi k}{\lambda} \tag{2}$$

wherein λ is the wavelength of the light in vacuum.

The reflectance R is the ratio between the reflected and the incident intensity at a boundary between two media. Given the optical parameters of the two materials, the reflectance depends on both the polarization and the angle of incidence of the incoming light:

$$R\| = \frac{(n_2 \cos\theta_i - n_1 \cos\theta_t)^2 + (k_2 \cos\theta_i - k_1 \cos\theta_t)^2}{(n_2 \cos\theta_i + n_1 \cos\theta_t)^2 + (k_2 \cos\theta_i + k_1 \cos\theta_t)^2} \tag{3a}$$

$$R\perp = \frac{(n_1 \cos\theta_i - n_2 \cos\theta_t)^2 + (k_1 \cos\theta_i - k_2 \cos\theta_t)^2}{(n_1 \cos\theta_i + n_2 \cos\theta_t)^2 + (k_1 \cos\theta_i + k_2 \cos\theta_t)^2} \tag{3b}$$

with: $R\|$ = reflectance for the polarization parallel to the plane of incidence

$R\perp$ = reflectance for the polarization perpendicular to the plane of incidence

n_1 and k_1 = optical constants of medium 1 (incoming light)

n_2 and k_2 = optical constants of medium 2 (transmitted light)

θ_i = angle between incoming light and the surface's normal

θ_t = angle between transmitted light and the surface's normal

The angle of incidence and transmission are related to the refractive indices of media 1 and 2 by Snell's law:

$$\frac{\sin\theta_i}{\sin\theta_t} = \frac{n_2}{n_1} \tag{4}$$

For normal incidence at an air-material boundary the equations 3(a + b) reduce to one simpler, and well known expression:

$$R\| = R\perp = \frac{(n_2 - 1)^2 + k_2^2}{(n_2 + 1)^2 + k_2^2} = R_n \tag{5}$$

The optical properties of crystalline silicon have been extensively studied by scanning ellipsometry techniques (Aspnes and Theeten, 1980; Jellison and Modine, 1982a, 1982b, 1983; Jellison and Burke, 1986). C-Si is an indirect-gap semiconductor and its optical properties vary substantially with wavelength and temperature. The dependence of n and k on the photon energy is a complicated function of parameters related to the band structure of silicon. Therefore, no sensible approximation formula can be given. The influence of temperature on the optical properties is less capricious, and it is possible to use empirical relations. For photon energies well below the direct gap of silicon (3.4 eV) and for temperatures between 300 K and 1000 K, the absorption coefficient can be fitted by:

$$\alpha(\lambda, T) = \alpha_0(\lambda)\, exp(T/T_0) \tag{6}$$

with $T_0 \simeq 430$ K. The refractive index increases linearly with temperature for photon energies from 2 eV to 3 eV:

$$n(\lambda, T) = n(\lambda, 300\ K) + 5 \times 10^{-4}\ \mathrm{K}^{-1}\ (T - 300\ \mathrm{K}) \tag{7}$$

A compilation of the relevant optical parameters of c-Si for the different wavelengths used in this thesis is given in table I (Jellison and Modine, 1982a, 1982b).

Amorphous silicon has also been studied by many authors (McGill et al. 1970; Adams and Bashara 1975; Watanabe et al. 1979; Cortot and Ged 1982; Lue and Shaw 1982; Ravindra and Narayan 1986; White 1986). The documentation of the optical properties of α-Si is complicated by the fact that these often vary with the sample fabrication. For example, Fredrickson et al. (1982) reported that the optical properties of ion-implanted α-Si change upon heat treatment. They observed that the infrared refractive index saturates at ≃96 % of

λ(nm)	laser	n	k	α(cm^{-1})	R_n	α_0(cm^{-1})	T_0(K)
820	AlGaAs	3.586	0.003	4.6×10^2	.318	2.3×10^2	430
694	Ruby	3.763	0.013	2.4×10^3	.336	1.3×10^3	427
647	Krypton ion	3.827	0.015	3.0×10^3	.343	1.4×10^3	430
633	Helium-Neon	3.866	0.018	3.6×10^3	.347	2.1×10^3	447
532	$2\nu_0$ Nd:YAG	4.153	0.038	9.0×10^3	.374	5.0×10^3	430
488	Argon ion	4.356	0.064	1.6×10^4	.392	9.1×10^3	438

Table I. Optical constants of c-Si for the wavelenghts used in this thesis.

its as-implanted value after 2 hours at 500 °C or 30 minutes at 550 °C. In this section we only discuss the optical constants of as-implanted ion-implantation amorphized silicon since this is the material we have been working with. As already mentioned in the introduction to this chapter, α-Si is still a semiconductor. The absence of long-range order however means that the sharp features of the band structure are smeared out in energy. As a result of this, both n and k are increased for photon energies below the direct band gap. The absorption coefficient α is no longer a strong function of temperature as with c-Si. There is some evidence that it increases to a value between that of l-Si and "cool" α-Si for temperatures just below the melting point (Bruines et al. 1986b). The reflectance of α-Si for the ruby laser wavelength ($\lambda = 694$ nm) was measured by Webber et al. (1983) and showed little temperature dependence up to 800 K. Table II gives the optical data for α-Si at the relevant wavelengths (White, 1986).

With the advent of laser annealing and the computer modelling thereof, it became increasingly important to know the optical functions of l-Si. The first static measurements were performed by Sharev et al. (1975, 1977). The results for n and k can be fitted by straight lines:

$$n = -0.2 + 4.8 \times 10^{-3} \lambda\,(\text{nm}) \tag{8a}$$

$$k = 2.3 + 4.7 \times 10^{-3} \lambda\,(\text{nm}) \tag{8b}$$

λ(nm)	laser	n	k	$\alpha(cm^{-1})$	R_n
694	Ruby	4.547	0.542	9.8×10^4	.414
647	Krypton ion	4.642	0.771	1.5×10^5	.427
633	Helium-Neon	4.633	0.833	1.7×10^5	.428
532	$2\nu_0$ Nd:YAG	4.758	1.339	3.2×10^5	.456
488	Argon ion	4.738	1.694	4.4×10^5	.470

Table II. Optical constants for α-Si at selected wavelengths.

They also found that the optical properties of l-Si are not very temperature dependent. This is in agreement with the data from Lampert et al. (1981), indicating a temperature coefficient of -0.02 %/K up to $\simeq$1870 K for the reflectance at $\lambda = 633$ nm. Recently, Jellison and Lowndes (1985) and Jellison et al. (1986) performed time-resolved ellipsometry and time-resolved reflectivity measurements during pulsed-laser annealing of Si and Ge. The so obtained optical constants did not show a significant difference with the data from Sharev et al. (1975, 1977). Since the electronic structure of melted α-Si was shown to be the same as that of melted c-Si (Murakami et al. 1986), there is no difference between the optical constants of the two molten states. The resulting parameters of l-Si as calculated from the equations 8(a + b) are presented in table III.

I.3.3 Thermophysical properties of silicon

The relevant thermophysical properties of silicon can be divided into two classes. Firstly the melt point T_m and latent heat L_h, and secondly the thermal conductivity κ and specific heat C_p. The first two parameters depend only on the phase, the other two depend also on temperature. When going from room temperature to the melting point of c-Si, the specific heat increases by a factor of nearly two and the thermal conductivity decreases to only one sixth of its original value. The specific heat of α-Si differs only slightly from that of c-Si, however, the thermal conductivity is drastically reduced and does not show any

λ(nm)	laser	n	k	$\alpha(cm^{-1})$	R_n
820	GaAlAs	3.7	6.2	8.4×10^5	.76
694	Ruby	3.1	5.6	1.0×10^6	.74
647	Krypton ion	2.9	5.3	1.0×10^6	.73
633	Helium-Neon	2.8	5.3	1.1×10^6	.73
532	$2\nu_0$ Nd:YAG	2.4	4.8	1.1×10^6	.73
488	Argon ion	2.1	4.6	1.2×10^5	.72

Table III: Optical constants for l-Si at selected wavelengths based on the equations 8(a + b).

significant temperature dependence. Both the thermal conductivity and the specific heat show a jump when going from the solid to the liquid state. These properties of l-Si are similar to that of metals and thus are not very sensitive to temperature.

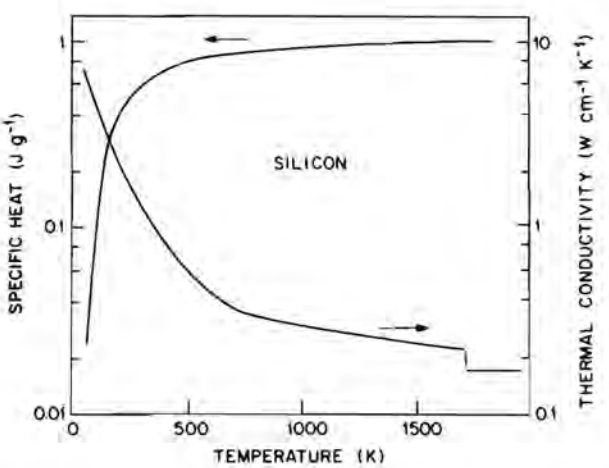

Figure I.6. Specific heat and thermal conductivity of c-Si as a function of temperature (Baeri and Campisano, 1982).

The thermophysical properties of c-Si can be found in several handbooks (Goldsmith et al. 1961; Touloukian and Boyco 1970; Touloukian et al. 1970).

The melting point of c-Si is 1685 K, although slight variations around this value can be found in literature. The latent heat amounts 4.2×10^9 Jm^{-3}. The specific heat of c-Si is reasonably described by the Debye law with a Debye temperature of 645 K (Kittel 1976a). For the temperature range from 300 K to the melting point, it can be fitted by a power law:

$$C_p = 6.33 \times 10^5 \ \mathrm{JK^{-1.18}m^{-3}} \ T^{0.18} \tag{9}$$

The specific heat and thermal conductivity of c-Si are shown in figure I.6 as a function of temperature. At this point it is interesting to compare the energy needed to bring c-Si from room temperature to the melting point with its latent heat. The integral over the specific heat C_p gives $\simeq 3.5 \times 10^9$ Jm^{-3} , which is about 83 % of the value for the latent heat. So for c-Si, heating and melting take about the same amount of energy.

To a first approximation, the thermal conductivity is expected to vary as 1/T for high temperatures since the collision frequency for phonons is proportional to their total number, which scales with T (Kittel 1976a; Ashcroft and Mermin 1976). This does not, however, give a satisfactory fit with the data at room temperature where the full Bose-Einstein expression for the phonon occupation number must be used. A much better result can be obtained using an exponentially decaying function with saturation:

$$\kappa = 22 + 382 \, exp(-T/240 \ K) \ \mathrm{Wm^{-1}K^{-1}} \tag{10}$$

Since α-Si is a metastable phase, it is not easy to determine its thermophysical properties. To avoid crystallization during the measurement of thermophysical properties, much work has been done using pulsed-lasers. The melting point and the latent heat are the most difficult to obtain (Bagley and Chen 1979; Spaepen and Turnbull 1979; Baeri et al. 1980; Webber et al. 1983; Thompson et al. 1984; Donovan et al. 1985; Thompson et al. 1985). Moreover, there is some evidence that they depend on the method and rate of heating (Sinke et al. 1988). The most accurate value for the melting temperature of α-Si, obtained in the nanosecond pulse regime, is 1460±25 K (Thompson et al. 1985). The best value for the latent heat is given by Donovan et al. (1985);

3.08×10^9 Jm^{-3}. A first well considered estimate for the thermal conductivity of α-Si was given by Webber et al. (1983). Based on the Debye kinetic theory they calculated a value on the order of 1 Wm^{-1}K^{-1}. Goldsmid et al. (1983) measured 2.6 Wm^{-1}K^{-1} and pulsed-laser experiments by Lowndes et al. (1984) indicated 2 Wm^{-1}K^{-1}. All values given are at least an order of magnitude beneath those of c-Si. There is no data available on the possible temperature dependence of the thermal conductivity, but according to Webber et al. (1983), only minor corrections can be expected. The difference between the specific heat of the crystalline and the amorphous phase of α-Ge has been determined by Chen and Turnbull (1969). The result can also be used for α-Si when scaled with the melting temperature of c-Si instead of that of c-Ge (Donovan et al. 1985):

$$\Delta C_{p,ac} = -1.86 \times 10^4 + 236\,(T/1685\ K)\ \mathrm{Jm^{-3}K^{-1}} \qquad (11)$$

If we compare the energy to heat α-Si and to actually melt α-Si we find nearly the same result as with c-Si. The integral over the specific heat is lowered to $\simeq 2.9 \times 10^9$ Jm^{-3}, mainly because of the lower melting point. This value is equivalent to 94 % of the latent heat. The energy needed to both heat and melt α-Si is about 78 % of that of c-Si. This means that, neglecting effects of the much smaller heat diffusion, α-Si will always melt more deeply as compared with c-Si under irradiation with the same laser pulses.

The thermal conductivity and specific heat of l-Si are not know. The usual way of compensating for this lack of knowledge is to use the fact that l-Si is a metal. In that case the thermal conductivity can be related to the electrical conductivity σ by the Wiedemann-Franz law (Kittel 1976b):

$$\kappa = 2.45 \times 10^{-8}\ \mathrm{W\Omega K^{-2}}\ \sigma T \qquad (12)$$

Measurements of Glasov et al. (1969) give a value of 1.25×10^6 Ω^{-1}m^{-1} for σ with a small increase with temperature. Together with the result of eq. 12 this leads to:

$$\kappa = 47\,(T/1685\ K)\ \mathrm{Wm^{-1}K^{-1}} \qquad (13)$$

The only data on the specific heat of l-Si is given by Hultgren et al. (1973). They argued that the specific heat would be $\simeq$10% lower than the value for c-Si.

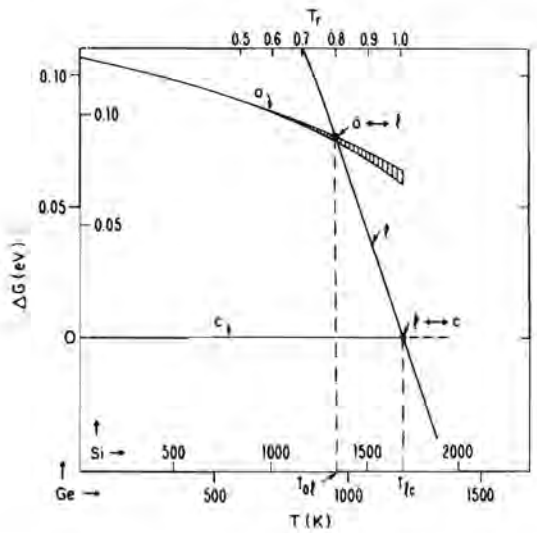

Figure I.7. Gibbs free energy differences, in eV/atom, for the amorphous (a), the liquid (l), and the crystalline (c) phase, for Si (inner scale) and Ge (outer scale) after Spaepen and Turnbull (1982).

In pulsed-laser annealing a small volume of material is subsequently energized and quenched. Usually the rate of heating and cooling is so high that departures from equilibrium become appreciable. For example when (100) c-Si is melted by picosecond light pulses, the rate of cooling will be so high that normal crystalline growth cannot take place and α-Si is formed instead; the l → a transition in figure I.7. The critical velocity for this phenomenon was shown to be 15 m/s (Thompson and Galvin, 1983; Thompson et al. 1983). An even more intriguing situation is encountered in the pulsed-laser annealing of α-Si . When heated on a microsecond timescale α-Si cannot be melted. Instead it either grows epitaxially on a c-Si substrate or, in the absence of such a seed, little crystalline nuclei are formed homogeneously throughout the layer; this is the a → c transition in figure I.7 (Olson et al. 1987; Roth and Olson, 1987). The above mentioned processes are not fast enough to suppress melting when nanosecond

pulses are used (a → l in fig. 1.7). Depending on the experimental conditions the (undercooled) l-Si can solidify into α-Si again, grow epitaxially or crystallize spontaneously. This last situation can give rise to explosive crystallization in which the latent heat from the crystallization of the undercooled liquid melts additional α-Si. All these phenomena are related with the kinetics of melting and solidification. The remainder of this paragraph is therefore devoted to the basic principles of the transition state theory for crystal growth (Hillig and Turnbull, 1956; Turnbull, 1962; Spaepen and Turnbull, 1982; Tsao et al. 1986) and nucleation (Spaepen and Turnbull, 1982; Kelton et al. 1983; Tsao and Peercy, 1987).

The velocity u of the liquid-solid interface can be written as the difference between a melting and freezing term:

$$u = a\, v_0 f \left\{ \exp\left(-\frac{\Delta g_{l-t}}{k_B T_i}\right) - \exp\left(-\frac{\Delta g_{s-t}}{k_B T_i}\right) \right\} \tag{14}$$

where a is the jump distance, v_0 the jump frequency, f the fraction of interfacial sites at which rearrangement can occur, k_B the Boltzmann constant, T_i the temperature at the interface, and Δg_{l-t} and Δg_{s-t} the Gibbs free energy differences per atom between the liquid respectively solid and the transition state. Normally the term containing Δg_{l-t} is factored out and the effect of a possible energy barrier is represented as an effective attempt frequency $v_{eff} = v_0 \exp\left(-\frac{\Delta g_{l-t}}{k_B T_i}\right)$ to give:

$$u = a\, v_{eff} f \left\{ 1 - \exp\left(-\frac{\Delta g_{s-l}}{k_B T_i}\right) \right\} \tag{15}$$

where Δg_{s-l} is the Gibbs free energy of melting per atom. For small deviations from equilibrium the exponential term and Δg_{s-l} can be linearized:

$$u \simeq a\, v_{eff} f \frac{\Delta g_{s-l}}{k_B T_i} \simeq a\, v_{eff} f \frac{\Delta s_{s-l}(T_m - T_i)}{k_B T_i} \equiv \zeta^{-1} \Delta T_i \tag{16}$$

with Δs_{s-l} the entropy of solidification per atom, T_m the static melt temperature, and ζ^{-1} the velocity- undercooling/superheating constant. Equation 16 shows that the interface velocity is zero for $T_i = T_m$ and a certain amount of

undercooling/superheating is needed to move the liquid-solid interface. A number of authors have investigated the numerical value of ζ for c-Si by comparing calculated and measured temporal melt depths (Galvin et al. 1985; Thompson et al. 1985; Peercy et al. 1987). The most accurate number until now is 17±3 K/(m/s). The combination of this value with the amorphization velocity of 15±1 m/s and the difference in melt temperature between c- and α-Si of 225±20 K, results in a value for the ζ of α-Si between 0 and 7 K/(m/s).

The actual speed with which the solid-liquid interface will propagate is governed by the heat flow. In the stationary state, the heat flux Q through and the velocity u of the interface are related as:

$$Q = -\kappa_l \frac{\partial T_i}{\partial z}\Big|_l + \kappa_s \frac{\partial T_i}{\partial z}\Big|_s = -u\,\Delta h_{s-l} \tag{17}$$

where we have used a one-dimensional heat flow. Δh_{s-l} is the heat of melting per atom and z the position coordinate in the irradiated material. For most practical purposes concerning pulsed-laser annealing, equation 17 can be simplified to:

$$u = \kappa \frac{(T_s - T_i)}{\Delta h_{s-l}\, d} = \nu_{hf}\, a \frac{(T_s - T_i)}{T_m} \tag{18}$$

in which T_s stands for the temperature of the substrate at infinity and d for the effective thermal penetration depth, i.e. the distance for which a linearization of the temperature from the interface towards the substrate would give T_s. If c-Si is irradiated with visible light pulses of ≃10 ns full width at half maximum (FWHM) this characteristic length is of the order of a micron. At this point Spaepen and Turnbull (1982) introduced ν_{hf}, the characteristic frequency associated with heat flow:

$$\nu_{hf} = -\frac{\kappa T_m}{a\,\Delta h_{s-l}\, d} = -\frac{\kappa}{a\,\Delta s_{s-l}\, d} \tag{19}$$

The interface temperature can now be found by comparing equations 16 and 18:

$$\frac{(T_m - T_i)\,T_m}{(T_s - T_i)\,T_i} = \left(\frac{k_B}{\Delta s_{s-l}}\right)\left(\frac{v_{hf}}{v_{eff} f}\right) \tag{20}$$

For most materials $\frac{\Delta s_{s-l}}{k_B}$ is of the order of unity (for metals $\simeq$1, for Si and Ge $\simeq$3.6). The interface temperature is therefore dominated by the ratio of the two effective frequencies, see figure I.8. If $f v_{eff} \gg v_{hf}$ the propagation of the liquid-solid boundary is said to be heat flow limited and $T_i \rightarrow T_m$, figure I.8 (a). In the other limit $v_{hf} \gg f v_{eff}$ we speak of a growth or interface dominated motion and $T_i \rightarrow T_s$, figure I.8 (b).

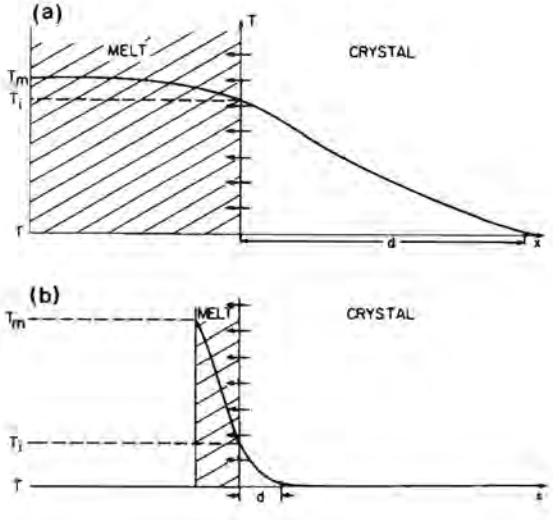

Figure I.8. Schematic diagrams of the temperature profile in case of (a) heat-flow limited and (b) interface limited solidification.

Little is known about the growth of α-Si. Equation 16 can of course be used both for crystalline and amorphous growth. The condition that the α-Si phase would outrun the c-Si phase, i.e. $u^{\alpha\text{-}Si} > u^{c-Si}$, can then be written as:

$$(v_{eff} f\, \Delta s_{s-l}\, \Delta T_i)^{\alpha\text{-}Si} > (v_{eff} f\, \Delta s_{s-l}\, \Delta T_i)^{c-Si} \tag{21}$$

Since the interfacial undercooling ΔT_i is always highest for the c-Si phase and since Δs_{s-l} for amorphous growth is not expected to differ much from that for

crystalline growth, the big difference must come about from the effective attempt frequency ν_{eff} and/or the fraction of interfacial sites f. However, until now it is unclear how these differences could be explained. The occurrence of α-Si growth from the free surface, which has only been observed in impurity implanted Si until now, is also not understood (Cullis et al. 1982, 1984; Campisano et al. 1985; Bruines et al. 1986b, 1987b; Peercy et al. 1986a). Cullis and coworkers (1982,1984) proposed that the initial growth of α-Si from the interior and the melting point depression for high impurity concentrations, resulting in highly undercooled l-Si, causes the "nucleation" of α-Si at the air-liquid interface. In this thesis we will show that the presence of impurities is not necessary for this process. It would be interesting to know whether amorphous regrowth from the free surface also occurs at ultra high vacuum conditions with the thin native oxyde surface layer removed.

Up to this point all the expressions were symmetric with respect to melting and solidification, which means that for a given value of $|T_m - T_i|$ the interface velocity will be the same irrespective of undercooling or superheating. Recently however, Tsao et al. (1986) found evidence for an asymmetry in the melting and freezing kinetics of c-Si. They argued that it is easier for the silicon to melt than to crystallize because of the large entropy difference between the liquid and the crystal. They proposed that the crystallization velocity is lowered with a factor of $\exp(-\frac{\Delta s_{s-l}}{k_B})$. For c-Si this would mean a reduction to only 3 % of its original value, which would fit in well with the fact that the superheating upon pulsed-laser melting is certainly below 6 K/(m/s) but that crystallization proceeds with an undercooling of 17 K/(m/s) (Tsao et al. 1987).

As already mentioned, the irradiation of α-Si with laser pulses in the nanosecond regime can produce a melt of highly undercooled l-Si. In the absence of a seed the only way to crystallize from this unstable state would appear to be via bulk nucleation. This mechanism was proposed to play a role in the explosive crystallization of α-Si (Wood et al. 1984). Based on TEM results, indicating an average grain size of ≃10 nm (Lowndes et al. 1984; Narayan and White, 1984), and estimating the available time to be ≃10 ns, they calculated a bulk nucleation rate of $\simeq 10^{32}\ m^{-3}\ s^{-1}$. Undercooling experiments on molten Si

by Devaud and Turnbull (1985) indicated a maximum value of only $2 \times 10^{10}\ m^{-3}\ s^{-1}$ at 240 K below the melting point of c-Si. This makes bulk nucleation as the process of explosive crystallization highly unlikely unless the l-Si is undercooled appreciably below the melting point of α-Si. Tsao and Peercy (1987) proposed a model in which the nucleation takes place at the liquid-solid interface. Recently, Roth and Olson (1987) and Roorda (1988) obtained data on homogeneous nucleation in solid α-Si. Their results indicate that XCR is possibly sustained and/or initiated by c-Si nuclei which are formed during heating of the solid material and grow as soon as they are in contact with undercooled l-Si. To give some insight into this matter of the origin of explosive crystallization, the last part of this chapter is devoted to the basic principles of homogeneous (=bulk) and heterogeneous (=interface) nucleation.

The Gibbs free energy difference of a crystalline nucleus with radius r surrounded by its melt is given by:

$$\Delta G = 4\pi r^2 \gamma + \frac{4\pi}{3} r^3 \Delta G_v \tag{22}$$

in which γ is the surface energy and ΔG_v the Gibbs free energy difference per unit volume. The critical nucleus is found by setting $\frac{d\Delta G}{dr} = 0$

$$r_c = -\frac{2\gamma}{\Delta G_v}; \quad \Delta G_c = \frac{16\pi\gamma^3}{3(\Delta G_v)^2} \tag{23}$$

The number of atoms in a critical nucleus can be found by multiplying $\frac{4\pi}{3} r_c^3$ with the density of atoms per volume. In the same manner as with the interface velocity it can be shown that the nucleation rate yields:

$$I = I_0 \exp\left(-\frac{\Delta G}{k_B T}\right) \simeq I_0 \exp\left(-\frac{16\pi\gamma^3}{3(\Delta G_v)^2 k_B T}\right) \tag{24a}$$

$$I_0 = N_{l-Si}\left[\frac{k_B T}{h}\right] \exp\left(-\frac{\Delta f_{l-c}}{k_B T}\right) \tag{24b}$$

where N_{l-Si} is the density of atoms in the liquid, h Planck's constant, and Δf_{l-c} the activation energy for transporting an atom across the liquid-solid barrier.

This last parameter is not known but Turnbull (1950) estimated it to be approximately equal to the activation energy for viscous flow. Based on this proposition he calculated that $I_0 \simeq 10^{39\pm1}\ m^{-3}\ s^{-1}$ for metals. Using the same approach for silicon we arrive at $6.8 \times 10^{39}\ m^{-3}\ s^{-1}$ at the melting temperature of α-Si. A more phenomenological treatment of the pre-exponential factor is given by Uhlmann (1972). According to his calculations I_0 can be expressed as $\{(k_B T)/(3\pi a^6 \eta)\}$ in which a is the mean distance between atoms in the liquid and η the viscosity. This expression results in a value of $\simeq 5 \times 10^{38}\ m^{-3}\ s^{-1}$ at the melting point of α-Si.

The Gibbs free energy difference Δg_v between c- and α-Si can be estimated by a linearization of the Gibbs free energy around the melting point of c-Si: $\Delta G_v(T) \simeq L_c\,(1 - T/T_m^{c\text{-}Si})$. For most practical purposes concerning nucleation, the Gibbs free energy is taken at the melting temperature of α-Si , $\Delta G_v\ (T_m^{\alpha\text{-}Si}) \simeq 5.8 \times 10^8\ Jm^{-3}$.

Unfortunately, the surface energy γ between the liquid and the crystalline phase is not well known for silicon. A crude approach to the determination of the surface energy of Si has been given by Turnbull (1950). He correlated the surface energy of an imaginary interface containing Avogadro's number of atoms γ_{mole} with the heat of fusion per mole ΔH_{mole} and found that most materials obey $\gamma_{mole} \simeq 0.35\ \Delta H_{mole}$. A more sophisticated treatment was given by Miedema and den Broeder (1979). In their model the interfacial energy between the solid and the liquid can be split into γ^I, reflecting the enthalpy change for the atoms in the surface layer of the solid and γ^{II} , accounting for the entropy change of the atoms in the surface layer of the liquid. The first term corresponds with that of Turnbull. Inserting a value for the already mentioned imaginary molar area and allowing for some small corrections, e.g. due to surface roughness on an atomic scale, this leads to:

$$\gamma^I = 2.5 \times 10^{-9}\ \frac{\Delta H_{mole}}{V_{mole}^{2/3}}\ \ Jm^{-2} \qquad (25a)$$

with V_{mole} the molar volume. The second term depends on the entropy difference S^* between the atoms in the first layer of the liquid and those in the bulk.

Miedema and den Broeder state that, in first approximation, γ^{II} must be independent of the material if calculated per unit molar surface area. Based on previous measurements of the surface energy for germanium (Turnbull, 1950), giving an entropy difference S* of 7×10^{-8} J/K , this leads to an expression for Si of:

$$\gamma^{II} = 7 \times 10^{-8}\ \mathrm{JK}^{-1}\ \frac{T}{V_{mole}^{2/3}} \tag{25b}$$

$$\gamma = 0.242 + 0.174 \times \frac{T}{1685\ \mathrm{K}}\ \mathrm{Jm}^{-2} \tag{26}$$

This results in a γ of $\simeq$0.4 Jm^{-2} for $T = T_m^{\alpha\text{-Si}} = 1460$ K . If all the parameters are inserted into equation 23 we find a bulk nucleation rate of $\simeq 10^{(30\pm1)}\ \mathrm{m}^{-3}\ \mathrm{s}^{-1}$. This number, however, depends strongly on the value of γ. The already mentioned undercooling experiments by Devaud and Turnbull (1985) yield a minimum value of 0.3 Jm^{-2}. To reach the nucleation rate estimated by Wood et al. (1984) with this value, an undercooling $T_m^{c\text{-}Si} - T$ of $\simeq$535 K would be necessary, which is more then 300 K below the melting point of α-Si. It is clear from this analysis that, in spite of the large uncertainties, homogeneous nucleation is indeed very unlikely.

The case of heterogeneous nucleation is even more complex and ill defined. A first approximation can be made under the following assumptions. i) The surface roughness is equal to the radius of the critical nucleus, ii) the surface energy between the nucleation plane material and the nucleus is negligible, and iii) no surface tension effects are present. The heterogeneous nucleation rate can now be derived from the homogeneous one by realizing that only half the surface energy is needed. This means that the radius of the critical nucleus is reduced by a factor of two but more importantly that its Gibbs free energy difference is lowered by a factor of eight. As a result the nucleation rate increases from $\simeq 10^{-(30\pm1)}$ to $\simeq 10^{(30\pm1)}\ \mathrm{m}^{-3}\ \mathrm{s}^{-1}$ for $\gamma = 0.4\ \mathrm{Jm}^{-2}$. The real heterogeneous nucleation rate can in first approximation be found by multiplying the homogeneous nucleation rate, including the corrected Gibbs free energy, by the radius of a critical nucleus. With the above calculated result this would lead to

a value of $10^{30}\ m^{-3}\ s^{-1} \times 10^{-9}\ m^{-1} \simeq 10^{21}\ m^{-2}\ s^{-1}$. A more sophisticated approach is to use the density of atoms per unit area in equation 24b to obtain the pre-exponential factor for heterogeneous nucleation (Turnbull, 1950). This means a reduction of I_0 by $\simeq 10^{10}$, which gives a comparable result. A nucleation rate of $\simeq 10^{22}\ m^{-2}\ s^{-1}$ means that the formation of c-Si nuclei at a (moving) liquid-solid boundary, as present during explosive crystallization, is not completely impossible. The value is, however, flattered by the crude assumptions made to arrive at this result. It is obvious that the heterogeneous nucleation rate could be strongly influenced by the presence of impurities at the solidification front but, as with heterogeneous nucleation itself, all models are highly speculative.

Spontaneous nucleation can of course also occur in solid α-Si. The corresponding nucleation rate is again described by equations 24a and 24b. Since the viscosity of a solid is $\simeq 10^{14}$ higher than that of a liquid (Uhlmann, 1972), the pre-exponential factor I_0 is now presumably lower than that of l-Si. However, the surface energy between α-Si and c-Si is much smaller than that between l-Si and c-Si. Model-building studies of planar interfaces separating c-Si and α-Si yield 0.13 Jm^{-2} (Spaepen, 1983). Nucleation experiments in α-Si films give 0.04 Jm^{-2} (Koster, 1978). Both values are considerably below the $\simeq 0.4\ Jm^{-2}$ for nucleation in the melt. An extrapolation of the data of Roth and Olson (1987) to 1460 K yields a homogeneous nucleation rate in the solid of $\simeq 10^{26}\ m^{-3}\ s^{-1}$, equivalent to one nucleus per 10 μm^3 in one nanosecond. Roorda (1988) recently showed that this density of nuclei can be obtained upon laser annealing with a single 32 ns FWHM ruby laser pulse.

In principle the quoted figures and equations for homogeneous and heterogeneous nucleation are only valid in the steady-state situation. For the transient regime, expression 24 must be multiplied by an additional factor (Kashchiev, 1969; Kelton et al. 1983).

$$\frac{I(t)}{I(\infty)} = \left[1 + \sum_{m=1}^{\infty} (-1)^m e^{-m^2 t/\tau_i}\right] \qquad (27a)$$

$$\text{with } \tau_i = \frac{4}{\pi^3}\ \frac{N}{I_0}\ \frac{1}{Z} \qquad (27b)$$

where $Z = \sqrt{\dfrac{\Delta G'}{6\pi k_B T n_c}}$ (27c)

N is the density of atoms, I_0 the pre-exponential factor for nucleation and Z the so called Zeldovitch factor, which in its turn contains the Gibbs free energy per atom $\Delta G'$, the Boltzmann constant k_B, the temperature T, and the number of atoms in a critical nucleus n_c. This last quantity can of course be found by multiplying the volume of a critical nucleus $\frac{4\pi}{3} r_c^3$ with the density of atoms N and depends on the nucleation mechanism via r_c

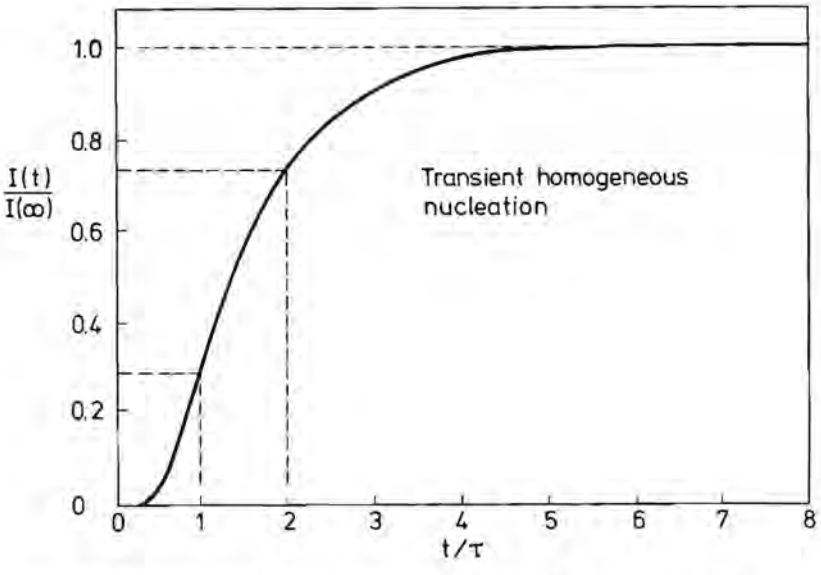

Figure I.9. Nucleation rate, normalized to its steady-state value, as a function of time, normalized to the incubation time τ, as calculated using expression 27a.

Figure I.9 gives the evaluation of expression 27a. The nucleation rate is completely negligible below $t/\tau = 0.5$ and increases to about 80 % of its steady-state value at $t = 2\tau$. Apart from some rearrangements, all the parameters needed to calculate the incubation time τ are given in this section. For heterogeneous nucleation at the liquid-solid front this leads to:

$$\tau \simeq 5 \times 10^{-13\pm1}\ \text{s} \sqrt{\frac{\dfrac{T}{1685\ \text{K}}\left[0.697 + 0.501\ \dfrac{T}{1685\ \text{K}}\right]^3}{\left[1 - \dfrac{T}{1685\ \text{K}}\right]^4}} \qquad (28)$$

This result must be multiplied by $\sqrt{8}$ for homogeneous nucleation in the melt because of the larger number of atoms in the critical nucleus. Expression 28 leads to an incubation time τ of $\simeq 3 \times 10^{-10+1}$ s at the melting point of α-Si. The temperature dependence of τ is only weak, its value changes with approximately $\pm$ 50 % for every $\pm$ 60 K variation around 1460 K. The uncertainty in these incubation times is large, not only because of the ill defined value of I_0 but also because of the crude approach to heterogeneous nucleation and the not accurately known value of the surface energy γ. This means that the incubation time for nucleation in the melt can be anything between a negligible 100 ps to a noticeable 10 ns.

A calculation of the incubation time for nucleation in the solid, using Uhlmann's (1972) phenomenological approach to the pre-exponential factor, yields a value of the order of hours. This because I_0 is greatly reduced, while the Zeldovitch factor Z hardly changes. It is clear that this can not be true, which suggests that the dependence of the pre-exponential factor on the viscosity, as described by Uhlmann (1972), is not valid in solids. This is not surprizing if one bears in mind that the local rearrangements needed for nucleation, are no longer strictly coupled to bulk properties in the solid.

References Chapter I

Adams, J.R., and Bashara, N.M. (1970); Surf. Sci. **49**, 441.

Ashcroft, N.W. and Mermin, N.D. (1976); Solid-State Physics (Holt-Saunders International Edition, Philadelphia, 1976), page 499.

Aspnes, D.E., and Theeten, J.B. (1980); J. Electrochem. Soc. **127** , 1359.

Baeri, P., and Campisano, S.U. (1982); *Laser Annealing of Semiconductors* edited by J.M. Poate and J.W. Mayer (Academic Press, New York, 1982), page 79.

Baeri, P., Foti, G., Poate, J.M., Cullis, A.G. (1980); Phys. Rev. Lett. **45**, 2036.

Bagley, B.G., and Chen, H.S. (1979); AIP Conf. Proc. **50**, 97.

Bartsch, H., Andra, G., and Glaser, E. (1986); Phys. Stat. Sol. (a) **94**, 773.

Bruines, J.J.P., van Hal, R.P.M., Boots, H.M.J., and Wolter, J. (1986a); *Energy Beam – Solid Interaction and Transient Thermal Processing* edited by V.T. Nguyen and A.G. Cullis (Les editions des physique, Les Ulis Cedex, 1986), page 525.

Bruines, J.J.P., van Hal, R.P.M., Boots, H.M.J., Sinke, W., and Saris, F.W. (1986b); Appl. Phys. Lett. **48**, 1252.

Bruines, J.J.P., van Hal, R.P.M., Boots, H.M.J., Polman, A., and Saris, F.W. (1986c); Appl. Phys. Lett. **49**, 1160.

Bruines, J.J.P., van Hal, R.P.M., Koek, B.H., Viegers, M.P.A., and Boots, H.M.J. (1987a); Appl. Phys. Lett. **50**, 507.

Bruines, J.J.P., van Hal, R.P.M., Koek, B.H., Viegers, M.P.A., and Boots, H.M.J. (1987b); MRS Symp. Proc. Vol. **74**, 91.

Campisano, S.U., Jacobson, D.C., Poate, J.M., Cullis, A.G., and Chew, N.G. (1985); Appl. Phys. Lett. **46**, 846.

Chapman, R.L., Fan, J.C.C., Zeiger, H.J., and Gale, R.P. (1980); Appl. Phys. Lett. **37**, 292.

Chen, H.S. and Turnbull, D. (1969); J. Appl. Phys. **40**, 4114.

Cortot, J.P., and Ged, Ph. (1982); Appl. Phys. Lett. **41**, 93.

Cullis, A.G., Chew, N.G., Webber, H.C., Smith, D.J. (1984); J. Crystal Growth **68**, 624.

Cullis, A.G., Webber, H.C., and Chew, N.G. (1980); Appl. Phys. Lett. **36** , 547.

Cullis, A.G., Webber, H.C., and Chew, N.G. (1982); Appl. Phys. Lett. **40** , 998.

Devaud, G., Turnbull, D. (1985); Appl. Phys. Lett. **46**, 844.

Donovan, E.P., Spaepen, F., Turnbull, D., Poate, J.M., Jacobson, D.C. (1985); J. Appl. Phys. **57**, 1795.

Fredrickson, J.E., Waddell, C.N., Spitzer, W.G., and Hubler, G.K. (1982); Appl. Phys. Lett. **40**, 172.

Galvin, G.J., Mayer, J.M., and Peercy, P.S. (1985); Appl. Phys. Lett. **46** , 644.

Glasov, V.M., Chizhevskaya, S.N., and Glagoleva, N.N. (1969); *Liquid Semiconductors* (Plenum Press, New York, 1969).

Goldsmid, H.J., Kaila, M.M., and Paul, G.L. (1983); Phys. Stat. Sol. (a) **76**, K31.

Goldsmith, A., Waterman, T.E., and Hirschhorn, H.J. (1961); *Handbook of Thermophysical Properties of solid Materials* (Pergamon, New York, 1961), Vol. 1, page 1-576.

Gore, G (1855); Philos. Mag. **9**, 73.

Hillig, W.B., Turnbull, D. (1956); J. Chem Phys. **24**, 914.

Hultgren, R., Desai, P.D., Hawkins, D.T., Gleiser, M., Kelley, K.K., and Wayman, D.D. (1973); *Selected Values of the Thermodynamic Properties of the Elements* (Pergamon, New York, 1973).

Jacobson, D.C., Elliman, R.G., Gibson, G.M., Olson, G.L., Poate, J.M., and Williams, J.S. (1987); Mat. Res. Soc. Symp. Proc. **74**, 327.

Jellison, G.E., Modine, F.A. (1982a); J. Appl. Phys. **53**, 3745.

Jellison, G.E., Modine, F.A. (1982b); Appl. Phys. Lett. **41**, 180.

Jellison Jr., G.E., Modine, F.A. (1983); Phys. Rev. B **27**, 7466.

Jellison Jr., G.E., Burke, H.H. (1986); J. Appl. Phys. **60**, 841.

Jellison Jr., G.E. and Lowndes, D.H. (1985); Appl. Phys. Lett. **47** , 718.

Jellison Jr., G.E., Lowndes, D.H., Mashburn, D.N., and Wood, R.F. (1986); Phys. Rev. B **34**, 2407.

Kelton, K.F., Greer, A.L., and Thompson, C.V. (1983); J. Chem. Phys. **79** , 6261.

Kittel, C. (1976a); *Introduction to Solid State Physics* (John Wiley & Sons, inc., New York, 1976), chapter 5.

Kittel, C. (1976b); *Introduction to Solid State Physics* (John Wiley & Sons, inc., New York, 1976), page 178.

Koster, U. (1978); Phys. Stat. Sol. A 48, 313.

Lampert, M.O., Koebel, J.M., and Siffert, P. (1981); J. Appl. Phys. **52** , 4975.

Leamy, H.J., Brown, W.L., Celler, G.K., Foti, G., and Gilmer, G.H. (1981); Appl. Phys. Lett. **38**, 137.

Lowndes, D.H., Jellison Jr., G.E., Pennycook, S.J., Withrow, S.P., and Mashburn, D.N. (1986); Appl. Phys. Lett. **48**, 1389.

Lowndes, D.H., Wood, R.F., and Narayan, J. (1984); Phys. Rev. Lett. **52** , 561.

Lue, J.T., and Shaw, S.Y. (1982); J. Appl. Phys. **53**, 5617.

McGill, T.C., and Kurtin, S.L., and Shifrin, G.A. (1970); J. Appl. Phys. **41**, 246.

Miedema, A.R., and den Broeder, F.J.A. (1979); Z. Metallde. **70** , 14.

Murakami, K., Gerritsen, H.C., van Brug, H., Bijkerk, F., Saris, F.W., and van der Wiel, M.J. (1986); MRS Symp. Proc. Vol. **51**, 119.

Narayan, J. (1986); J. Vac. Sci. Technol. A **4**, 61.

Narayan, J. and White, C.W. (1984); Appl. Phys. Lett. **44**, 35.

Narayan, J., Pennycook, S.J., Fathy, D., and Holland, O.W. (1984); J. Vac. Sci. Technol. A **2**, 1495.

Nygren, E., Williams, J.S., Pogany, A., Elliman, R.G., Olson, G.L., and McCallum, J.C. (1987); Mat. Res. Soc. Symp. Proc. **74**, 307.

Olson, G.L. (1985); Mat. Res. Soc. Symp. Proc. **35**, 25.

Olson, G.L., Roth, J.A., Nygren, E., Pogany, A.P., and Williams, J.S. (1987); MRS Symp. Proc. Vol. **74**, 109.

Peercy, P.S., Poate, J.M., Thompson, M.O., Tsao, J.Y. (1986a); Appl. Phys. Lett. **48**, 1651.

Peercy, P.S., Thompson, M.O., and Tsao, J.Y. (1986b); Mat. Res. Soc. Conf. Proc. Vol. **53**, 125.

Peercy, P.S., Thompson, M.O., and Tsao, J.Y. (1987); Mat. Res. Soc. Conf. Proc. Vol. **74**, 15.

Ravindra, N.M., Narayan, J. (1986); J. Appl. Phys. **60**, 1139.

Roorda, S., Saito, S., and Sinke, W.C. (1988); submitted to Phys. Rev. Lett.

Roth, J.A., and Olson, G.L. (1987); Mat. Res. Soc. Symp. Proc. **74** , 319.

Sharev, K.M., Baum, B.A., and Gel'd, P.V. (1975); Sov. Phys. Solid State **16**, 2111.

Sharev, K.M., Baum, B.A., and Gel'd, P.V. (1977); High Temperature **15** , 548.

Sinke, W and Saris, F.W. (1984); Phys. Rev. Lett. **53**, 2121. The pulse length mentioned in this text (20 ns) is incorrect. The right value is 32 ns.

Sinke, W.C., Warabisako, T., Miyao, M., Tokuyama, T., Roorda, S., and Saris, F.W. (1988); Mat. Res. Soc. Symp. Proc., Boston U.S.A., December 1987, to be published.

Spaepen, F., and Turnbull, D. (1979); AIP Conf. Proc. **50**, 73.

Spaepen, F. and Turnbull, D. (1982); *Laser Annealing of Semiconductors* edited by J.M. Poate and J.W. Mayer (Academic Press, New York, 1982), page 15.

Spaepen, F. (1983); *Amorphous Materials: Modeling of Structure and Properties*, edited by Vitek, V. (The Metallurgical Society of the American Institute of Mining, Metallurgical and Petroleum Engineers, New York, 1983), page 265.

Thompson, M.O., Bucksbaum, P.H., and Bokor, J. (1985); Mat. Res. Soc. Conf. Proc. Vol. **35**, 181.

Thompson, M.O. and Galvin, G.J. (1983); Proc. Mat. Res. Soc. Vol. **13** , 57.

Thompson, M.O., Galvin, G.J., Mayer, J.W., Peercy, P.S., Poate, J.M., Jacobson, D.C., Cullis, A.G., and Chew, N.G. (1984); Phys. Rev. Lett. **52** , 2360.

Thompson, M.O., Mayer, J.W., Cullis, A.G., Webber, H.C., Chew, N.G., Poate, J.M., and Jacobson, D.C. (1983); Phys. Rev. Lett. **50**, 896.

Thompson, M.O., Peercy, P.S., Tsao, J.Y., Aziz, M.J. (1985); Appl. Phys. Lett. **49**, 558.

Thompson, M.O. and Peercy, P.S. (1986); Mat. Res. Soc. Symp. Proc. Vol. **51**, 99.

Touloukian, Y.S. and Boyco, E.H. (1970); *Thermophysical Properties of Matter*, (IFI/Plenum, New York-Washington, 1970), Vol. 4, page 204.

Touloukian, Y.S., Powell, R.W., Ho, C.Y., and Klements, P.G. (1970); *Thermophysical Properties of Matter* , (IFI/Plenum, New York-Washington, 1970), Vol. 1, page 339.

Tsao, J.Y., Aziz, M.J., Thompson, M.O., Peercy, P.S. (1986); Phys. Rev. Lett. **25**, 2712.

Tsao, J.Y., Peercy, P.S., and Thompson, M.O. (1987); J. Mat. Res. **2** , 91.

Tsao, J.Y. and Peercy, P.S. (1987); Phys. Rev. Lett. **58**, 2782.

Turnbull, D. (1950); J. Appl. Phys. **21**, 1022.

Turnbull, D. (1962); J. Phys. Chem. **66**, 609.

Uhlmann, D.R. (1972); J. Non-Cryst. Sol. 7, 337.

Viegers, M.P.A., Koek, B.H., Bruines, J.J.P., van Hal, R.P.M., and Boots, H.M.J. (1986); Proc. XIth Cong. on Electron Microscopy, Kyoto 1986, 1521.

Wagner, M., Geiler, H.-D., and Goetz, G. (1985); Phys. Stat. Sol. (a) **92**,413.

Watanabe, K., Miyao, M., Takemote, I., and Hashimoto, N. (1979) Appl. Phys. Lett. **34**, 518.

Webber, H.C., Cullis, A.G., and Chew, N.G. (1983); Appl. Phys. Lett. **43** , 669.

White, C.W. (1986); private communication.

Wood, R.F. and Geist, G.A. (1986a); Phys. Rev. B **34**, 2606.

Wood, R.F. and Geist, G.A. (1986b); Phys. Rev. Lett. **57**, 873.

Wood, R.F., Lowndes, D.H., and Narayan, J. (1984); Appl. Phys. Lett. **44** , 770.

II. EXPERIMENTAL SET-UP

II.1 Introduction

The pulsed-laser annealing of c- and α-Si has shown a wide variety of melt and solidification phenomena. To understand these phenomena, the system must be studied under various experimental conditions with many different techniques. The annealing parameters such as pulse duration or substrate temperature are often difficult to vary. As a result, most experiments focus on the combination of as many probe methods as possible. In general these techniques can be classified according to whether they take place before or after the experiment. Into the first case fall the time-resolved reflectivity/ellipsometry (TRR/TRE) and time-resolved conductivity (TRC) methods. The second case includes e.g. Rutherford backscattering spectroscopy (RBS), transmission electron microscopy (TEM), and static reflectivity/ellipsometry (SR/SE) measurements. The latter techniques are more or less standard service activities in most laboratories, the time-resolved experiments are more complicated and require an individual approach. Except for TRC, all techniques have been used in the present work. This chapter is devoted to the way in which we performed our pulsed-laser annealing and TRR experiments.

The next section presents the set-up used for the pulsed-laser annealing experiments. The importance of a uniform energy-density profile and variable pulse duration will be discussed as well as our approach to those problems. The third section of this chapter deals with the set-up for the TRR measurements. Firstly the focus will be on the optical configuration and secondly on the electronics to monitor the signals. The preparation and characterization of the α-Si samples is described in the fourth and last section.

II.2 The Experimental Set-Up for Pulsed-Laser Annealing

II.2.1 Basic principles and energy-density profile considerations.

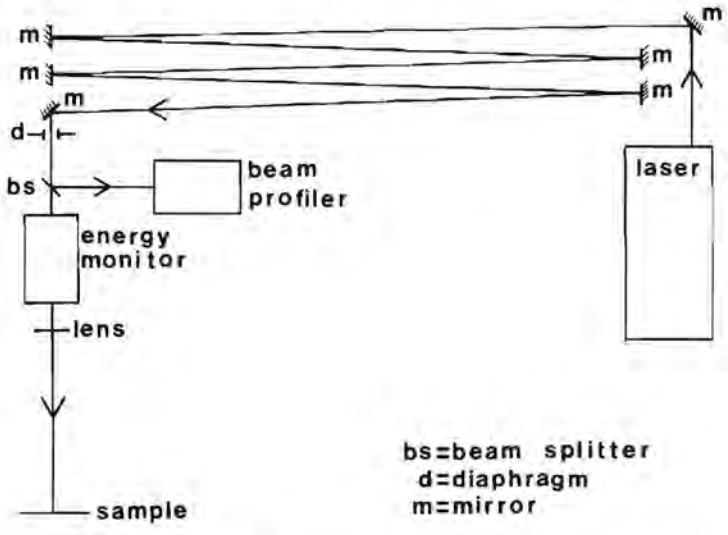

Figure II.1. Basic elements of the set-up used for laser annealing.

The basic principles of our experimental set-up for the pulsed-laser annealing of c- and α-Si is shown in figure II.1. The experiments have been performed with either a "Quanta-Ray" DCR-1A frequency-doubled neodymium:yttrium aluminum garnet (Nd:YAG) laser ($\lambda = 532$ nm) or a "JK Lasers" SYSTEM 2000 ruby laser ($\lambda = 694$ nm, on loan from the "Institute for Atomic and Molecular Physics", Amsterdam, the Netherlands). The Nd:YAG laser has some disadvantages with respect to the ruby laser. YAG has large thermal lensing and birefringence effects, which determine the design of the optical resonator. This means that the energy content of a pulse and its corresponding energy-density profile are dependent on the temperature distribution in the laser rods. The Nd:YAG laser can therefore only be optimized for a fixed setting of the flashlamp energy. Moreover, the DCR-1A Nd:YAG laser has an unstable optical resonator while the ruby laser has a stable one. This results in a much smoother energy-density profile for the ruby laser. The flashlamps of the

Nd:YAG laser operated at the maximum energy of 40 J per lamp (160 J in total) and were fired at a frequency of 10 Hz. This procedure ensured a stable temperature profile in the laser rods after several hours, which minimized output energy fluctuations and changes in the energy-density profile. The pulses could be extracted from the thus operated laser by activating the Q-switch from a remote control box. In this way single 7.5 ns FWHM pulses were obtained with an energy content of ≃300 mJ and a pulse to pulse energy fluctuation of ±3 %. As mentioned, the ruby laser is much less sensitive to the temperature distribution in the rods. Therefore it can be operated in the single-shot mode without firing the flashlamps at a constant rate. With a lamp energy of ≃65 J (260 J in total), the ruby laser produced 32 ns FWHM pulses with an energy content of 3 J.

The energy-density profile of both lasers is far from uniform. Since the melt and solidification phenomena depend on energy-density, special arrangements have to be made to eventually obtain a flat (top-hat) energy-density profile. A few of the solutions to this problem have been reviewed by Hill (1982). The most commonly used method is the mixing of the initial beam into many spatial components, introduce angular and phase differences, and recombine them at the surface to be processed. This can for instance be done with a quartz rod guide diffusor (Cullis et al. 1979). The scattering of the beam is there accomplished by a matte entrance face of a quartz waveguide and a large number of rays propagate through the rod by total internal reflection to the polished output face. A uniformity of 95 % in energy-density over an area almost that of the output face can be achieved for distances smaller than 1 mm from the end surface. The energy-density profile deteriorates rapidly beyond this distance. Another method is to use such a small spatial fraction of the beam that the intensity is nearly constant over its area. The first technique is normally superior to the second one because of its ability to anneal large areas for a given pulse energy, which facilitates RBS and TEM measurements. However, the small distance between the output face and the sample makes it virtually impossible to perform time-resolved reflectivity experiments. We have therefore chosen the second method.

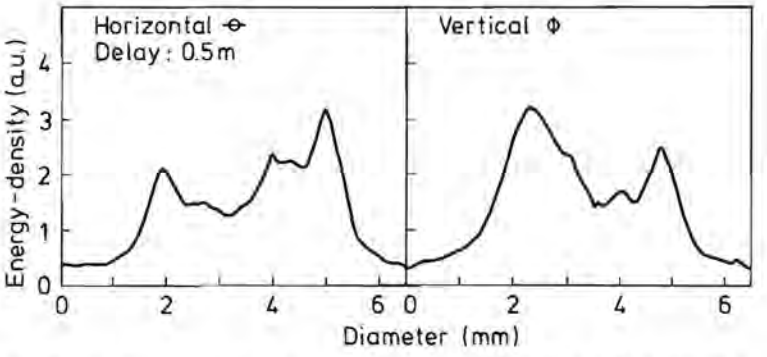

Figure II.2. Typical energy-density profile of the DCR-1A Nd:YAG laser, operated under standard conditions, at a distance of 0.5 m after the laser head.

Unfortunately, the initial energy-density profile of the Nd:YAG laser exhibits large fluctuations over short distances (hot spots), see figure II.2. Therefore it is impossible to select an area of reasonable proportion with an adequate energy-density profile at a short distance from the laser. Moreover, the high energy-density there ($\simeq$2 Jcm^{-2}) can easily damage optical components. The solution to this problem is to use an optical delay line of sufficient length to ensure a smooth intensity profile afterwards. A standard criterion for the distance needed to obtain this so called far-field regime is that the Fresnel number, the squared radius of the aperture divided by the product of the wavelength and the distance, is much larger than one. For a laser rod radius of 3 mm and $\lambda = 532$ nm, this gives a delay line length much larger than $(3\ \text{mm})^2 / (532\ \text{nm}) = 17$ m . In practice a delay line of 14 m, obtained by folding the beam several times with the aid of mirrors, sufficed to get a reasonably smooth energy-density profile (see figure II.3). From the standard theory for diffraction at the circular laser rod (Born and Wolf, 1983), it follows that the energy-density must be uniform within 90 % over distances <170 μm for a delay line of 10 m, irrespective of the initial uniformity of illumination. The near Gaussian energy-density profile of the ruby laser was so smooth already that we only needed one pass of the delay line ($\simeq$4 m). Eventually, a small portion of the laser beam was extracted by means of a diaphragm (d). For the Nd:YAG laser, a uniformity of about 90 %

in the energy-density could be obtained with an aperture of 1 mm ϕ, see figure II.4.

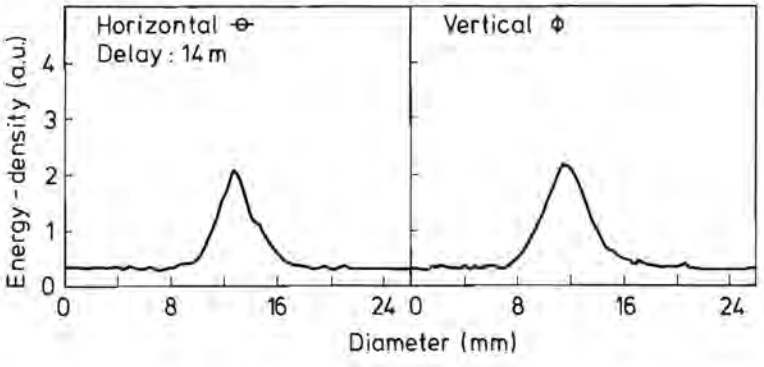

Figure II.3. Characteristic energy-density profile of the DCR-1A Nd:YAG laser, operated under standard conditions, at a distance of 14 m after the laser head.

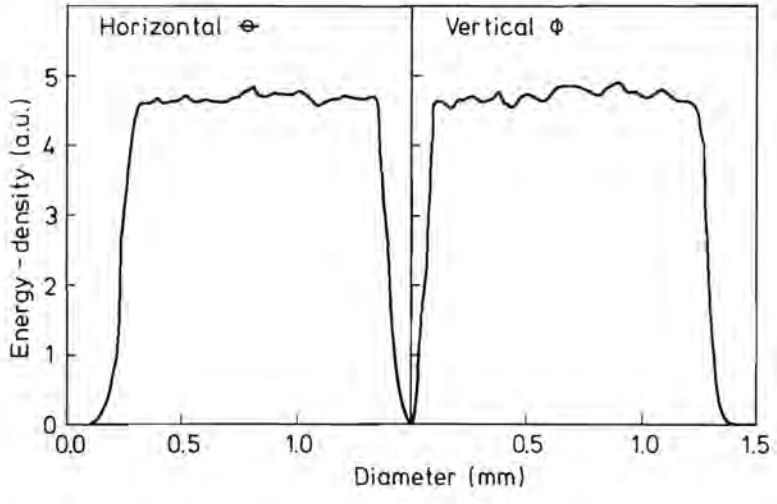

Figure II.4. Typical energy-density profile after an aperture of 1 mm ϕ.

However, small variations in the angle at which the pump beam leaves the laser in combination with the optical delay line, give a shift in the position of the beam at the aperture of a few millimeters. Unfortunately, this causes large changes in the energy-density profile and therefore less than $\simeq$20 % of the shots are useful. Moreover, not only the uniformity but also the absolute value of the

energy-density is affected, which makes it virtually impossible to do experiments at a fixed, previously chosen energy-density. The ruby laser has none of the above mentioned problems with the so called beam pointing stability. A much better result of <5 % non-uniformity of the energy-density across a diaphragm of 1.5 mm ϕ was achieved for every shot. The stability of its output beam made it possible to do experiments at a chosen energy-density with a 100 % yield.

The aperture (d) is projected on the sample by a biconvex lens, focal length and diameter both 400 mm. Crude variations of the energy-density range were made by adjusting the magnification of the system (M≃0.8-1.2), the final adjustment was done by neutral density filters. The high pulse energies used made it necessary to utilize volume volume absorbing neutral density filters and single component optical elements with high energy coatings throughout the path of the pump beam. The aperture (d) is immediately followed by a beam splitter (bs), which couples approximately 10 % of the energy out of the main optical path to monitor the intensity profile on a pulse to pulse basis.

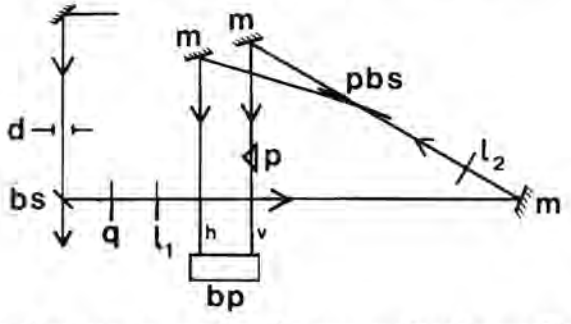

Figure II.5. Optical set-up to monitor the energy-density profile after the aperture (detail of figure I.1).

A detailed picture of the set-up for the beam profiling is given in figure II.5. The main part of the system projects the aperture on a "Delta Developments" Laser Beam Profile Monitor Mark IV (bp), consisting of a linear array of 60 pyroelectric elements, by means of two lenses (l_1, l_2). The size of the elements is 0.375 x 2.67 mm (1 mm^2) and their sensitivities are equal within 1.5%. Furthermore, the energy-density scale of the apparatus is calibrated to ±3%. To get a good overall impression of the intensity profile, the array is used to monitor both a

horizontal (h) and a vertical (v) cross section of the beam. For that purpose, the beam is split in two via a polarizing beam splitter (pbs) positioned after the second lens (l_2). One of the thus formed beams passes a prism (p) which is rotated 45 degrees to get a 90 degrees rotation of the intensity profile. Both beams impinge on the array, each covering about half of the available elements. Every cross section is projected on about 30 elements, which results in a total resolution of 30 or 50 μm depending on the diaphragm. A quarter wave plate (q) is used before the first lens to give the extracted beam the circular polarization needed for the 50%-50% division at the polarizing beam splitter. The so recorded intensity profiles were used to select the data on the basis of their uniformity of energy-density. Pulse energies were measured by a commercially available instrument ("Delta Developments" Pulsed Laser Energy Monitor), which was placed directly into the main optical path just before the lens. In this way the energy of every pulse was determined with an error <5 %.

II.2.2 Variation of the pulse length.

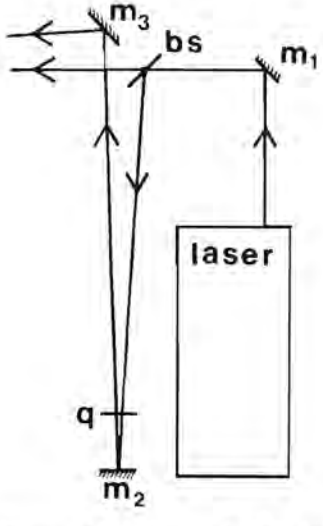

Figure II.6. Optical delay line to vary the pulse duration between 7.5 and 18 ns (quasi FWHM).

As already mentioned in the introduction to this chapter, there is a need to be able to vary certain experimental parameters. Unfortunately, both lasers have a fixed pulse duration. In order to study the influence of the pulse length on the melt and solidification behaviour of α-Si, a double pulse technique was set up to effectively lengthen the pulse duration. The method used is illustrated in figure II.6. Just after the first mirror (m_1) of the main optical delay line, 50 % of the energy is coupled out via a beam splitter (bs). An additional mirror (m_2) introduces an extra delay for one of the beams after which it is fed into the main delay line again (m_3) in such a way that both

beams superimpose at the aperture. To avoid interference effects the auxiliary delay line is provided with a quarter wave plate (q), which gives the second pulse a polarization perpendicular to the first one. Pulse delays of 5 to 10 ns were used giving quasi FWHM durations up to 18 ns, see figure II.7. When using this double pulse technique, not only the energy-density profile but also the temporal

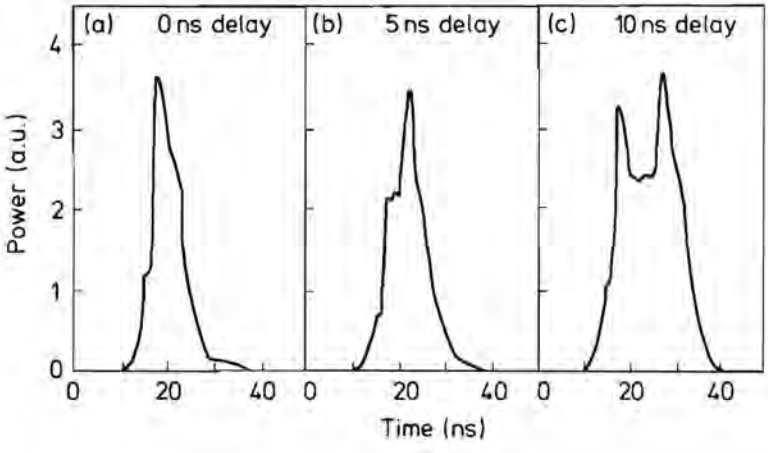

Figure II.7. Temporal pulse shape as obtained with the double pulse technique for a) 0 ns, b) 5 ns, and c) 10 ns delay between both pulses.

pulse shape was monitored with every pulse since fluctuations in the intensity ratio between the two beams, caused by the already mentioned beam pointing instability in combination with a different total delay line length, change the evolution in time of the combined pulse.

II.3 The Time-Resolved Reflectivity Set-Up

II.3.1 The optical set-up.

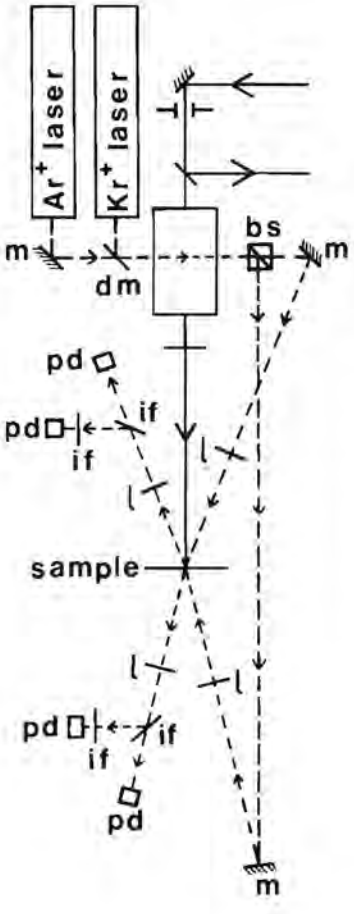

Figure II.8. Schematic drawing of the optical set-up for the TRR measurements.

The real-time monitoring of the reflectivity of c- and α-Si upon pulsed-laser irradiation puts heavy demands on the optical arrangement. In order to investigate melting and solidification fronts with propagation velocities up to tens of meters per second, the power of the probe lasers must be constant on a nanosecond timescale. This constraint results in the use of either single-frequency lasers or lasers with power fluctuations far beyond the bandwidth of the detection system. Furthermore the variety of possible melting and solidification phenomena makes it is necessary to use several probe wavelengths impinging at different directions to gain as much insight as possible. The resulting set-up for the TRR measurements is given in figure II.8. The drawing can only be schematic since the exact configuration depends on the class of experiments. TRR measurements have been performed at four wavelenghts; $\lambda = 820$ nm (AlGaAs diode laser), $\lambda = 647$ nm (krypton ion laser), $\lambda = 633$ nm (helium-neon laser), and $\lambda = 488$ nm (argon ion laser). The AlGaAs diode laser has the advantage that its power variations are on a picosecond timescale, which is far beyond our resolution. To satisfy our need for constant power at a nanosecond timescale, the other laser must be single-frequency. One way to achieve this is to use a laser

with short resonator, which only permits one longitudinal mode. Unfortunately, these lasers have a very low, <1 mW, output power. A combination of single-frequency operation and reasonable output power can be obtained by a standard length laser with an intra-cavity etalon.

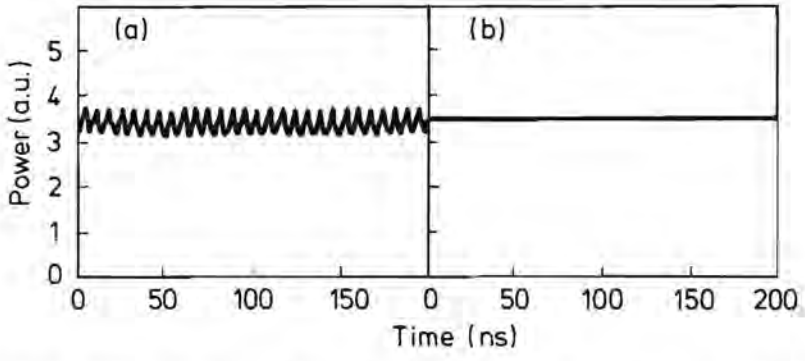

Figure II.9. Temporal output power of the used "Spectra-Physics" model 165 argon ion laser before (a) and after (b) insertion of an intra-cavity etalon. This result is also applicable for the helium-neon and krypton ion laser.

Figure II.9 shows the temporal output power of the used "Spectra-Physics" model 165 argon ion laser both with and without intra-cavity etalon. The helium-neon and krypton ion laser were also made single-frequency in this way. Only two wavelengths (lasers) could be handled simultaneously as is schematically shown in figure II.8. Both beams are made collinear by means of a dichroic mirror (dm) and cross the beam of the melt laser. There it is divided into two beams with a beam splitting cube (bs), one to probe the front and one to probe the rear of the sample. Each of the two sections contains a lens (*l*) to focus the probe beam and a lens to collect the reflected light again and project it onto two photodiodes (pd). The wavelengths are separated after the collection lens by means of two interference filters (if). This procedure also eliminates the transmission of scattered light from the melt laser to the photodiodes.

Three conflicting factors influence the power and focussing of the probe beams. Firstly, sufficient power is needed to have a reasonable signal to noise ratio. Secondly, a small spot is needed to obtain a good uniformity of the energy-density of the melt laser across the probe area. Thirdly, a low intensity

is needed to avoid excessive pre-heating of the sample. The second effect is of minor importance since the energy-density should already be uniform across the (larger) area irradiated by the melt laser. On the other hand, if the position of the probe spot is reasonably well known it is possible to deduce the energy-density at this position for a non-uniform profile. The pre-heating of the sample can, of course, be reduced by gating the probe beams, allowing them to irradiate the sample only during a time window around the melt laser pulse. It is however difficult to synchronize these events without using rather expensive techniques such as photo-acoustic or electro-optic switching. For this reason and because of the only moderate importance of a small probe spot, we have chosen to optimize the focus of the probe beam with respect to the power needed for a reasonable signal to noise ratio. The temperature T(t) on the surface of a half-infinite medium with thermal conductivity κ and thermal diffusivity D and at the center of a Gaussian heat source with an 1/e radius of ρ is given by (Pittaway, 1964):

$$T(t) = T(0) + \frac{P_{abs}}{\pi^{3/2}\kappa\rho} \arctan\sqrt{\frac{4Dt}{\rho^2}} \tag{29a}$$

wherein P_{abs} is the dissipated power in the medium. For $t > \frac{\rho^2}{4D}$ the temperature increase approaches its asymptotic value:

$$\delta T(t \to \infty) = \frac{P_{abs}}{2\sqrt{\pi}\,\kappa\rho} \tag{29b}$$

The allowable pre-heating is determined by the $\simeq$10 % error with which the energy-density threshold for melting can be measured. Given the melting point of α-Si, $\simeq$1460 K, this results in a tolerated temperature rise of <120 K. To be able to use both c-Si and glass substrates without changing the focussing of the probe beams, we take the worst-case value of 1.4 $Wm^{-1}K^{-1}$, $= \kappa_{glass}$, for the heat conductivity in equation 29b. In the next paragraph it will be shown that a reasonable signal to noise ratio can be obtained with a power of $\simeq$20 mW. If we assume that the incident light of the two probe lasers in completely absorbed, $P_{abs} = 2 \times 20 = 40\,mW$, equation 29b gives a worst-case minimum 1/e diameter

of about 140 μm. The actual spot size was set up to be approximately 200 μm ϕ. This gives a maximum pre-heating of only a few Kelvin when using c-Si substrates and about 80 K on glass. These values are almost instantaneously reached since the response time of the system is <1 ms. The resulting non-uniformity of the energy-density across the probe spot was at least a factor of four better than the 10 % specified across the total area irradiated by the melt laser.

II.3.2 Electronical equipment and resolution

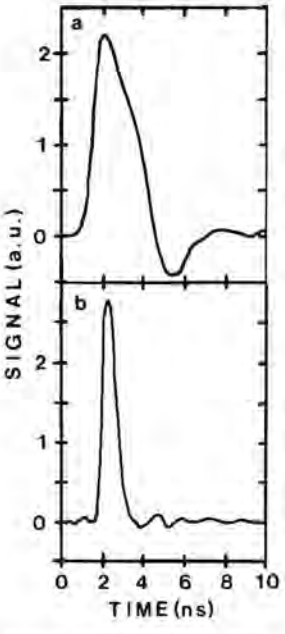

Figure II.10. Response of the system with (a) the FND-100 and (b) the PD-10 photodiode on a 190 ps FWHM pulse.

In the preceeding paragraph it was noted that the phenomena relevant for us occur on a nanosecond timescale. In order to record such fast signals, the overall 1/e rise time τ of the system must be at least a factor of two shorter. Recently, transient digitizers with a bandwidth of 6 GHz, $\tau = 27$ ps, have become available ("Tektronix" 7250). The older "Tektronix" R7912 and 7912AD transient digitizers we used had a bandwidth of 500 MHz, $\tau = 320$ ps, but with the advantage of a higher sensitivity. Avalanche photodiodes can be as fast as a few picoseconds but are not very suitable for absolute reflectivity measurements because of the low light intensity at which they saturate. Therefore we have used two types of non-avalanche photodiodes: the "EG&G" FND-100 with an active area of 5.1 mm^2 and a rise-time (10-90 %) of <1 ns, and the "Opto-Electronics LTD." PD10 with an active area of 0.25 mm^2 and a rise-time (1/e) of <90 ps. The bandwidth of the complete electronic system, photodiode and transient digitizer, has been determined by recording a 190 ps FWHM pulse from a mode-locked Krypton ion laser after which the result was

analysed by a fast Fourier procedure. This pulse has a frequency spectrum which can be considered to be flat up to 1 GHz. This means that the measured bandwidth will be that of the system itself. Figures II.10 gives the recorded response of the system for both photodiodes when excited with such a 190 ps FWHM pulse. It can clearly be seen that the FND-100 (Fig. II.10a) is not as fast as the PD10 (Fig. II.10b) photodiode. The spectral analysis of the measured responses is given in figure II.11.

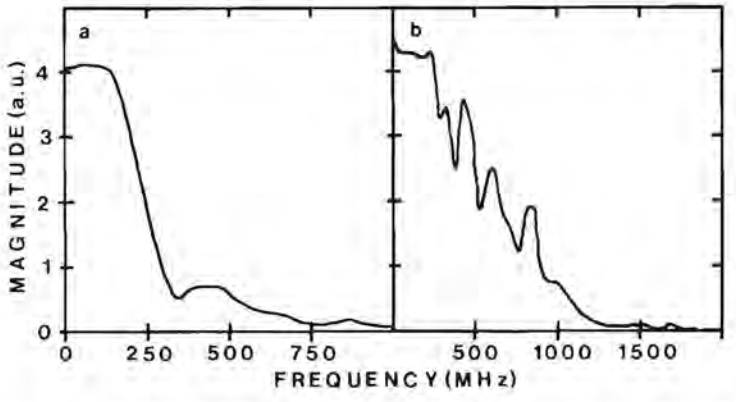

Figure II.11. Fourier analysis of the signals from figure II.10. (a) FND-100 photodiode giving a -3 dB bandwidth of ≃250 MHz, and (b) PD-10 photodiode resulting in a -3 dB bandwidth of ≃500 MHz.

For the FND-100 photodiode (Fig. II.11a) we get a -3dB frequency of ≃250 MHz, giving a τ of 0.6 ns. In this case the response of the system is limited by the photodiode. This situation changes when using the much faster PD10 photodiode, as can be seen in figure II.11b. Here the -3dB point is ≃500 MHz, $\tau = 0.3$ ns, the known cut-off frequency of the transient digitizer.

Absolute reflectivity values were obtained by scaling the TRR signal according to the initial static reflectivity of the sample. The responsivity of both photodiodes is better than 0.2 mA/mW, which gives a signal of >5 mV/mW across the 50 Ω transmission line. This must be compared with ≃0.5 mV noise from the transient digitizers. Given the worst-case reflectivity values of 32 % for c-Si and 76 % for l-Si at normal incidence (table I and III), we can calculate that we need an incident power of $\frac{76 \times 0.5}{0.32 \times 5} = 24$ mW to obtain a ≃1 % overall

absolute reflectivity accuracy. This result is of course based on the proposition that the initial reflectivity is known within 0.5 %. Unfortunately, that is not always the case, especially not for interference structures such as silicon on sapphire where small variations in the Si thickness or angle of incidence can cause large reflectivity changes. Under those circumstances we estimated that the measured values were only accurate to within 10 %. An output power of 24 mW was not realistic for the AlGaAs diode laser but the responsivity of the photodiodes has increased to $\simeq$0.4 mA/mW for $\lambda = 820$ nm, which reduces the necessary power to an easily obtainable 12 mW.

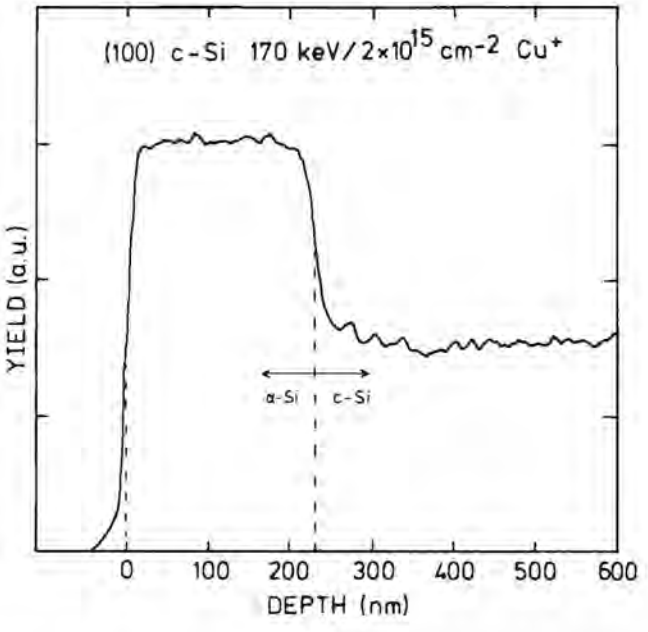

Figure II.12. RBS channeling spectrum after implantation of (100) c-Si with 170 keV Cu^+ ions to a dose of 2×10^{15} cm $^{-2}$. The thickness of the α-Si layer, determined from the FWHM values of the high yield portion in the spectrum, is 225 nm.

The preparation and characterization of α-Si is severely hindered by the fact that it is not a well defined structure or in other words: "what is amorphous silicon ?". Most techniques do not see any difference between p- and α-Si. Only cross-section TEM can give a positive identification but is, unfortunately, not very easy and moreover rather local. There are two main methods of preparing α-Si: evaporation and ion-implantation. The evaporation technique can give large areas of α-Si in a relatively short time. These α-Si films, however, often contain voids and a large concentration of hydrogen, incorporated during evaporation. Moreover, the structure of the layer depends in an involved way on parameters such as evaporation rate and substrate temperature. The fabrication of α-Si by ion-implantation of c-Si is a rather well defined and controlled method. Since the process has been studied thoroughly, the parameters needed

to obtain a really amorphous layer are known. This reduces the characterization to a determination of the α-Si thickness by RBS channeling measurements. A disadvantage is that it can not handle large areas in a short time. On the other hand, the layers do not contain hydrogen or voids. The Si is often amorphized by implantation with elements like Cu, Zn and In, which have a low solubility in the solid and a high solubility in the liquid. These impurities accumulate at a solid-liquid interface (segregation) so that the direction and covered distance of the solidification front(s) can be determined by RBS from the redistribution of the implanted species.

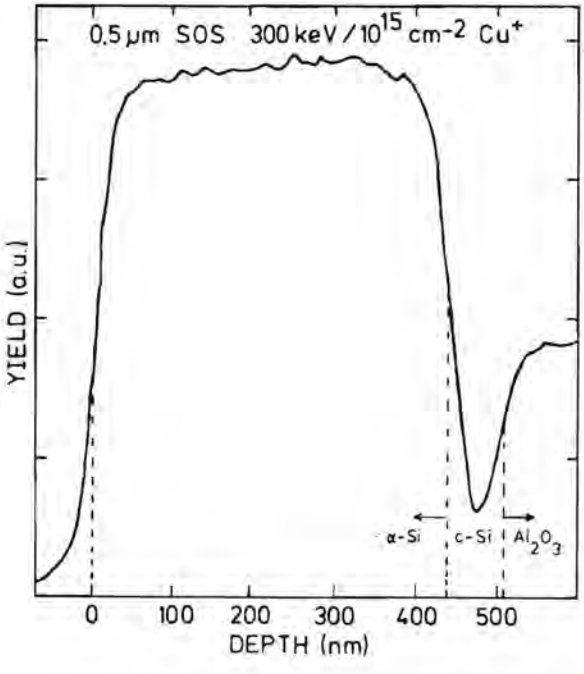

Figure II.13. RBS channeling spectrum after implantation of 0.5 μm (100) c-Si on sapphire with 300 keV Cu^+ ions to a dose of $10^{15}\,cm^{-2}$. The α-Si thickness, determined between the FWHM points of the high yield portion in the spectrum, is 440 nm.

All of our α-Si samples were prepared by ion implantation. Three types of samples can be distinguished: 225 nm Cu implanted α-Si on a c-Si substrate, 440 nm Cu implanted α-Si on top of 60 nm c-Si on sapphire, and 230 nm Si im-

planted α-Si on c-Si. The first type of sample was obtained by implantation of (100) c-Si with 170 keV Cu^+ ions to a dose of $2 \times 10^{15}\,cm^{-2}$. The material was then analysed by RBS channeling measurements to get the α-Si thickness, the results of which are shown in figure II.12. From the FWHM value of the high yield portion of the spectrum, an amorphous layer thickness of 225 nm can be inferred.

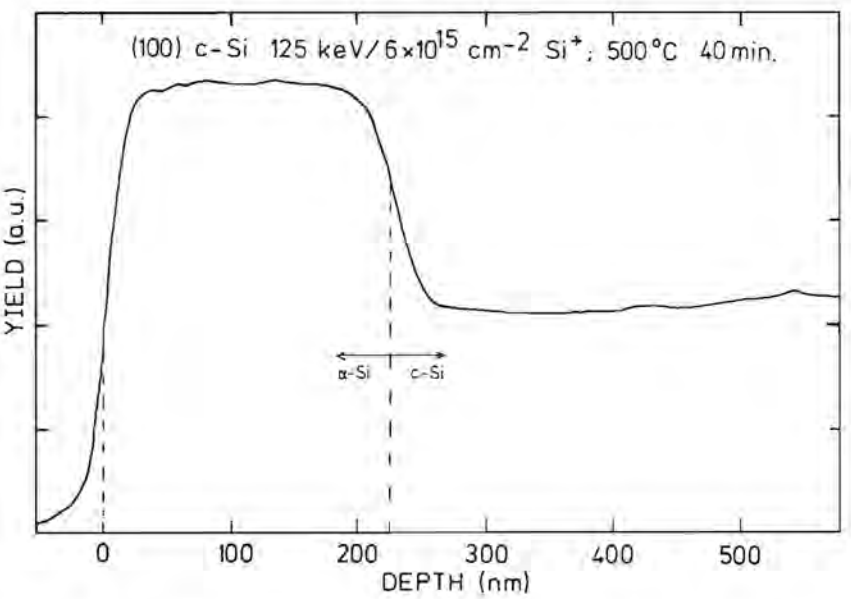

Figure II.14. RBS channeling spectrum after implantation of (100) c-Si with 125 keV Si^+ ions to a dose of $6 \times 10^{15}\,cm^{-2}$, followed by an annealing step at 500 °C for 40 minutes. The thickness of the resulting α-Si layer, deduced from the high yield portion of the spectrum, is 230 nm.

The second type of sample was obtained by implantation of a 0.5 μm thick c-Si layer on sapphire with 300 keV Cu^+ to a dose of $10^{15}\,cm^{-2}$. Again, the resulting amorphized layer thickness was determined by RBS. Figure II.13 presents the result, showing a FWHM value of 440 nm. Finally, the third and last type of sample was made by the bombardment of (100) c-Si with 125 keV Si^+ ions to a dose of $6 \times 10^{15}\,cm^{-2}$. The RBS analysis gave a resulting α-Si layer of 264 nm. To obtain a thickness as close as possible to the value for the first type of samples, the material was heated to 500 °C and kept at that temperature for about

40 minutes to decrease the α-Si thickness by SPE growth. This procedure delivered an amorphous layer depth of 230 nm, as can be deduced from the RBS spectrum of figure II.14. In all cases the specimen was kept at ≃10 °C by water cooling during implantation.

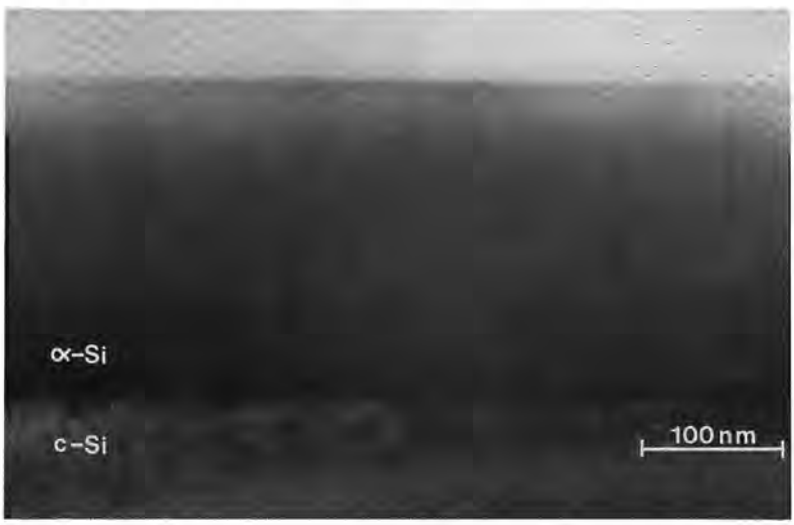

Figure II.15. TEM image of the as-implanted 225nm α-Si layer.

Some of the irradiated spots were investigated by cross-section TEM. The specimens were prepared by polishing and finally ion milling. A Philips EM400T microscope, operated at 120 keV, was used to obtain the micrographs. Since solidification phenomena, such as the nucleation of p-Si, can be of a random nature, our conclusions concerning these features are drawn on basis of relative abundances averaged over distances far beyond their characteristic dimensions (≃1 μm). Figure II.15 shows a cross-section TEM image after implantation of (100) c-Si with 170 keV Cu^+ ions to a dose of $2 \times 10^{15}\,cm^{-2}$. The amorphous layer thickness of 225 nm, determined by RBS, is in excellent agreement with the result obtained from TEM. A similar picture was taken for the Si implanted α-Si sample, giving the same good agreement between RBS and TEM.

References Chapter II

Cullis, A.G., Webber, H.C., and Bailey, P. (1979); J. Phys. E **12** , 688.

Born, M. and Wolf, E. (1983); *Principles of Optics* (Pergamon Press, Oxford, 1983), page 395.

Hill, C. (1982); *Laser Annealing of Semiconductors* edited by J.M. Poate and J.W. Mayer (Academic Press, New York, 1982), page 479.

Pittaway, L.G. (1964); Brit. J. Appl. Phys. **15**, 967.

III. EXPERIMENTAL RESULTS

III.1 Introduction

As mentioned in the statement of the problem, section I.2, this thesis is written with the intention to bring some order in the multitude of pulsed-laser irradiation experiments on α-Si. To do this we have made a systematic study of the influence of the pulse duration, α-Si thickness, impurities and energy-density on the melt and solidification behaviour of implantation amorphized Si, on pulsed-laser annealing. The various phase change phenomena were observed and analysed by time-resolved and static reflectivity measurements, Rutherford backscattering spectroscopy, transmission electron microscopy, and energy dispersive X-ray (EDX) analysis to gain as much insight as possible. In the remaining part of this introduction we present the conceptual framework which will be used to interpret the experimental results. This section is followed by a description of the data on the irradiation of 225 nm, Cu implanted and 230 nm, Si implanted α-Si on c-Si with 7.5 ns FWHM pulses from a frequency-doubled Nd:YAG laser. Section III.3 contains our study on the influence of the pulse duration on the transition between amorphous regrowth and XCR. The importance of the α-Si thickness is discussed in section III.4 and the fifth and last section contains a discussion of the data on the irradiation of 225 nm α-Si on c-Si with 32 ns FWHM pulses from a ruby laser.

The observation that amorphous regrowth and the formation of p-Si can occur inhomogeneously across a laser spot of uniform energy-density (Bruines et al. 1987a) suggests that the p-Si is randomly nucleated. As will be shown, all our data indicate that this nucleation occurs at the l-Si/α-Si interface. The initiation and growth of the p-Si is governed by the temperature and lifetime of the melt. Therefore, the conditions for amorphous regrowth and the formation of p-Si respectively, are a complicated function of the laser wavelength, pulse duration, energy-density, and the α-Si layer thickness. In the following discussion it will be assumed that the optical absorption length is much smaller than the theoretical thermal penetration depth, $\alpha^{-1} \ll \sqrt{\pi D t}$, and that the α-Si thickness

is infinite. Superheating and undercooling are defined with respect to the melting point of α-Si. Two extreme conditions can now be distinguished:

1. For low intensities, long pulse lengths and low energy-density, melting will be slow and the superheating of the l-Si relatively small. Moreover, a long pulse duration will cause a small temperature gradient and thus a low solidification velocity, little undercooling, and a long lifetime of the melt.

2. For high intensities, short pulse lengths and high energy-density, melting will be fast and the superheating relatively high. A short laser pulse will cause a large temperature gradient in the underlying amorphous material. This results in a high solidification velocity with a correspondingly large undercooling and short lifetime of the melt.

The role of the energy-density and a finite α-Si thickness can be seen in the following way. In general, a higher energy-density will lead to a larger melt depth, higher melt velocity, higher l-Si temperature, and a thinner remaining unmelted α-Si layer. Since the thermal conductivity of both l-Si and c-Si is much larger than that of α-Si, most of the temperature difference between the liquid-solid interface and the substrate is accommodated in the α-Si. If the thickness of this layer becomes less than the theoretical thermal penetration depth the temperature gradient will increase. A larger optical absorption length, i.e. longer laser wavelength, decreases the temperature gradient. The consequences of this framework for the experiments in the next three sections are discussed and illustrated in the following paragraph.

Firstly we consider the irradiation of 225 nm α-Si on c-Si with 7.5 ns pulses from a frequency-doubled Nd:YAG laser. After 10 ns, the theoretical thermal penetration depth in an infinite α-Si layer has the value of $\sqrt{\pi Dt} = \sqrt{\pi \times 10^{-8}\,s \times 10^{-6}\,m^2s^{-1}} = 177$ nm. The effective thermal penetration depth will be even larger because the optical absorption length ($\simeq$50 nm at $\lambda = 532$ nm and $\simeq$200 nm at $\lambda = 694$ nm) must also be taken into account. As mentioned, the thickness of the α-Si layer will determine the temperature gradient whenever the theoretical thermal penetration depth is of the same order. For the stated experimental conditions, the effective thermal penetration depth already equals the unmelted α-Si thickness at moderate energy-densities. The irradiation of the

same material with 18 ns pulses from the same frequency-doubled Nd:YAG laser has the following consequences. Since the theoretical thermal penetration depth has increased, the temperature gradient will now always be dominated by the remaining α-Si thickness, irrespective of the energy-density. So despite the more than doubled pulse duration, the heat-flow has not changed much with respect to the situation discussed above. For a given melt depth, however, the melt velocity will be lower and the associated superheating smaller. It is clear from the previous discussion that the temperature gradient will no longer be determined by the unmelted α-Si layer upon irradiation of 440 nm α-Si on 60 nm c-Si on sapphire with 7.5 ns pulses from a frequency-doubled Nd:YAG laser. The fact that the bulk of the substrate is sapphire does not really matter. Because the thermal properties of sapphire are not very different from those of c-Si at room temperature and because the thick α-Si layer shields the influence of the substrate up to large melt depths. Since the material is again annealed with the short 7.5 ns pulses, the melt velocities and superheating will be comparable to those in the first treatment.

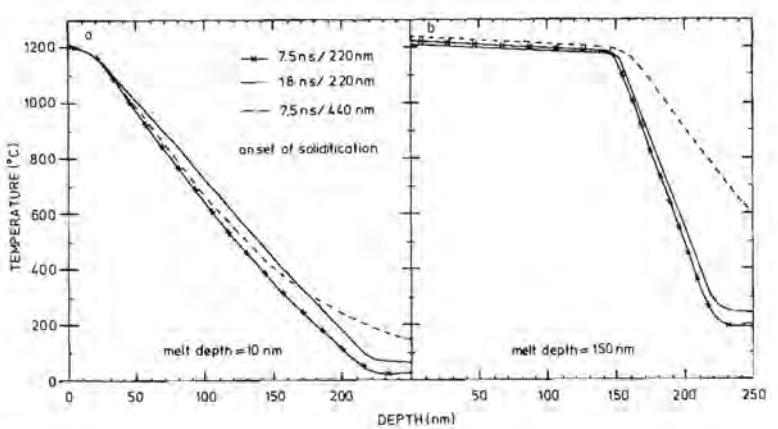

Figure III.1. Simulated temperature profiles, taken at the onset of solidification and upon irradiation with a frequency-doubled Nd:YAG laser, for 220 nm α-Si on c-Si and a 7.5 ns pulse (crosses), the same material but now with an 18 ns pulse (full line), 440 nm α-Si on 60 nm c-Si on sapphire again with a 7.5 ns pulse (dashed line), and for a melt depth of ≃10 nm (a) as well as ≃150 nm (b).

These considerations are further illustrated in figure III.1. It shows simulated temperature profiles, taken at the onset of solidification, for the three sets of experimental conditions discussed. The energy-densities are such that the calculations give a melt depth of (a) $\simeq$10 nm and (b) $\simeq$150 nm. The temperature profiles depicted in figure III.1a do not show large differences from each other. The two curves for the 7.5 ns pulse (crosses and dashed line) are nearly identical up to $\simeq$100 nm. Beyond this depth, the temperature gradient for the 440 nm α-Si decreases (dashed line) while that of the 220 nm layer continues with the same slope up to the α-Si/c-Si interface, where it flattens out (crosses). The comparison of the two curves for the 220 nm α-Si layer (full line and crosses) shows that there is some influence of the pulse duration on the temperature profile at this small melt depth. This influence is negligible for a melt depth of $\simeq$150 nm, figure III.1b, where the temperature gradient is completely dominated by the thickness of the remaining α-Si layer. However, the curve for the 440 nm layer exhibits the same temperature gradient across the α-Si as in figure III.1a. This signifies that the theoretical thermal penetration depth is still below the unmelted α-Si thickness of 440-150 = 290 nm.

More general information such as the melt depth and average melt velocity versus energy-density is given in each following section.

III.2 The Observation of Regrowth from the Surface upon Irradiation of α-Si on c-Si by 7.5 ns FWHM Pulses from a Frequency-Doubled Nd:YAG Laser

In this section we present the results obtained upon irradiation of an ≃225 nm thick, Cu implanted α-Si layer on a c-Si substrate with pulses of 7.5 ns FWHM duration from a frequency-doubled Nd:YAG laser. Part of this data has been published in Applied Physics Letters **48**(19), 1252-1254 (1986); Proceedings of the XIth Congres on Electron Microscopy, Kyoto 1986, pages 1521-1522; Applied Physics Letters **50**(9), 507-509 (1987); and Materials Research Symposium Proceedings **74** , 91-102 (1987).

III.2.1 Time-resolved reflectivity measurements on Cu implanted α-Si

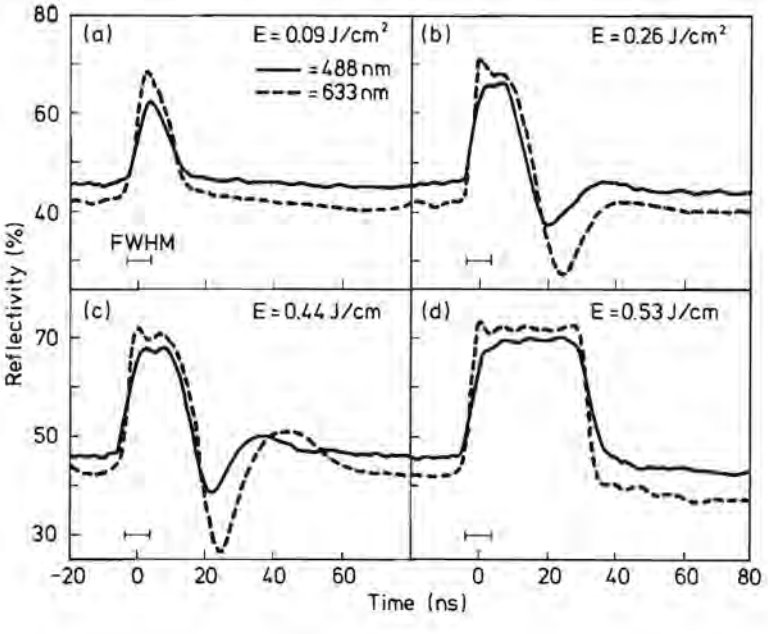

Figure III.2. Time-resolved reflectivity data at $\lambda = 488$ nm and $\lambda = 633$ nm of 225 nm, Cu implanted α-Si on c-Si upon irradiation with a 7.5 ns FWHM pulse from a frequency-doubled Nd:YAG laser at: (a) 0.09, (b) 0.26, (c) 0.44, and (d) 0.53 Jcm^{-2}. The top of the laser pulse is taken as origin of the time scale.

Figure III.2 shows the TRR data for both $\lambda = 488$ nm and $\lambda = 633$ nm upon irradiation of a 225 nm thick, Cu implanted α-Si layer on a c-Si substrate at four energy-densities. At an energy-density of 0.09 Jcm^{-2}, figure III.2a, the reflectivity rises to a value close to that of l-Si, indicating surface melting. Subsequently, the reflectivity drops and shows no further structure. The fact that the reflectivity does not show a high reflectivity plateau (HRP) indicates that the melt did not extend more than two optical penetration depths, $d_{melt} < 2\alpha_{l\text{-}Si}^{-1} \simeq 20$nm. Note that the reflectivity for $t = 80$ ns (R_{80}), which was always found to be approximately identical to that for $t = \infty$ in these experiments, equals that of α-Si. In figure III.2b, at 0.26 Jcm^{-2}, the TRR shows a HRP during ≃6 ns, which is followed by a minimum. The minimum in the reflectivity at 488 nm is reached ≃4 ns before the one at 633 nm. This time R_{80} is somewhat below that of α-Si, which is most obvious at $\lambda = 633$ nm. At an energy-density of 0.44 Jcm^{-2}, figure III.2c, the HRP duration has only slightly increased to ≃8 ns. The minimum after the HRP is now followed by a maximum. Here the minimum (maximum) at 488 nm occurs ≃3 ns (≃7 ns) earlier than the one at 633 nm. R_{80} again equals that of α-Si, just as at 0.09 Jcm^{-2}. Figure III.2d shows the TRR at 0.53 Jcm^{-2}. Except for the HRP, which now lasts ≃30 ns, there is no further structure in the reflectivity. Note that the duration of this HRP is extremely long compared to those of figures III.2b and 2c. The reflectivity value at $t = 80$ ns is considerably below that of α-Si

III.2.2 Cu redistribution results

After irradiation the spots were examined with RBS to determine the changes in the Cu profiles. Figure III.3 presents a comparison between Cu profiles before and after annealing with the energy-densities discussed in figure III.2. In figure III.3a, for 0.09 Jcm^{-2}, the Cu profile has not changed within the resolution of RBS (≃15 nm), indicating that only a very thin layer has been melted. Figure III.3b, for 0.26 Jcm^{-2}, shows a Cu profile after irradiation which has changed over 120 nm. This signifies that melting has occurred to this depth. There is a distinct peak in the RBS spectrum ≃40 nm below the surface indi-

cating the presence of a buried Cu layer. At 0.44 Jcm^{-2}, figure III.3c, the melt depth has increased to 200 nm and the peak in the Cu concentration is observed

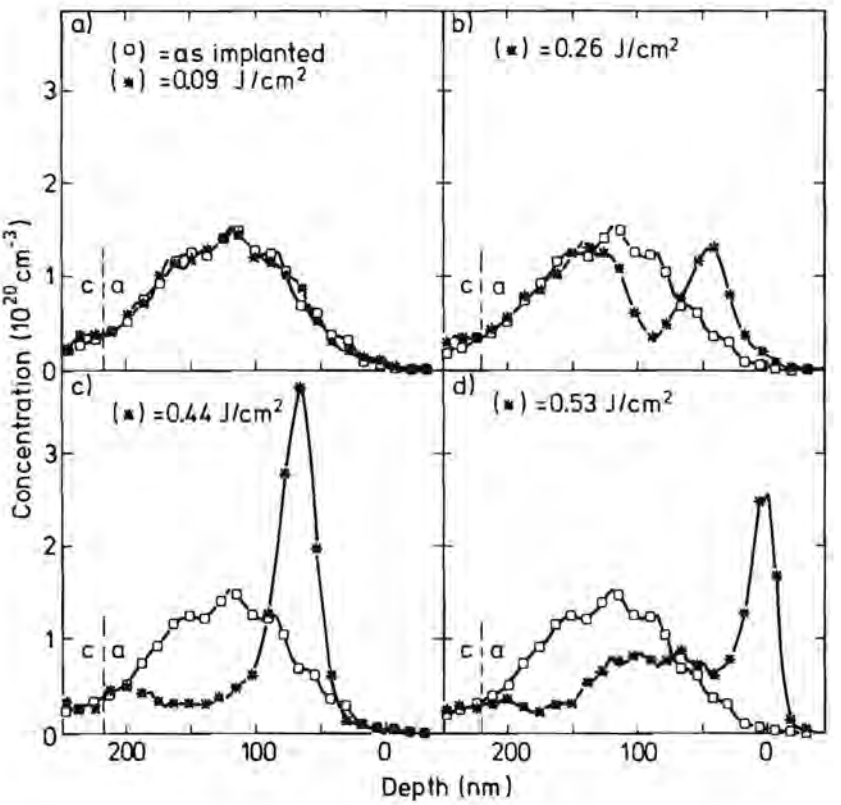

Figure III.3. Cu concentration profiles before and after irradiation at the energy-densities of figure III.2, as determined by RBS. Depth resolution ≃15 nm.

≃70 nm below the surface. The changes in the Cu profile at 0.53 Jcm^{-2}, figure III.3d, indicate that the entire α-Si layer has been melted. The distinct buried Cu layer is now absent and instead a Cu peak appears at the surface. RBS channeling measurements show a lowered yield in the regrown layer. Both the Cu segregation towards the surface and the increased channeling signify epitaxial growth. The Cu profiles after irradiation with an energy-density above 0.09 and below 0.53 Jcm^{-2} resemble the results of Campisano et al. (1985) ob-

tained on annealing of 130 nm, In implanted α-Si on c-Si with 2.5 ns FWHM ruby laser pulses, see section I.2.

III.2.3 Reflectivity calculations

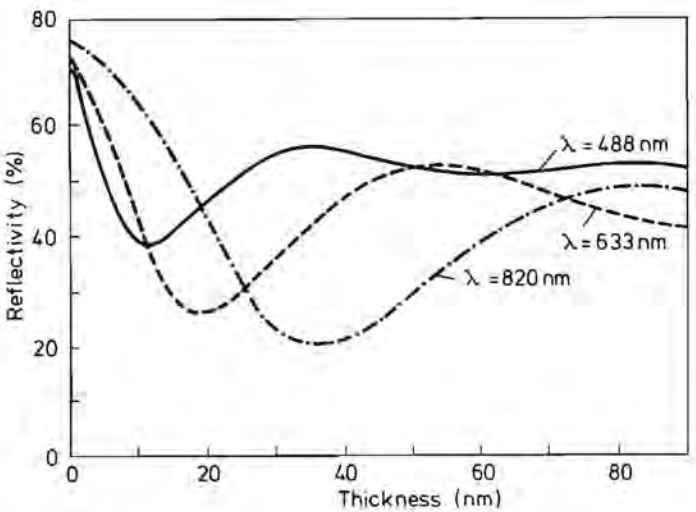

Figure III.4. Calculated reflectivity at 488, 633, and 820 nm for a solid α-Si layer on top of l-Si as a function of the position of the solid-liquid interface beneath the surface. The refractive index is taken as that of c-Si at a temperature of 1450 K. The absorption coefficient was adjusted to fit the calculations with the data of figures III.2b and 2c, with the following results: $\alpha_{488} = 5.3 \times 10^7\ m^{-1}$, $\alpha_{633} = 2.5 \times 10^7\ m^{-1}$, and $\alpha_{820} = 1.6 \times 10^7\ m^{-1}$

The results from figures III.2 and 3 all indicate the following process: At low energy-density only a thin layer of α-Si is melted; no structure is observed in the TRR and the Cu profile is unaffected (figures III.2a and 3a). At increasing energy-density the melt depth increases and solidification into α-Si takes place from both the interior and the surface. The solid-liquid front moving inwards from the surface gives rise to minima and maximum in the TRR (figures III.2b and 2c), caused by the interference of light reflected from the air-solid (surface) and the propagating solid-liquid interface. Cu is segregated at both solidification fronts and is accumulated where they collide, giving rise to a buried Cu layer (figures III.3b and 3c). Both the maximum melt depth and the

thickness of the regrown surface layer increase with increasing energy-density. Thus the Cu layer shifts inwards and the number of observed interference extrema increases. Epitaxial growth occurs for the energy-density at which the undercooled l-Si reaches the c-Si substrate. In that case the single solidification front causes the Cu to segregate towards the surface (figure III.3d). Since there is no growth from the front, the TRR will not show any structure apart from a HRP (figure III.2d).

In figure III.4 we present reflectivity calculations for a solid α-Si layer on top of l-Si as a function of the position of the solid-liquid interface beneath the surface. The index of refraction of α-Si is not expected to differ much from that of c-Si for the two probe wavelengths (488 nm and 633 nm). Therefore the refractive index of the top layer has been taken as that of c-Si at 1450 K, being roughly the melting temperature of α-Si, in the calculations. Since the temperature dependence of the absorption coefficient for α-Si is unknown, it was used as a fitting parameter. The resulting values for the absorptive power α are between those of c-Si at its melting point (1685 K) and those of l-Si. Using the measured positions in time of the reflectivity extrema at $\lambda = 633$ nm in figures III.2b & 2c and the calculated layer thicknesses for which these extrema should occur, see figure III.4, a mean velocity for growth from the surface can be deduced. For 0.26 Jcm^{-2}, figure III.2b, this results in a value of $\simeq 1.2$ m/s between the onset of growth and the minimum in the reflectivity. For 0.44 Jcm^{-2}, figure III.2c, the mean velocity, now deduced between the onset of growth and the maximum in the reflectivity, is $\simeq 1.6$ m/s.

III.2.4 Transmission electron microscopy results of the Cu implanted α-Si

In this section we present TEM results of the same spots which have been discussed above in the framework of growth from the surface. Except for the R_{80} value at 0.26 Jcm^{-2}, all experimental evidence for energy-densities below 0.53 Jcm^{-2} shown so far points towards growth of α-Si from both the interior and the surface. Cross-section TEM images, however, reveal that p-Si has also been formed. Figure III.5 shows a typical TEM result after irradiation at 0.26 Jcm^{-2}. Two regions can be distinguished: (a) Amorphous silicon with a narrow

stripe of segregated Cu, ≃40 nm beneath the surface. (b) Polycrystalline silicon in a matrix of α-Si. Some of the p-Si patches

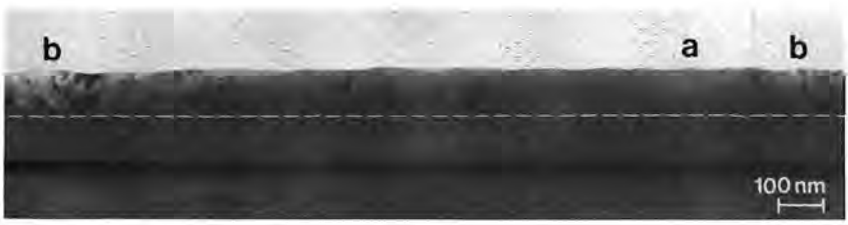

Figure III.5. TEM overview of the solidification phenomena observed after irradiation of 225 nm α-Si on c-Si with a 7.5 ns / 0.26 Jcm^{-2} pulse from a frequency-doubled Nd:YAG laser: (a) only α-Si with a narrow stripe of segregated Cu ≃40 nm below the surface, (b) p-Si in a matrix of α-Si. The average melt depth of 120 nm is indicated by the dashed line.

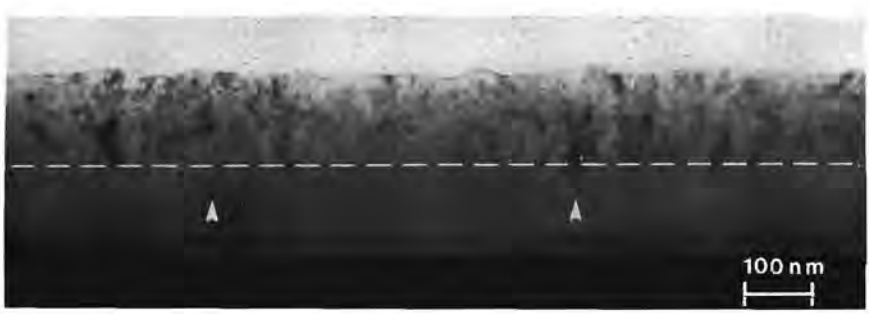

Figure III.6. TEM image after irradiation at 0.26 Jcm^{-2}. The arrows point towards p-Si patches that exceed the average melt depth, indicated by the dashed line.

extend to the surface while others are sandwiched between two α-Si layers. No regular pattern could be found in the occurrence of the p-Si regions, which indicates that they are not caused by spatial variations in the energy-density as might e.g. result from diffraction at dust particles. The relative abundances of the two forms of solid material, as determined at the depth of the buried Cu

layer and averaged over a distance of 30.5 μm, are: $\simeq$5 % α-Si with a clear Cu stripe (a) and $\simeq$95 % p-Si embedded in amorphous material (b).

Another observation at this energy-density is presented in figure III.6. The picture shows p-Si patches which have an in-depth extension beyond the average melt depth determined by RBS, see figure III.3b and 13. This suggests that the formation of p-Si has the character of XCR.

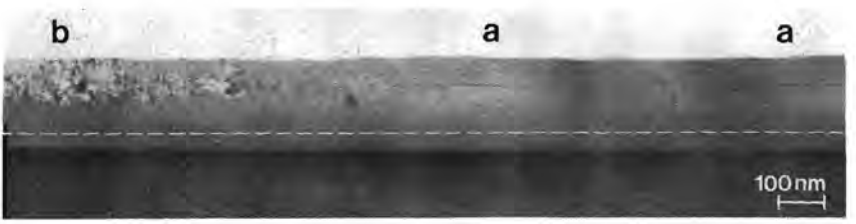

Figure III.7. Typical TEM image of the solidification phenomena observed after irradiation at 0.44 Jcm $^{-2}$; (a) and (b) refer to solidification processes described in figure III.5 and the text. The dashed line $\simeq$190 nm below the surface indicates the average melt depth.

Figure III.8. Detail of a p-Si patch at 0.44 Jcm^{-2}. The structure exhibits a large wing centered around the buried Cu layer.

A typical TEM image for an energy-density of 0.44 Jcm^{-2} is shown in figure III.7. In comparison with figure III.5, for 0.26 Jcm^{-2}, the buried Cu layer shows up more often and the amount of p-Si at the surface has decreased. The average abundances again determined at the position of the Cu stripe but this time over a length of 80.2 μm, are: $\simeq$35 % pure α-Si (a) and $\simeq$65 % p-Si in a matrix of

amorphous silicon (b). Figure III.8 presents a p-Si patch in more detail. An interesting feature is that the FG p-Si region in this picture exhibits a large wing, centered around the buried Cu line. This is in fact observed for all p-Si regions, irrespective of the energy-density. In three dimensions these p-Si patches have the shape of a lens with a flattend top and its brim at the Cu stripe.

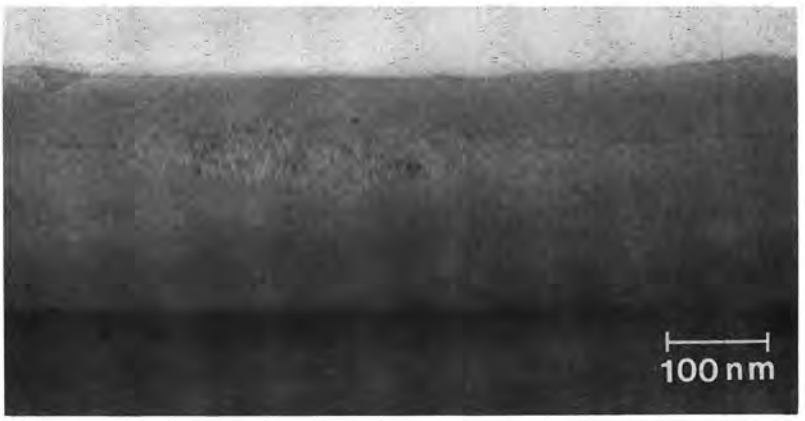

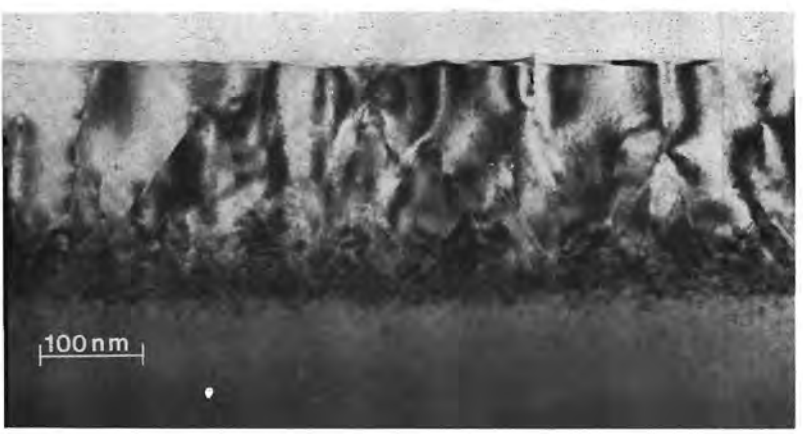

Figure III.9 shows a lens shaped p-Si patch which does not reach the surface. The centering around the buried Cu line is again evident. It is unclear whether this structure is a phenomenon on itself or a cross-section through the outer

range of a larger lens shaped p-Si region. For 0.44 Jcm^{-2}, the p-Si patches have an extension in depth which is substantially smaller than the average melt depth of 190 nm, previously determined by RBS (figures III.3c and 13). Finally, figure III.10 gives a TEM image of the regrown layer at 0.53 Jcm^{-2}. It is clear that epitaxial regrowth has occurred although the layer contains many twins.

At this point we state the following hypothesis concerning the melt and solidification processes for these experimental conditions. The absorbed energy of the laser pulse first melts the α-Si. Epitaxial growth occurs if the l-Si layer reaches the c-Si substrate. In all other cases solidification starts with the growth of α-Si from the interior liquid-solid interface. The with this growth associated undercooling of the l-Si initiates growth of α-Si from the surface. P-Si is nucleated at a liquid-solid front during the last stage of solidification, i.e. when the remaining l-Si layer has become thin (<40 nm). The nature of the nucleation mechanism itself is unknown. It could e.g. be heterogeneous nucleation (Tsao and Peercy; 1987) or nucleation in solid α-Si (Roorda et al. 1988). The above formulated hypothesis is consistent with a number of observations:

(1) Heat-flow calculations of the melt depth were in good agreement with those determined by RBS, although a release of latent heat by the formation of p-Si was not taken into account. This implies the existence of separate melt and solidification phases as well as that p-Si must have been formed after melt-in. Thus the latent heat was not used to increase the melt depth but to extend the lifetime of the melt.

(2) TEM revealed that the buried Cu layer was only visible for a very limited fraction. EDX measurements indicated that the Cu line was still present in the p-Si regions and RBS clearly showed a pronounced peak. At the same time large amounts of p-Si could be distinguished, which were not expected to accumulate Cu at all, but to broaden the Cu profile. These observations indicate that the segregation of Cu had already begun at the moment the nucleation of p-Si started.

(3) The reflectivity calculations were performed with a single valued absorption coefficient. Since they are in good agreement with the measurements,

at least up to the maximum in the reflectivity at 55 nm for $\lambda = 633$ nm, the major part of the p-Si must have been formed when the l-Si layer was becoming optically thin.

(4) The stated hypothesis also explains the centering of the FG p-Si wings around the Cu stripe. After nucleation, growth will be easiest in the lateral direction, where there is still a thin l-Si layer, and more difficult in the other direction, where the melt has already solidified into α-Si. The Cu distribution will not be changed drastically by the p-Si, since its growth perpendicular to the surface takes place through an area where the Cu has already been depleted.

The difference between the refractive index of α-Si and that of p-Si is small, which explains why the value of the end-reflectivity (R_{80}) is not severely influenced by the presence of p-Si. Moreover, the penetration depth in α-Si is 40 nm at $\lambda = 488$ nm and $\simeq 150$ nm at $\lambda = 633$ and 647 nm. The reflectivity at 488 nm is therefore only sensitive to changes in the optical properties near the surface, while that at 633 and 647 nm is influenced by changes in a much thicker layer. The value of R_{80} at 0.26 Jcm^{-2} (figure III.2b), where both the total amount of p-Si and the amount of p-Si at the surface were large, is indeed slightly reduced with respect to that at t = -20 for both probe wavelengths. At 0.44 Jcm^{-2} (figure III.2c) this reduction has disappeared, in agreement with the TEM observation that the amount of p-Si has decreased with respect to that at 0.26 Jcm^{-2}.

The fact that both the total amount of p-Si and the amount of p-Si at the surface decrease with increasing energy-density may indicate that the nucleation of p-Si is hampered by the segregated Cu at the solidification fronts, as was proposed earlier by Cullis et al. (1984, 1986). A higher energy-density and thus larger melt depth, gives rise to higher Cu concentrations and consequently less nucleation. The effect of Cu on regrowth from the surface, solidification velocities, and the nucleation of p-Si will be discussed in the next sections.

III.2.5 Time-resolved reflectivity measurements on Si implanted α-Si

The influence of the implanted Cu on the melt and solidification behaviour described in the first part of this section was investigated by performing the

same experiments on samples which were amorphized by Si implantation, see section II.4. The original α-Si thickness after implantation was 265 nm. To be as close as possible to the former conditions, its thickness was brought back to 230 nm by solid phase epitaxial regrowth at 500 °C for 40 minutes.

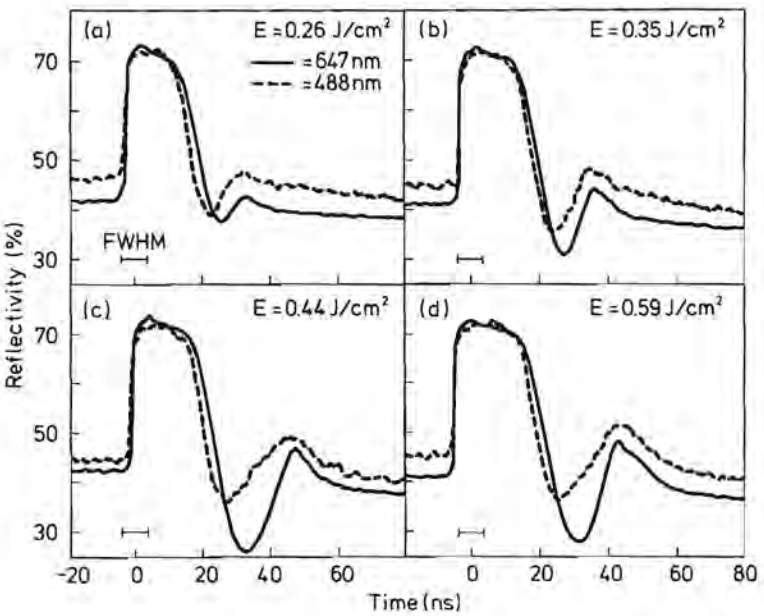

Figure III.11. TRR data at $\lambda = 488$ nm and $\lambda = 647$ nm of 230 nm, Si implanted α-Si on c-Si upon irradiation with a 7.5 ns FWHM pulse from a frequency-doubled Nd:YAG laser at: (a) 0.26, (b) 0.35, (c) 0.44, and (d) 0.59 Jcm^{-2}. The top of the laser pulse is taken as origin of the time scale.

The TRR signals upon irradiation of this material, again with 7.5 ns FWHM pulses from a frequency-doubled Nd:YAG laser, are given in figure III.11. Figure III.11a, for 0.26 Jcm^{-2}, shows a HRP with a duration of ≃10 ns. The minimum in the reflectivity after the HRP is much less pronounced for the Si implanted than for the Cu implanted material. However, the extremum at 488 nm is again reached before that at 647 nm. The end-reflectivity, for t = 80 ns, is lower than the value for α-Si, as was the case with the Cu implanted α-Si. At 0.35 Jcm^{-2} (figure III.11b) the duration of the HRP has increased to ≃13 ns. The minimum in the reflectivity is more distinct now with respect to

that of figure III.11a, however, its value (31 %) is still above the 27 % reached for 0.26 Jcm^{-2} in the case of the Cu implanted sample. Moreover, a small maximum can be distinguished. The fact that this maximum is reached simultaneously ($t \simeq 36$ ns) for both wavelengths indicates that the growth from the surface has stopped abruptly at this point. The end-reflectivity again has a value below that for α-Si. Figure III.11c, at 0.44 Jcm^{-2}, shows a HRP with a duration of $\simeq 15$ ns. The reflectivity value in the minimum (26 %) now equals that of the Cu implanted sample (figures III.2b and 2c). The minimum is also followed by a maximum, which occurs simultaneously ($t \simeq 48$ ns) for both wavelengths. Once more we observe that the end-reflectivity is considerably below that at the start of the experiment. The difference between the Si and the Cu implanted samples becomes even more striking for figure III.11d, at 0.59 Jcm^{-2}. The TRR does not indicate epitaxial growth here, which the Cu implanted material already showed at 0.53 Jcm^{-2}. This discrepancy, which will be shown to have no connection with the Cu, is treated in section III.2.7.

III.2.6 Growth velocity from the surface for the Si implanted α-Si

The above described TRR measurements suggest that the growth velocity from the surface is lower for the Si than for the Cu implanted material. A comparison between the TRR signals at 647 nm, presented in figure III.11, and the calculations in figure III.4 gives an average velocity of $\simeq 1$ m/s between the onset of growth from the surface and the occurrence of the minimum in the reflectivity at 0.26 Jcm^{-2}. The deduced velocity over the same range at 0.35, 0.44 and 0.59 Jcm^{-2} is $\simeq 1.1$ m/s. From figure III.11c, at 0.44 Jcm^{-2}, we also determined the average velocity over the interval between the onset of growth from the surface ($t \simeq 14$ ns) and the achievement of 45 % reflectivity after the minimum in the TRR ($t \simeq 32$ ns). The value of $\simeq 1.2$ m/s defined in this way, is only slightly higher than the average velocity over the interval from the onset of growth to the minimum and less than the $\simeq 1.5$ m/s determined over the same interval for the Cu implanted material. The difference between the growth velocities of the Cu and Si implanted sample is further illustrated in figure III.12. It shows the TRR signal during the amorphous regrowth phase of both the Cu

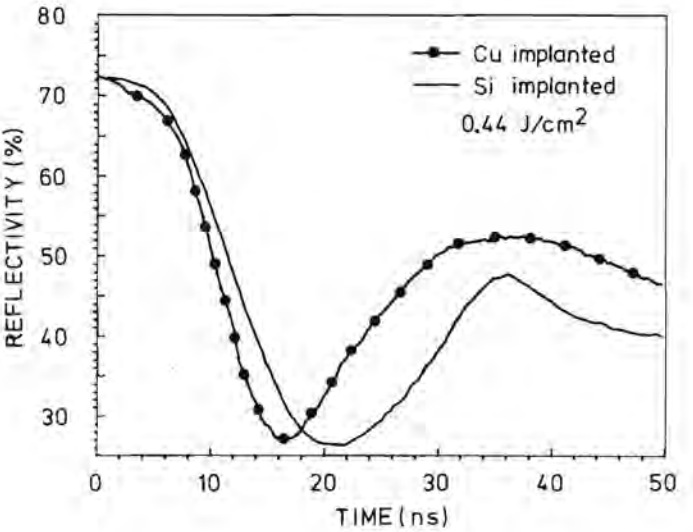

Figure III.12. Time-resolved reflectivity data during the amorphous regrowth phase of both the Cu (dotted line) and the Si (full line) implanted sample upon irradiation at 0.44 Jcm^{-2}. The origin of time is taken at the onset of solidification.

and the Si implanted material, irradiated at 0.44 Jcm^{-2} (figures III.2c and 11c). The onset of growth has been taken as the origin of time. Figure III.12 clearly shows that the TRR of the Cu implanted sample has a faster evolution in time than the Si implanted one. The difference can be explained by assuming that the segregated Cu hampers growth. This seems contradictory but one has to keep in mind that the sum of the solidification velocities is determined by the heat-flow, while their ratio is fixed by the undercooling at both interfaces. Any effect of the segregated Cu which influences this undercooling, e.g. a higher value of ζ or a melt temperature reduction, will be most severe at the interface with the highest concentration. Since the temperature always decreases with depth, the interior liquid-solid front will move the fastest thus accumulating the highest Cu concentration. As a result, the ratio between both velocities will tend to approach unity. Because the sum of both velocities is reasonably constant, this means that the velocity of growth from the surface increases. The effect of the Cu on the formation of p-Si is discussed in section II.2.8.

III.2.7 Melt depth/velocity calculations in comparison with the RBS data.

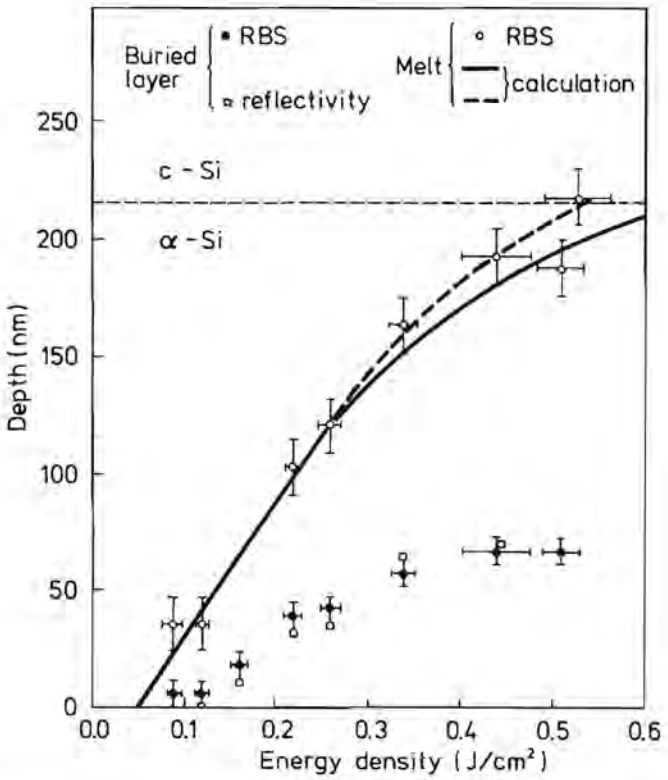

Figure III.13. (1) Melt depth as a function of energy-density. Results from the heat-flow calculations for both a 220 (full line) and 250 nm (dashed line) α-Si layer on c-Si in comparison with measurements from Cu redistribution profiles. The computer simulations were performed without superheating effects and with a slab size of 10 nm. (2) Position of the buried Cu layer as a function of energy-density. Estimates from the TRR data and values deduced from the Cu profiles after irradiation.

The positions of the buried Cu layer and maximum melt depth inferred from the RBS data are shown in figure III.13 as a function of energy-density. The melt depth has also been calculated using a heat-flow computer model, see chapter IV. The simulations for the 220 nm thick α-Si layer (full line) agree very well with the RBS measurements for low energy-densities. However, there is a discrepancy for energy-densities approaching the threshold for epitaxial

growth. As can be seen, the calculated melt depth exhibits a strongly decreasing slope for these energy-densities because of the increased heat-loss due to the presence of the c-Si substrate, which has a larger heat conductivity and thus acts as a heat sink. The data obtained with RBS do not show such a strong influence of the substrate. The calculations give a value of $\simeq 0.7$ Jcm^{-2} to melt the α-Si layer fully, while the experimental result is only 0.53 Jcm^{-2}. Since both the Cu and the Si implanted materials have the same energy-density for surface melting, it is unlikely that the difference is caused by an error in the determination of the pulse energy or by relaxation of the Si implanted sample during its short period of solid phase epitaxial regrowth. The effect of the Cu on the melt temperature and/or latent heat would have to be enormous to give the $\simeq 25$ % decrease in the threshold energy-density for epitaxial growth at a maximum concentration of <1 at.%. However, the discrepancy could be explained as follows: The Cu implanted sample contains an $\simeq 30$ nm thick, heavily damaged Si layer just below the α-Si . Such a layer is always present when implanting at room temperature. This heavily damaged layer could still act as a c-Si seed for epitaxial growth, while having the (low) thermal conductivity of α-Si . The effective α-Si thickness would then be larger, from a thermal point of view, thus reducing the influence of the c-Si substrate which has a higher thermal conductivity. Due to the special treatment of the Si implanted material, its damaged Si layer is both annealed and covered by a c-Si layer with less defects. Consequently, the reduction of the heat-flow to the substrate is less severe. This proposition was tested by a determination of the threshold for epitaxial growth of the originally 265 nm thick, Si amorphized sample. Although the α-Si layer is 35 nm thicker, epitaxial growth occurred at about the same energy density as with the annealed (230 nm) sample, which proves that the heavily damaged c-Si acts as described. Further evidence for the proposed behaviour of the damaged Si layer is given by the maximum melt depth calculations for a $220 + 30 = 250$ nm α-Si layer on c-Si (dashed line). It is clear that the data now fit with the measurements for all energy-densities. Additional computer simulations indicate an effective thermal α-Si thickness of 240 nm for the Si implanted sample. Since this is only 10 nm less than that of the Cu implanted

material, all further calculations regarding the Cu and the Si amorphized Si will be performed with an amorphous layer of 250 nm. This choice has a negligible effect on the heat-flow simulations for the Si implanted material as long as the melt depth is below ≃200 nm. The small difference in the effective thermal α-Si thicknesses also implies that the TRR signals of the Cu- and the Si implanted material can be compared on the basis of equal energy-density up to ≃0.44 Jcm^{-2}.

energy-density	.08 Jcm^{-2}	.17 Jcm^{-2}	.26 Jcm^{-2}	.35 Jcm^{-2}	.44 Jcm^{-2}
average melt velocity	4.2 m/s	8.0 m/s	11.1 m/s	14.6 m/s	16 m/s

Table IV. Calculated average melt velocities for $\zeta = 0$ upon irradiation of 250 nm α-Si on c-Si with a 7.5 ns FWHM pulse from a frequency-doubled Nd:YAG laser at 0.08, 0.17, 0.26, 0.35, and 0.44 Jcm^{-2}.

Table IV gives the average melt velocities at five energy-densities calculated without superheating ($\zeta = 0$) and for an effective α-Si thickness of 250 nm. The value of ζ does not greatly influence the velocity and melt depth, but does determine the superheating of the l-Si. It is clear that a ζ value of 7 K/(m/s), see section I.4, would give a considerable superheating with respect to the melting point of α-Si at the melt front. Moreover, the temperature at the surface must be even higher to provide the necessary heat-flow across the l-Si to give such a high melt velocity.

The position of the buried Cu layer has not only been deduced from the RBS data but also from a comparison between the TRR results and the reflectivity calculations. These estimates are found to be consistent with the values from the Cu redistribution, as can be seen in figure III.13, which justifies the use of the refractive index of c-Si for the reflectivity calculations in section III.2.3. Note that the position of the buried Cu layer is about 1/3 of the maximum melt depth, irrespective of energy-density. It can be shown that this results

from a difference in growth velocity rather than a difference in the time at which solidification starts (see section V.2). Consequently, the average velocity of growth from the rear must be approximately twice that from the surface.

III.2.8 TEM data of the Si implanted material

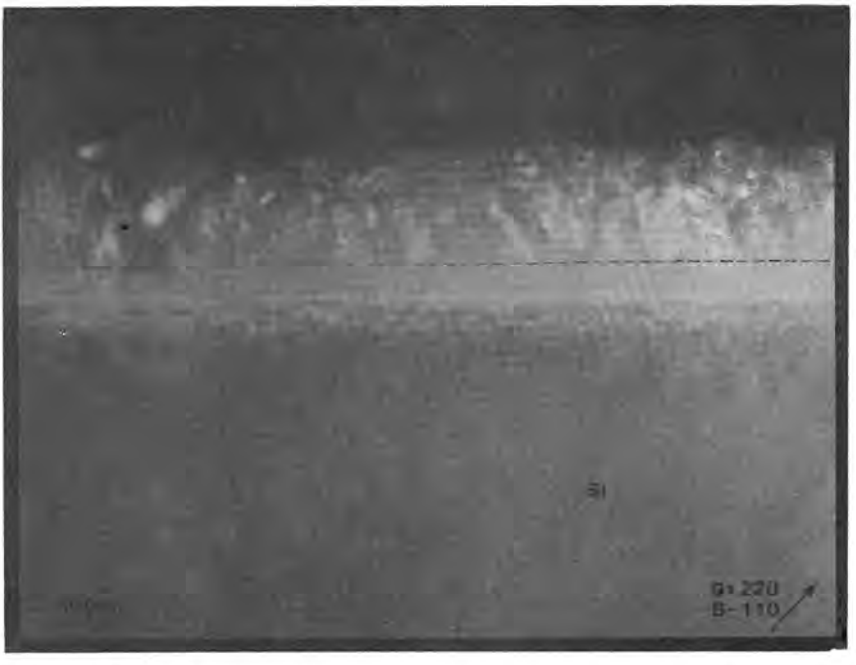

Figure III.14. TEM image characteristic for the Si implanted material after irradiation at 0.44 Jcm^{-2}. The dashed line indicates the calculated melt depth of $\simeq$180 nm.

Figure III.14 shows a typical TEM image of the Si implanted material after irradiation at 0.44 Jcm^{-2}. The dashed line in the figure indicates the calculated melt depth of $\simeq$180 nm. It is clear that nearly all the melted material has transformed into p-Si. This is in sharp contrast with the data for the Cu implanted sample, figures III.7-9, which showed both amorphous and polycrystalline material. A detail of the previous TEM image is given in figure III.15. This structure shows some resemblance to the lens shaped p-Si region of figure III.9. However, there is no α-Si at the surface. Note that the central part

of the structure exceeds the calculated melt depth. This has not been seen before at this energy-density for the Cu implanted material. Figure III.16 shows a typical TEM picture after annealing at 0.57 Jcm ^{2}. Again, the complete melted layer has turned into p-Si. A close examination of the p-Si structures revealed that the grain size at the interior is slightly coarser than that at the surface. It was not possible to distinguish two separate layers, however. This reversed order of the FG and LG p-Si regions has been observed before by Narayan and White (1984), also for a large melt depth. We will encounter the same situation again in chapter V, but for completely different circumstances.

Figure III.15. Detail of figure III.14. P-Si region showing some resemblance to the lens shaped p-Si structures found in the Cu implanted material after annealing at 0.44 Jcm^{-2} (figure III.9). The dashed line indicates the calculated melt depth of $\simeq$180 nm.

It is obvious from the TEM results presented above that the implanted Cu greatly reduces the nucleation of p-Si during amorphous regrowth. It does not seem to be unreasonable to state that all implanted species which show segre-

gation will give this effect. It is not clear whether the nucleation is mainly hampered by the segregated Cu itself or by its effect on the growth velocities. However, the presence of an element with a low solubility in solid Si, such as Cu, is known to influence nucleation (Roth and Olson, 1987).

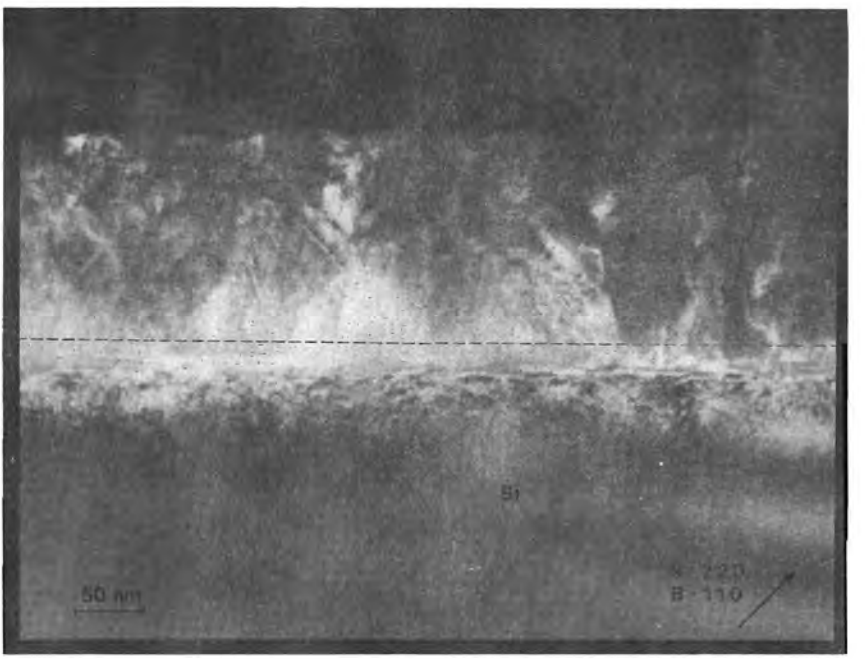

Figure III.16. Typical TEM result after irradiation of the Si implanted material at 0.57 Jcm^{-2}. The dashed line indicates the calculated melt depth of $\simeq$205 nm.

III.3 The Irradiation of 225 nm α-Si on c-Si with 18 ns Pulses from a Frequency-Doubled Nd:YAG Laser.

This section deals with the influence of the pulse duration on the transition between amorphous regrowth and XCR. To study this influence, an ≃230 nm thick, Si implanted α-Si layer on a c-Si substrate was irradiated by quasi 18 ns pulses from a frequency-doubled Nd:YAG laser (see section II.2.2). Similar data for Cu implanted material have been published in Materials Research Society Symposium Proceedings **74** (1987), 91-102.

III.3.1 Time-resolved reflectivity data obtained with quasi 18 ns FWHM pulses from a frequency-doubled Nd:YAG laser

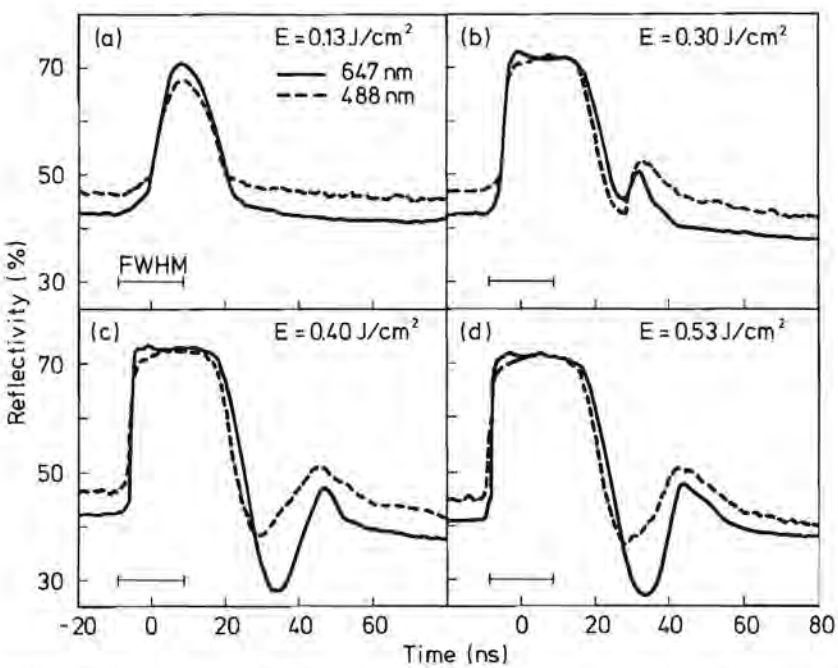

Figure III.17. Time-resolved reflectivity signals upon annealing of 230 nm thick, Si implanted α-Si with quasi 18 ns pulses from a frequency-doubled Nd:YAG laser at a) 0.13, b) 0.30, c) 0.40, and d) 0.53 Jcm^{-2}.

Figure III.17 presents TRR data at $\lambda = 488$ and 647 nm on irradiation of 230 nm, Si implanted α-Si on c-Si with quasi 18 ns pulses from a frequency-

doubled Nd:YAG. For this purpose, two 7.5 ns FWHM pulses were used with a delay of ≃10 ns between the pulses. The quasi FWHM of the pulse is depicted in the figure. Figure III.17a shows the TRR at a total energy-density of 0.13 Jcm^{-2}. The melt depth for these conditions is similar to that of figure III.2a, 7.5 ns and 0.09 Jcm^{-2}, so that both TRR signals can be compared. The only significant difference is that the end-reflectivity (R_{80}) is slightly below the value for α-Si now. The fact that figure III.2a contains TRR data for Cu implanted α-Si is not relevant for this low energy-density, since there is no significant segregation. However, this is not true for higher energy-densities, which must be compared with their counterparts in figure III.11. The result at 0.30 Jcm^{-2}, figure III.17b, can be compared with the 7.5 ns and 0.26 Jcm^{-2} experiment depicted in figure III.11A. The duration of the HRP is now ≃15 ns, 5 ns longer than for the 7.5 ns pulse. The HRP is followed by a minimum and a maximum in the reflectivity. Within the experimental error, both extrema are reached at the same moment in time, independent of the wavelength, indicating an abrupt end of growth from the surface. Moreover, the reflectivity value in the minimum, 43 %, is above the 37 % found in figure III.11A. The end-reflectivity is about that of c-Si. Figures III.17c and 17d, for 0.40 and 0.53 Jcm^{-2} respectively, are nearly identical. Both curves show a minimum and a maximum in the TRR as in figure III.17a. The reflectivity value in the minima, however, has decreased to ≃27 %, comparable to the value found in figures III.11C and 2c. Moreover, there is again a time delay between the time for which the minimum is reached at 488 nm and at 647 nm. The deduced velocity of growth, between the onset of solidification from the surface and the occurrence of the minimum at 647 nm, is ≃1 m/s for both curves. The value of the reflectivity at the maximum does not change much with increasing energy-density. The moment in time for which the maximum occurs is independent of the probe wavelength. Both observations indicate that the maximum in the reflectivity is not connected with growth from the surface. As expected, the end-reflectivity of curves III.17c and 17d is below the value for α-Si and about that of c-Si. Epitaxial growth occurred at an energy-density only slightly higher than that found upon annealing with 7.5 ns pulses, 0.70 respectively 0.63

Jcm^{-2}, which proves once more that the pulse duration has only a small influence on the heat-flow for this α-Si thickness.

III.3.2 Calculations of the melt depth/velocity versus energy-density

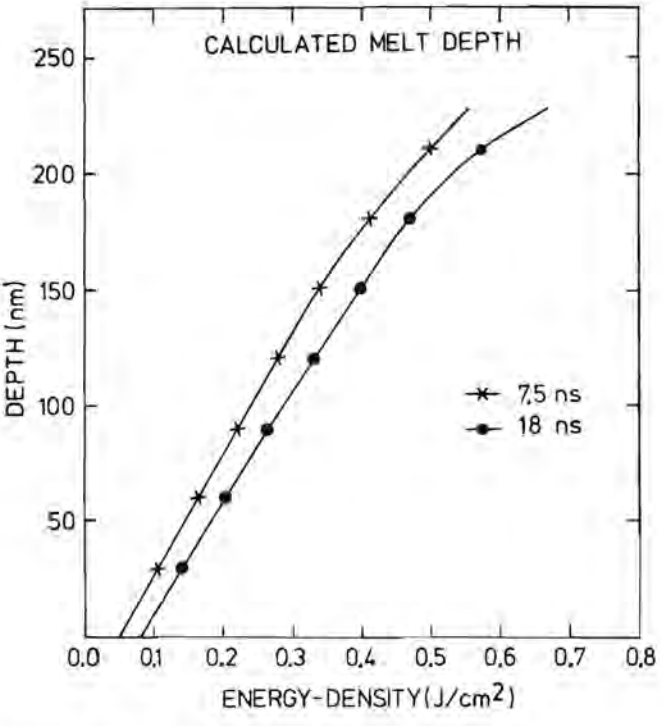

Figure III.18. Melt depth versus energy-density for the irradiation of 230 nm α-Si on c-Si with 18 ns FWHM pulses from a frequency-doubled Nd:YAG laser (dots), calculated without superheating and for dZ = 10 nm. The data for 7.5 ns FWHM pulses (crosses) are added for comparison.

The calculated melt depth versus energy-density for the annealing of 250 nm α-Si on c-Si with 18 ns FWHM pulses from a frequency-doubled Nd:YAG laser is illustrated in figure III.18 (dots). For comparison the results for the irradiation of the same material with pulses of 7.5 ns FWHM duration are added (crosses). The behaviour of the two curves is clearly similar, except that the one for the 18 ns pulses is shifted to higher energy-densities. The pri-

mary melt depth increases with (500 nm)/(Jcm^{-2}) for energy-densities below $\simeq$0.4 Jcm^{-2}. The figure also shows that the influence of the substrate on the increase of the melt depth with energy-density is more pronounced for the 18 ns pulses. This manifests itself in the reduced slope of this curve for melt depths above $\simeq$200 nm.

Table V gives the calculated average melt velocities. They are more than a factor of two smaller than the velocities for the 7.5 ns pulses at the same energy-density. For instance, an average melt velocity of $\simeq$8 m/s is obtained at 0.44 Jcm^{-2} for the 18 ns pulse and at 0.17 Jcm^{-2} for the 7.5 ns pulse. The pulse duration apparently has more effect on the melt velocity than on the maximum melt depth for these experimental conditions.

energy-density	.17 Jcm^{-2}	.26 Jcm^{-2}	.35 Jcm^{-2}	.44 Jcm^{-2}	.53 Jcm^{-2}
average melt velocity	3.6 m/s	5.3 m/s	7.0 m/s	8.1 m/s	9.1 m/s

Table V. Average melt velocities simulated for $\zeta = 0$ upon irradiation of 230 nm α-Si on c-Si with a 18 ns FWHM pulse from a frequency-doubled Nd:YAG laser at 0.17, 0.26, 0.35, 0.44, and 0.53 Jcm^{-2}.

III.3.3 Transmission electron microscopy results

Figures III.19a and 19b present TEM pictures which are characteristic for the structure after irradiation with a quasi 18 ns / 0.39 Jcm^{-2} pulse from a frequency-doubled Nd:YAG laser. Except for a small α-Si layer at the substrate, the pictures show only FG p-Si. This explains why the end-reflectivity value approached that of c-Si, see figure III.17c. The FG p-Si thickness always exceeds the calculated primary melt depth (dashed line) but shows local variations up to 60 nm or more, see e.g. figure III.19b.

The following picture emerges from the data concerning the annealing of 230 nm, Si implanted α-Si on c-Si with quasi 18 ns pulses from a frequency-doubled Nd:YAG laser. For small melt depths (low energy-densities),

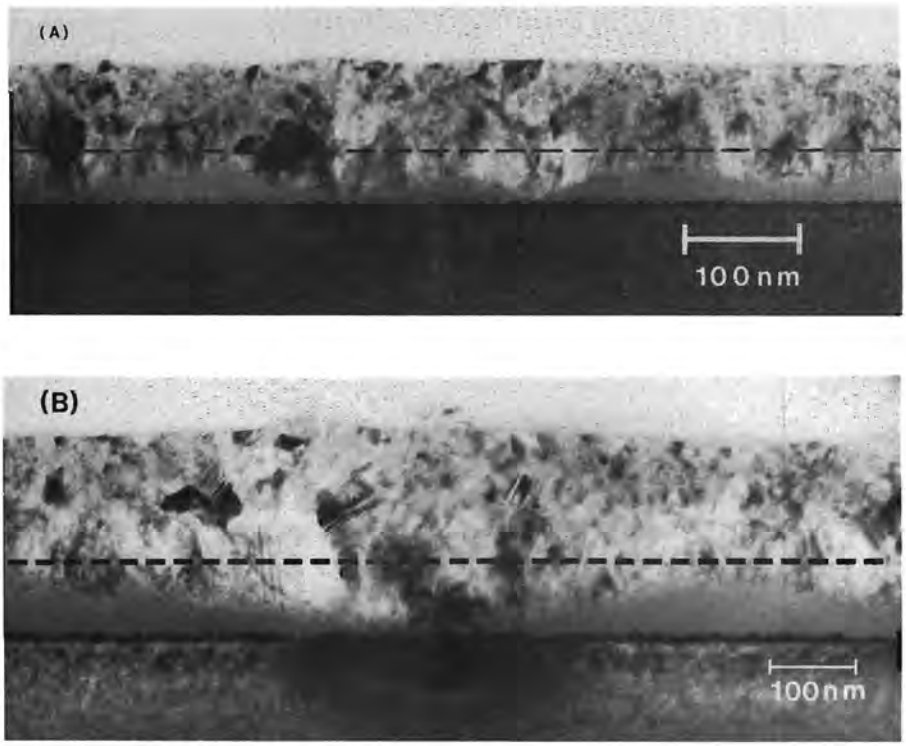

Figure III.19. Transmission electron microscopy images upon annealing of 230 nm α-Si on c-Si with a quasi 18 ns / 0.39 Jcm^{-2} pulse from a frequency-doubled Nd:YAG laser. The calculated primary melt depth of 140 nm is indicated by the dashed line.

solidification starts with amorphous growth from both the interior and the surface as with the 7.5 ns pulses. However, the longer pulse duration results in a smaller growth velocity, and solidification is interrupted by the formation of p-Si at a very early stage. The influence of the longer pulse duration on the growth velocity diminishes with increasing melt depth (energy-density). The formation of p-Si shifts to a later stage of solidification and the TRR data for the 7.5 and the 18 ns pulses become more and more similar at the same melt depth. However, the always somewhat lower cooling rate for the 18 ns case results in the formation of slightly more p-Si than with the 7.5 ns pulses.

III.4 The Annealing of 440 nm α-Si on 60 nm c-Si on Sapphire with 7.5 ns FWHM Pulses from a Frequency-Doubled Nd:YAG Laser

This section describes the investigation of the influence of the amorphous layer thickness on the melt and solidification behaviour of Cu implanted α-Si on c-Si on sapphire when annealed with 7.5 ns FWHM pulses from a frequency-doubled Nd:YAG laser. As mentioned in the introduction to this chapter, the thickness of the α-Si layer is of importance whenever it is exceeded by the theoretical thermal penetration depth. The previous two sections have shown that this is nearly always the case for an α-Si thickness of ≃230 nm. It is clear that this situation changes drastically when the α-Si thickness is nearly doubled to 440 nm. The fact that the bulk of the substrate is sapphire does not really matter because the thick α-Si shields the influence of the substrate up to large melt depths. Since the material is irradiated with the same laser pulses as used in section III.2, the melt velocities will be comparable or even higher due to the lower heat-loss to the substrate. A sapphire substrate has the advantage that reflection measurements can be made from the rear, which can give insight into the nucleation of the XCR front from the primary melt. Some data in this section have been published in Materials Research Society Symposium Proceedings **74** , 91-102 (1987).

III.4.1 Time-resolved reflectivity measurements on 440 nm α-Si on 60 nm c-Si on sapphire

Figure III.20 gives the time-resolved reflectivity from the front (TRR-F) obtained at a probe wavelength of 820 nm for the pulsed-laser annealing of 440 nm α-Si on 60 nm c-Si on sapphire with 7.5 ns FWHM pulses from a frequency-doubled Nd:YAG laser. Upon irradiation at 0.24 Jcm^{-2}, figure III.20a, the TRR-F shows a HRP of ≃20 ns duration followed by small oscillations on a time scale about ten times faster than observed for amorphous regrowth, which suggests XCR. This is substantiated by the observed large increase, from 20 to 40 %, of the static reflectivity. The evolution of these oscillations with energy-density can be observed in figure III.20b, for 0.31 Jcm^{-2}.

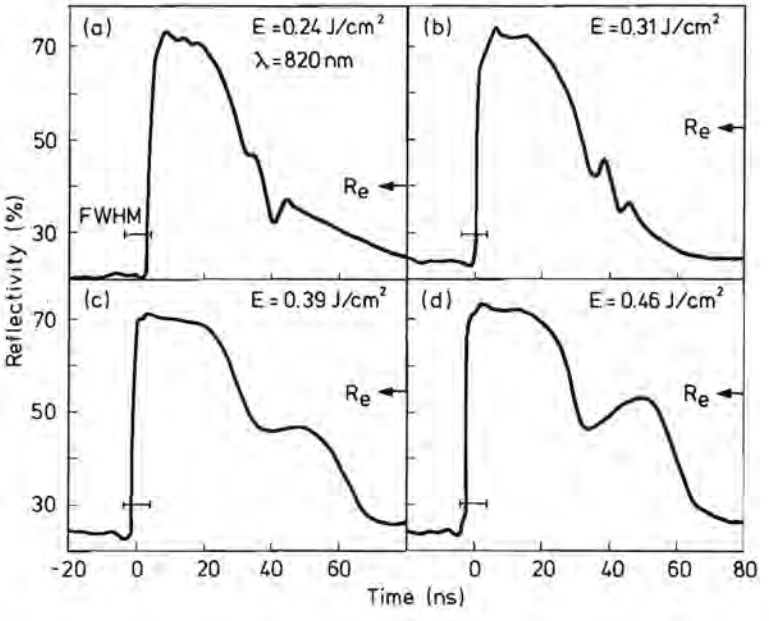

Figure III.20. Time-resolved reflectivity for the front side, at $\lambda = 820$ nm, upon irradiation of 440 nm α-Si on 60 nm c-Si on sapphire with a 7.5 ns FWHM pulse from a frequency-doubled Nd:YAG laser at (a) 0.24, (b) 0.31, (c) 0.39, and (d) 0.46 Jcm^{-2}. The end-reflectivity ($t \rightarrow \infty$) is indicated in the figures by R_e.

The temporal reflectivity signal clearly shows additional extrema in the falling edge of the HRP compared with figure III.20a, indicating that the XCR front has proceeded further. The static reflectivity value has increased from 25 to 52 %. Assuming an effective wavelength of $\frac{820 \text{ nm}}{4.1} \simeq 50$ nm, the XCR front velocity is estimated to be 10 ± 2 m/s. The oscillations in the TRR-F signal could be detected over an energy-density interval of $\simeq 0.15$ Jcm^{-2}. Figures III.20c and 20d show the TRR-F measurements made for 0.39 and 0.46 Jcm^{-2}. The interferences from the explosively propagating solid-liquid front are completely shielded by the high reflectivity phase of the primary melt. What remains is something which looks like the TRR data described in the previous two sections; a HRP followed by a minimum and a maximum on a timescale of tens of

nanoseconds. The static reflectivity changes from 25 to 54 % for both energy-densities, indicating the formation of p-Si.

It is clear from the TRR measurements of figure III.20 that XCR occurs under these conditions. The sapphire substrate makes it possible to measure the TRR from both the front and the rear (TRR-R) simultaneously, which can be used to study the initiation and evolution of the explosively propagating l-Si layer. The results are presented in figure III.21. The reflectivity from the front is obtained at $\lambda = 647$ nm, that from the rear at 820 nm where the absorption is much smaller. In the first instance, the melt and solidification phenomena are described for figure III.21C, at 0.77 Jcm $^{-2}$: The TRR-F shows a familiar behaviour, a HRP with a duration of $\simeq$16 ns, followed by a weak minimum and a small peak. The most important difference from figures III.20c and 20d is the appearance of a low reflectivity plateau (LRP) after the small peak. Measurements at two wavelengths simultaneously, either 488 and 647 nm or 647 and 820 nm, did not reveal a time delay between the extrema. Moreover , the LRP disappears and the small peak becomes more pronounced at longer wavelengths. The TRR-R of figure III.21C contains many interesting details. The signal starts with a fast drop at t$\simeq$-4 ns to about half its original value. An analysis of similar data for lower energy-densities shows that this initial drop is caused by the heating of the α-Si. The surface starts to melt at t$\simeq$-2 ns. The inwards moving melt front is responsible for the interferences in the TRR-F signal between approximately -2 and +12 ns. The number of interferences indicates a melt depth of about 300 nm. It is clear that the resolution of the system was not sufficient to fully resolve the oscillations, which is not surprizing for an average melt velocity exceeding 20 m/s. The liquid-solid front reverses at t = +12 ns; the onset of solidification. The growth velocity from the rear is a little less than 4 m/s. The start of the solidification from the rear coincides roughly with the end of the HRP in the TRR-F signal. These observations indicate that we are dealing with growth of α-Si from both the front and the rear. The slow reflectivity oscillations, caused by the internal solidification front, end at t$\simeq$36 ns and the liquid-solid interface reverses again. It can be inferred from the interferences following t$\simeq$36 ns, that this new melt front covers a distance

of about 200 nm. This brings the total melt depth to approximately 300-100 + 200 = 400 nm, about the thickness of the original α-Si layer. Since the interferences end again at t≃54 ns, the estimated average velocity of the melt front is $\frac{\simeq 200\ \text{nm}}{\simeq 18\ \text{ns}} \simeq 11$ m/s. This value clearly indicates that these last interferences are caused by an explosively propagating l-Si layer. Note that the laser pulse has long since passed during this XCR process. Both TRR signals exhibit a monotonous behaviour beyond t = 52 ns, which can be attributed to the cooling of the material.

The TRR measurements of figures III.21A and 21B, at 0.41 and 0.51 Jcm^{-2}, can also be described with the melting and solidification scheme discussed above. The l-Si thickness increases with energy-density giving rise to more and more interference extrema during the melt phase. The velocity of growth from the rear is ≃1 m/s. This is much less than found at 0.77 Jcm^{-2}, figure III.21C, since the remaining α-Si layer at 0.41 and 0.51 Jcm^{-2} (>300 nm) is significantly larger than the theoretical thermal penetration depth (≃200 nm), which results in a weak temperature gradient. The amorphous regrowth from the rear is again interrupted by XCR. The unmelted α-Si thickness decreases with increasing energy-density resulting in less and less interference extrema during the XCR phase. Note that the total number of extrema in the melt and the XCR phase is constant for figures III.21A to 21C. This observation suggest that the final (secondary) melt depth equals the original α-Si thickness.

Finally, figure III.21D gives the TRR-F and TRR-R signals upon epitaxial growth at 0.91 Jcm^{-2}. The reflectivity from the front only shows a long HRP with no further structure. That of the rear reveals oscillations of both melt-in, which are smeared out considerably now, and epitaxial growth. The difference in solidification velocity, now ≃9 m/s, is clearly visible from the time scale of the oscillations. The encircled part of the TRR-R signal shows the transition between the melting of α-Si and that of c-Si. The reflectivity value remains constant for a short while (<1 ns) after which it resumes its original course but at a slightly weaker angle. This behaviour proves once more that α-Si has a lower melting point and a reduced latent heat with respect to c-Si.

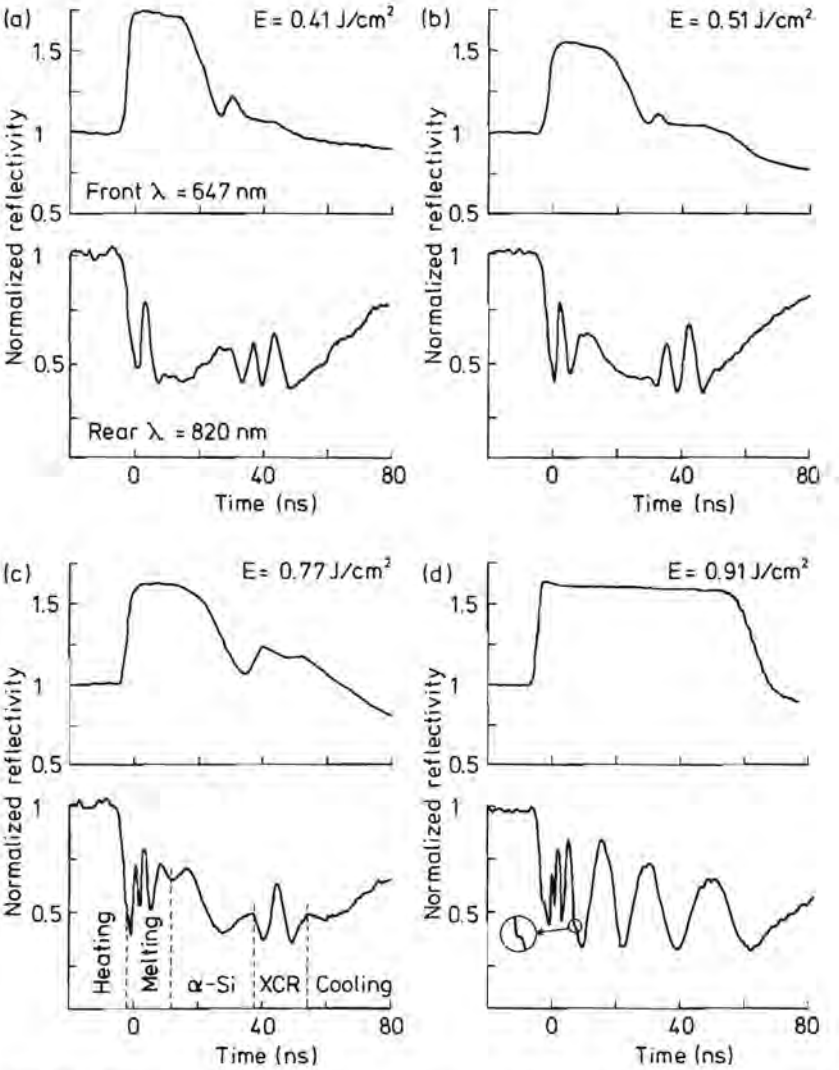

Figure III.21. Time-resolved reflectivity signals, from both the front and the rear, upon irradiation at A) 0.41, B) 0.51, C) 0.77, and D) 0.91 Jcm^{-2} The signals are normalized with respect to their initial value.

III.4.2 Melt depth/velocity simulations

The calculated melt depth for the 440 nm α-Si layer is given in figure III.22. The dependence of the melt depth on energy-density is similar to that shown in figure III.13a with the exception that the influence of the substrate is

shifted to much higher energy-densities. Figure III.22 clearly shows that this influence becomes noticeable at $\simeq 0.35$ Jcm^{-2}, where the curve for the 440 nm layer splits off

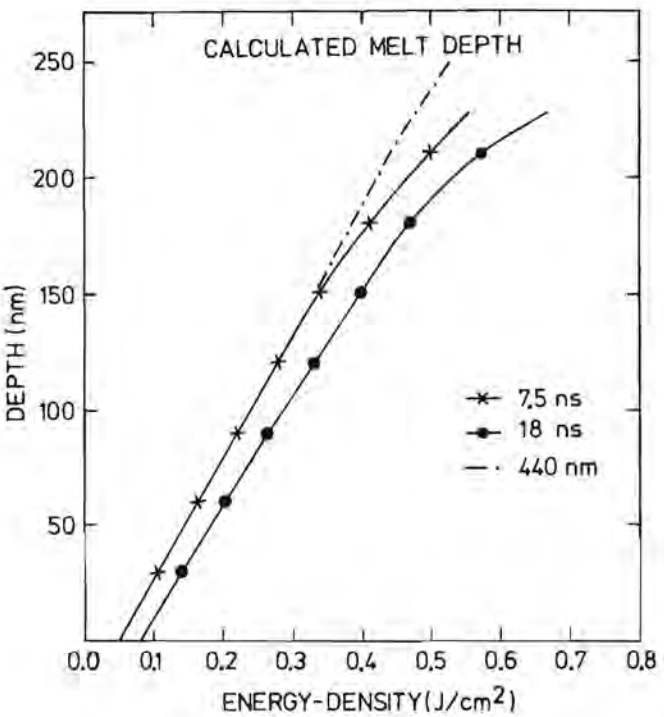

Figure III.22. Melt depth versus energy-density, calculated without superheating and for $dZ = 10$ nm, on irradiation of 440 nm α-Si on 60 nm c-Si on sapphire with 7.5 ns FWHM pulses from a frequency-doubled Nd:YAG laser (dashed line). The simulations for the irradiation of 250 nm α-Si on c-Si with 18 (dots) and 7.5 ns (crosses) pulses from the same laser are added for comparison.

from the one for 250 nm. In fact, the argument about the damaged c-Si layer with its low thermal conductivity also applies to this situation. However, since there was no TEM picture available which showed the thickness of this layer, the simulations were performed with the original thickness. This results, for instance, in a calculated melt depth of 370 nm at 0.80 Jcm^{-2}, while epitaxial

growth occurred experimentally at 0.81 Jcm ^{2}. Fortunately, the effects of this uncertainty in the layer thickness are not severe below 0.53 Jcm^{-2}.

Table VI presents the average melt velocities for these experimental conditions. The velocities are somewhat higher than those in table V.

energy-density	.08 Jcm^{-2}	.17 Jcm ^{2}	.26 Jcm^{-2}	.35 Jcm^{-2}	.53 Jcm^{-2}
average melt velocity	4.3 m/s	8.3 m/s	11.5 m/s	16.3 m/s	19.9 m/s

Table VI. Average melt velocities computed for $\zeta = 0$ upon irradiation of 440 nm α-Si on 60 nm c-Si on sapphire with a 7.5 ns FWHM pulse from a frequency-doubled Nd:YAG laser at 0.17, 0.26, 0.35, 0.44, and 0.53 Jcm^{-2}.

III.5 The irradiation of 225 nm α-Si on c-Si with 32 ns FWHM pulses from a ruby laser

The experimental conditions for this section: 225 nm, Cu implanted α-Si on c-Si irradiated by 32 ns FWHM pulses from a ruby laser, have been shown to favour XCR (Sinke and Saris, 1984). It is clear from the previous three sections that the longer pulse duration and larger optical penetration depth of the ruby laser will primarily influence the melt velocity for this α-Si thickness. Because this could result in the formation of p-Si during melt-in, special care was given to the absolute value of the TRR measurements. We estimated the values to be accurate within ±1 % absolute. Some parts of this work have been published in Applied Physics Letters **49**(18), 1160-1162 (1986).

III.5.1 Time-resolved reflectivity measurements

The TRR signals at various energy-densities just above the threshold for surface melting are given in figure III.23. At 0.16 Jcm^{-2}, figure III.23a, the maximum reflectivity reached is approximately 60 %, which is well below the value for a thick (> 20 nm) l-Si layer at this wavelength, angle, and polarization (73 %). After this peak, oscillations are observed in the reflectivity, which we attribute to XCR. Two minima and one maximum, indicated by consecutive numbers, can be distinguished in figure III.23a. As the energy-density is increased to 0.18 Jcm^{-2}, figure III.23b, the first minimum and maximum (1 and 2) have nearly disappeared and the following minimum and maximum (3 and 4) are now fully developed. At 0.19 Jcm^{-2}, figure III.23c, the first extrema vanish in the tail of the high-reflectivity peak. The oscillations in the TRR could be detected in an energy-density interval of $\simeq$0.05 Jcm^{-2}, considerably less than the 0.15 Jcm^{-2} upon irradiation of 440 nm α-Si with 7.5 ns pulses from a frequency-doubled Nd:YAG laser. Note that these oscillations in the reflectivity do not follow a HRP as was the case in the previous section. The simultaneously recorded TRR signals at 488 nm did not show interferences, in agreement with experiments by Thompson and coworkers (1984). This apparent dependence on the probe wavelength is discussed in section III.5.4.

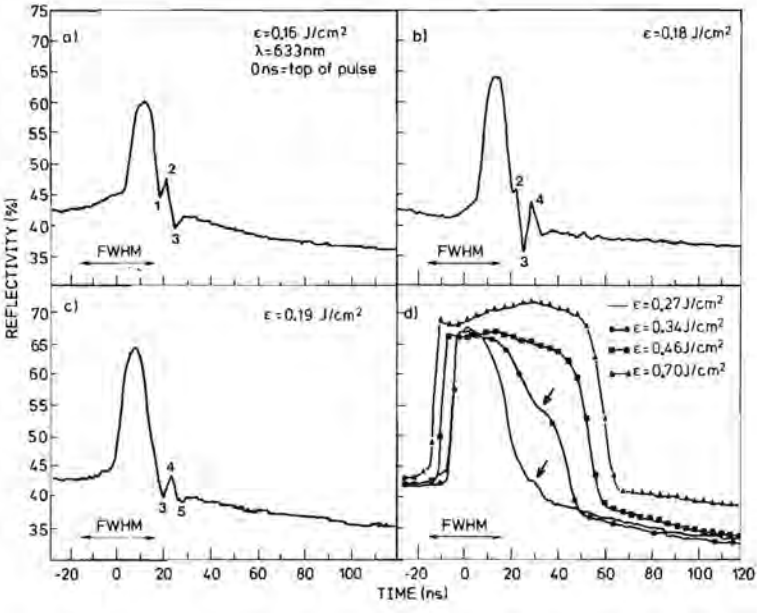

Figure III.23. Time-resolved reflectivity measurements upon irradiation of 225 nm, Cu implanted α-Si with 32 ns FWHM pulses from a ruby laser at various energy-densities.

Figure III.23d gives a compilation of four TRR measurements, at 633 nm, for increasing energy-densities following that of figure III.23c. The thickness and duration of the primary melt are, for these pulses, such that the interference effects are no longer observable. Instead, a small shoulder (indicated by the arrow in the figure) shows up at $t \simeq 30$ ns in the falling edge of the high reflectivity peak for 0.27 Jcm^{-2} (solid line), which appears at higher reflectivity values for increasing energy-densities. At 0.7 Jcm^{-2} (triangles) the shoulder has evolved into a maximum in the HRP. Like the shoulder, it occurs around $t \simeq 30$ ns. This fixed value suggests that these phenomena have some correlation with the timing of the laser pulse. The TRR measurements at 488 nm resemble those of figure III.23d, showing the same behaviour of the reflectivity both with time and energy-density.

III.5.2 Primary and secondary melt depth determined by RBS

After annealing the changes in the Cu profile have been measured by RBS. As found by Sinke and Saris (1984), the originally Gaussian implantation profile develops into a double-peaked structure characteristic for XCR, see section I.2. Part of the Cu is accumulated at the surface of the sample due to segregation during solidification of the primary melt. At the same time it is transported to the interior by the self-propagating l-Si layer. The resulting profile can be used to infer the primary and secondary melt depth. The data for low energy-densities, ranging from 0.14 to 0.27 Jcm^{-2}, are shown in figure III.24. Surface melting starts at 0.14 Jcm^{-2}. For 0.16 to 0.19 Jcm^{-2} the primary melt depth is $\simeq$40 nm. As the energy-density is increased to 0.27 Jcm^{-2}, the primary melt depth increases to $\simeq$65 nm. The penetration of the secondary melt front exhibits a much faster increase with energy-density. From 0.14 to 0.16 Jcm^{-2} it rises from 0 to 135 nm. At 0.27 Jcm^{-2} it almost reaches the c-Si substrate.

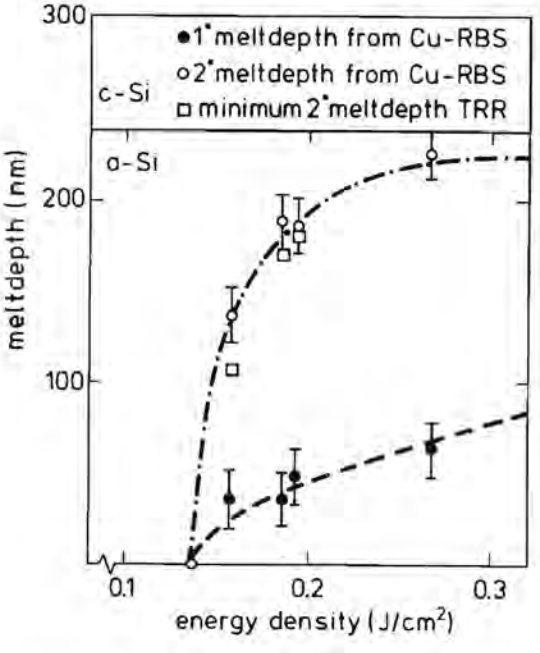

Figure III.24. Primary (solid dots) and secondary (open dots) melt depth as a function of energy-density as measured by RBS, together with estimates for the secondary melt depth from TRR data (open squares).

III.5.3 Comparison between the TRR and the RBS results: evidence for the presence of nuclei in the melt

The comparison of the TRR and RBS data leads to a number of interesting observations. The results in figure III.24 show that the thickness of the primary melt is >20 nm between 0.16 and 0.27 Jcm^{-2}, yet the corresponding TRR data do not show a HRP. Moreover, the maxima in these TRR signals do not reach the 73 %, expected at this wavelength, polarization and angle of incidence. All TRR data are in fact, for at least a part of their high-reflectivity duration, below this value. The reduced reflectivity value can not be explained by the temperature dependence of the optical properties of l-Si. The data of Lampert et al. (1981) suggest an increasing reflectivity value with increasing temperature, an effect with the opposite sign as observed. We believe that the lowering of the reflectivity of the melt is caused by the presence of c-Si nuclei. The existence and growth of such nuclei will both reduce the specular reflectivity of the melt and give rise to scattering. In this way the primary melt can reach thicknesses beyond 20 nm, while its apparent reflectivity stays below 73 %.

The presence of c-Si nuclei in the primary melt is corroborated by the following arguments. We have already discussed that none of the TRR measurements in figure III.23 exhibits a HRP. One would expect a HRP if the primary melt consisted of pure l-Si and was thicker than 20 nm. Since the primary melt depth was greater than 20 nm, this observation implies that the optical properties of the l-Si were not constant in time. Moreover, the falling edges at the end of the high reflectivity phases of the TRR data in figure III.23d, are not as abrupt as one observes for a uniform solid-liquid front moving towards the surface, see e.g. figure III.2d. This is most obvious for the two lowest energy-densities in figure III.23d, where a shoulder is visible in the down going flank of the reflectivity. At 0.70 Jcm^{-2}, this shoulder has developed into a maximum in the reflectivity, which approaches the value of 73 % for pure l-Si at $\lambda = 633$ nm. The shoulder and its evolution into a maximum in the reflectivity is consistent with the idea of c-Si nuclei in the melt. Once there, the growth of the nuclei will be influenced by the absorbed energy from the laser. At low energy-densities, the expansion of the nuclei is only hampered. However, at high

energy-densities the nuclei can be melted. This explains the apparent synchronization with the (end) of the laser pulse, since both the growth velocity reduction and the melting are caused by the absorbed energy from the laser pulse. Note that the reduced high reflectivity value and its decrease in time give a higher effective absorption, which counteracts the decreasing power of the laser pulse. A discussion of the origin of the c-Si nuclei is given in chapter V.

One might argue that the implanted Cu causes such a local melting point depression that the melt initiates in the interior, giving a reduced high reflectivity value (Peercy et al. 1985). Since there are no interferences visible in the high reflectivity phase e.g. at 0.7 Jcm $^{-2}$, figure III.23d, such an internal melt must have been situated within 20 nm below the surface, see section III.5.4. With a melt velocity as low as 1 m/s this would mean that the full reflectivity value of 73 % should be reached within 20 ns from the onset of melting, which is clearly not the case. Another possibility would be that the α-Si is not melted homogeneously, as proposed by Turnbull (1982). In that case, however, it is difficult to explain the behaviour of the reflectivity in time and with energy-density unless the unmelted α-Si ultimately transforms into c-Si without going through the liquid phase.

III.5.4 The XCR front velocity and melt depth/velocity calculations

In order to derive the velocity of XCR from the experiments, we calculated the reflectivity, at 488 and 633 nm, for a 15 nm thick l-Si layer as a function of its position below the surface, see figure III.25. This specific l-Si thickness was chosen as being realistic for XCR (Thompson et al. 1984; Lowndes et al. 1986). The optical constants of the top layer were taken as those of c-Si at the melting temperature of α-Si . The calculated reflectivity at 488 nm clearly shows interferences while these were not detected. Moreover, the reflectivity oscillations observed at 633 nm are much smaller than calculated. This discrepancy may be explained by the following arguments. Firstly, in reality the top layer does not consist of c-Si, as used in the calculations, but of p-Si, which can have a larger absorption. Secondly, the thickness of the top layer is not uniform as can be inferred from TEM studies (Cullis et al. 1980; Narayan and White, 1984;

Bartsch et al. 1986) and any roughness of the liquid-solid interface causes non-specular reflections thus reducing the amplitude of the interferences. Finally, the thickness of the self-propagating l-Si layer will increase and decrease with time, with a rate and maximum value which depend on the experimental conditions such as the temperature gradient and energy-density.

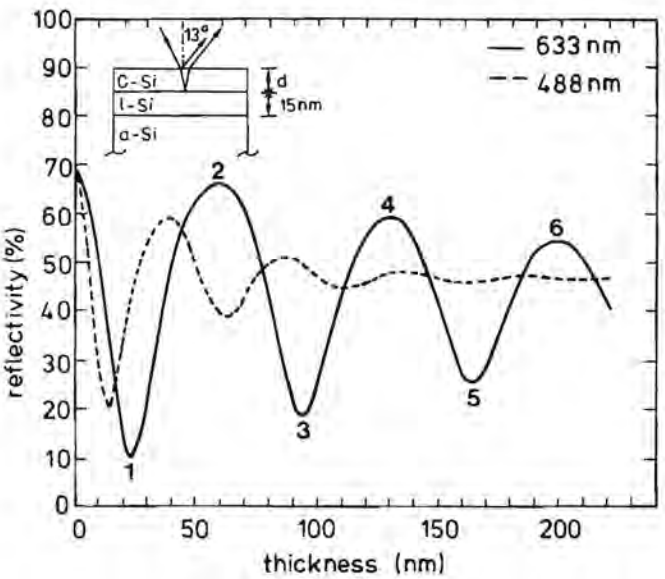

Figure III.25. Calculated reflectivity behaviour at 488 and 633 nm for a 15 nm thick l-Si layer as a function of its position below the surface. The optical constants of the top layer are those of c-Si taken at the melting point of α-Si The extrema at 633 nm are labeled with consecutive numbers, which can be compared with those in figure III.23.

The position of the extrema is, fortunately, not severely influenced by the arguments mentioned above. Therefore we can use the calculated reflectivity data of figure III.25 to obtain an estimate for the velocity of the explosively propagating solid-liquid front. The calculations show that the first minimum in the reflectivity at 633 nm occurs at a l-Si depth of 20 nm, while every additional extremum adds 40 nm to this value ($=\lambda/4$). From the measured time delay between the minima and maxima in the TRR at 0.16 Jcm^{-2} an estimate of 13±3 m/s is inferred for the first two extrema, falling to 6±3 m/s between the

two last ones. The same behaviour is found at 0.18 Jcm^{-2}. In this case the XCR front propagates at a velocity of 13±3 m/s between the first three extrema, again followed by a drop to 6±3 m/s. The number of interference extrema gives an estimate for the secondary melt depth. The result thereof is shown in figure III.24 and is in reasonable agreement with the data from the Cu redistribution, which justifies the presented approach.

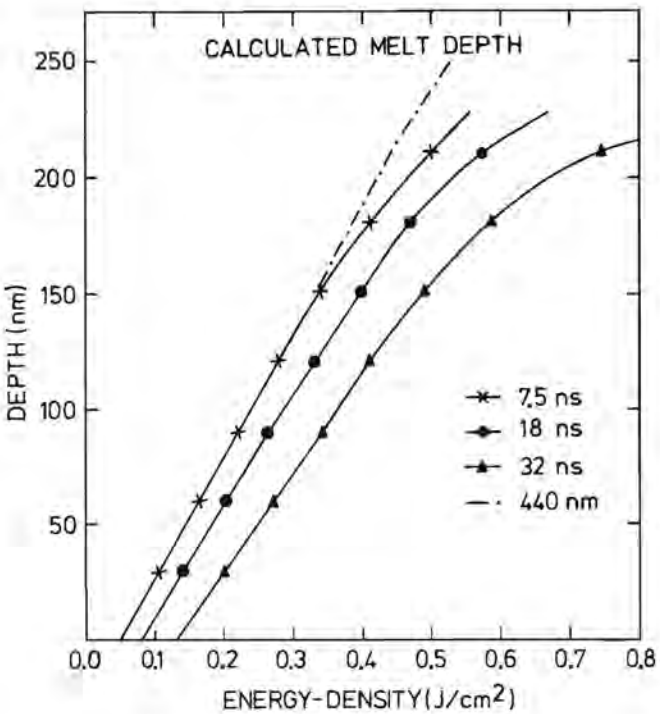

Figure III.26. Melt depth versus energy-density, calculated for dZ = 10 nm and without superheating, upon annealing of 250 nm α-Si on c-Si with 32 ns FWHM ruby laser pulses (triangles). The simulations for the irradiation of the same material with 18 (dots), and 7.5 ns (crosses) pulses from a frequency-doubled Nd:YAG laser are added for comparison.

The calculated melt depth versus energy-density for the annealing of 250 nm α-Si on c-Si with 32 ns FWHM pulses from a ruby laser is given in figure III.26 (triangles). For comparison, the figure also contains the data for annealing with 18 (dots), and 7.5 ns (crosses) pulses from a frequency-doubled

Nd:YAG laser. The threshold energy-density for surface melting is calculated at $\simeq$0.13 Jcm^{-2}. This is higher than for the other two curves because of the longer pulse duration and larger optical penetration depth of the ruby laser. The same arguments apply to the slightly smaller slope of the curve for low energy-densities: 425 (nm/Jcm^{-2}). Epitaxial growth occurs at $\simeq$0.9 Jcm^{-2} according to the simulations. Both thresholds, for surface melting and epitaxial growth, are in good agreement with the experimental values of Sinke and Saris (1984).

energy-density	.17 Jcm^{-2}	.26 Jcm^{-2}	.35 Jcm^{-2}	.53 Jcm^{-2}	.71 Jcm^{-2}
average melt velocity	2.8 m/s	3.1 m/s	4.0 m/s	5.5 m/s	7.2 m/s

Table VII. Average melt velocities calculated for $\zeta = 0$ upon irradiation of 250 nm α-Si on c-Si with a 32 ns FWHM pulse from a ruby laser at 0.17, 0.26, 0.35, 0.53, and 0.71 Jcm^{-2}.

Table VII gives the calculated average melt velocities for these experimental conditions. Their values are all below the ones of tables IV, V and VI. Above $\simeq$0.4 Jcm^{-2}, the difference approaches a factor of 2 respectively 4 with the average melt velocities of table V respectively IV and VI. In first approximation this implies that the superheating of the l-Si with respect to the melting point of α-Si will also be a factor of 2 respectively 4 lower than in the other cases.

References Chapter III

Bartsch, H., Andrä, G., and Glaser, E. (1986); Phys. Stat. Sol. (a) **94**, 773.

Bruines, J.J.P., van Hal, R.P.M., Boots, H.M.J., and Wolter, J. (1986a); *Energy Beam – Solid Interaction and Transient Thermal Processing* edited by V.T. Nguyen and A.G. Cullis (Les editions des physique, Les Ulis Cedex, 1986), page 525.

Cullis, A.G., Chew, N.G., Webber, H.C., and Smith D.J. (1984); J. Cryst. Growth **68**, 624.

Campisano, S.U., Jacobson, D.C., Poate, J.M., Cullis, A.G., and Chew, N.G. (1985); Appl. Phys. Lett. **46**, 846.

Cullis, A.G., Webber, H.C., and Chew, N.G. (1980); Appl. Phys. Lett. **36** , 547.

Cullis, A.G., Webber, H.C., and Chew, N.G. (1986); Appl. Phys. Lett. **40** , 998.

Devaud, G., Turnbull, D. (1985); Appl. Phys. Lett. **46**, 844.

Lampert, M.O., Koebel, J.M., and Siffert, P. (1981); J. Appl. Phys. **52** , 4975.

Lowndes, D.H., Jellison, G.E., Pennycook, S.J., Withrow, S.P., and Mashburn, D.N. (1986); Appl. Phys. Lett. **48**, 1389.

Narayan, J. and White, C.W. (1984); Appl. Phys. Lett. **44**, 35.

Peercy, P.S., Thompson, M.O., and Tsao, J.Y. (1985); Appl. Phys. Lett. **47**, 244.

Roorda, S., Saito, S., and Sinke, W.C. (1988); submitted to Phys. Rev. Lett.

Roth, J.A., and Olson, G.L. (1987); Mat. Res. Soc. Symp. Proc. **74** , 319.

Thompson, M.O., Galvin, G.J., Mayer, J.W., Peercy, P.S., Poate, J.M., Jacobson, D.C., Cullis, A.G., and Chew, N.G. (1984); Phys. Rev. Lett. **52** , 2360.

Thompson, M.O., Mayer, J.W., Cullis, A.G., Webber, H.C., Chew, N.G., Poate, J.M., and Jacobson, D.C. (1983); Phys. Rev. Lett. **50**, 896.

Tsao, J.Y. and Peercy, P.S. (1987); Phys. Rev. Lett. **58**, 2782.

Turnbull, D. (1982); Mat. Res. Soc. Symp. Proc. 7, 103.

Sinke, W and Saris, F.W. (1984); Phys. Rev. Lett. **53**, 2121. The pulse length mentioned in this text (20 ns) is incorrect. The correct value is 32 ns.

IV. HEAT-FLOW MODEL OF MELTING AND SOLIDIFICATION

IV.1. Introduction

Computer models based on heat-flow calculations have become an important aid for pulsed-laser annealing experiments. The main objective for developing these models was the determination of the threshold energy-density for melting and epitaxial growth. However, soon after their introduction, they were also used to verify theoretical assumptions concerning melting, solidification, diffusion and segregation. Computer simulations played a crucial role in the controversy between thermal versus plasma assisted melting (Wang et al. 1978; Baeri et al. 1979, van Vechten et al. 1979a, 1979b; Wood and Giles, 1981). Recently, heat-flow calculations dominated the discussion about superheating/undercooling, and were of great help in the determination of the thermophysical properties of α-Si (Lowndes et al. 1984; Thompson et al. 1984, 1985). Finally, computer simulations still are of importance for unravelling the basic processes behind explosive crystallization and amorphous regrowth (Wood et al. 1984; Wood and Geist, 1986a, 1986b; Tsao and Peercy, 1987) and are indispensable for the comparison of experiments performed under different conditions such as other wavelengths, pulse durations, α-Si thicknesses, and substrates.

This chapter is divided into three sections. The first one describes the basic theory of heat-flow calculations, most of which can be found in articles by Baeri et al. (1979) and Wood and Giles (1981). A more elaborate discussion of all physical mechanisms involved in pulsed-laser irradiation has been given by van Driel et al. (1982) and Lietoila and Gibbons (1982a, 1982b). In contrast to the standard theory which can be found in the articles mentioned above, our model also incorporates superheating and undercooling. This is not new in itself (Thompson et al. 1985), but has not been described previously. The second section deals with the way in which we simulated amorphous regrowth. Until now this phenomenon has never been modelled. The third and last section of this

chapter contains three different approaches to simulate XCR. Two of them are unique implementations of nucleation theory into a heat-flow computer model, the third one is based on ad-hoc assumptions. The latter having been written by Wood and Geist (1986a, 1986b).

IV.2. Fundamental Concepts of Heat-Flow Calculations

IV.2.1 The mathematical problem

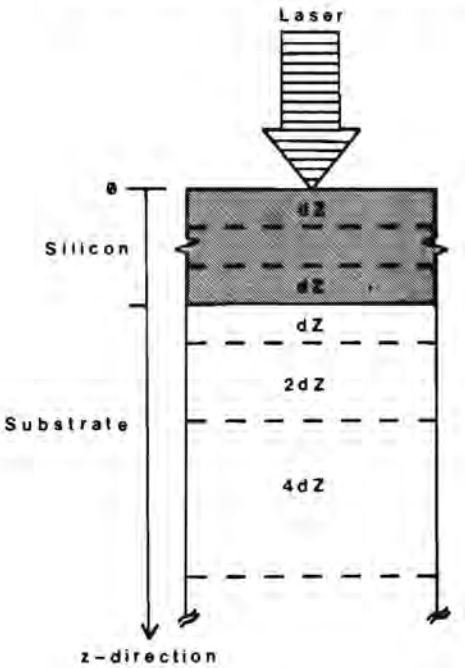

Figure IV.1. Drawing of the one-dimensional geometry used in the calculations.

The model described in this section is based on the following assumptions. First of all, we assume the problem to be one-dimensional. This is justified when the heat-flow directed towards the substrate is much greater than that directed towards the absorbing film or in a formula:

$$\pi\rho^2\kappa_s \gg 2\pi\rho h\kappa_f \;\rightarrow\; \rho\kappa_s \gg h\kappa_f \tag{30}$$

where κ_s and κ_f are the thermal conductivities of the substrate and absorbing film, h the thickness of the absorbing film and ρ the radius of the irradiated spot. Under normal annealing conditions this is easily satisfied since the thermal conductivities do not differ much while the radius of the annealing spot is usually about four orders of magnitude larger than the thickness of the film. For

optical recording, however, the submicron spot size often tips the scale to a combined substrate and film dominated heat flow thus requiring a two dimensional approach. Figure IV.1 shows the final one-dimensional geometry used in the calculations. The second major assumption made is that the absorbed laser light is "instantly" converted to heat. It has been shown by Shank et al. (1983a, 1983b) that this so called thermal model can be used down to the picosecond regime. For pulses in the femtosecond region the dense electron-hole plasma created by the absorbed photons starts to play a role. The third major assumption is that free carrier absorption, i.e. absorption by the free electrons and holes, is negligible. Lietoila and Gibbons (1983b) have calculated that this is indeed the case for $\lambda = 532$ nm. In fact the free carrier absorption can be ignored for all wavelengths with photon energies reasonably above the band gap of Si, i.e. $\lambda < \simeq 0.9$ μm for c-Si and $\lambda < \simeq 1.4$ μm for α-Si. Last of all, it has been assumed that α-Si exhibits a well-defined static melting point and latent heat.

Based on the assumptions discussed above, the differential equation for the heat flow can be written as:

$$C_p(z,T(z,t)) \frac{\partial T(z,t)}{\partial t} - \frac{\partial}{\partial z} \left\{ \kappa(z,T(z,t)) \frac{\partial T(z,t)}{\partial z} \right\} = S(z,t,T(z,t)) \qquad (31)$$

T(z,t) is the temperature, t represents time, z the depth with the surface as origin, S(z,t,T(z,t)) the so called source function, and κ(z,T(z,t)) respectively C_p(z,T(z,t)) the thermal conductivity and specific heat. The source function S(z,t,T(z,t)) is the driving force for the heat-flow, in our case the absorbed laser light:

$$S(z,t,T(z,t)) = \frac{\partial I(z,t)}{\partial z} = \alpha(z,T(z,t))\, I(z,t)$$

$$= \alpha(z,T(z,t))\, \{1 - R(t)\}\, I_0(t)\, \exp\{ - \int_0^z \alpha(\xi,T(\xi,t))\, d\xi \} \qquad (32)$$

with α(z,T(z,t)) the absorptive power of the medium, I(z,t) respectively I_0(t) the instantaneous intensity in the medium and impinging on the medium, and R(t) the reflection coefficient of the medium.

IV.2.2 Analytical approximations

Carslaw and Jaeger (1959) have shown that an analytical solution for equations (31 and 32) can be given under certain constraints: no temperature or spatial dependence of the constants, no phase changes involved, constant laser power, uniform initial temperature T_0, and an infinite sample thickness. In this case the solution can be written as:

$$T(z,t) = T_0 + \frac{(1-R)I_0}{\kappa}\left[2\sqrt{Dt}\ ierfc\left\{\frac{z}{2\sqrt{Dt}}\right\} - \frac{1}{\alpha}\,e^{-\alpha z}\right.$$
$$+ \frac{1}{2\alpha}\,e^{\{\alpha^2 Dt-\alpha z\}} \times erfc\left\{\alpha\sqrt{Dt} - \frac{z}{2\sqrt{Dt}}\right\} \qquad (33)$$
$$\left. + \frac{1}{2\alpha}\,e^{\{\alpha^2 Dt+\alpha z\}} \times erfc\left\{\alpha\sqrt{Dt} + \frac{z}{2\sqrt{Dt}}\right\}\right]$$

where $D \equiv \frac{\kappa}{C_p}$ is the thermal diffusivity and erfc$\{\xi\}$ respectively ierfc$\{\xi\}$ are the normal and the integrated form of the so called complementary error function (Abramowitz and Stegun, 1964):

$$erf\{\xi\} = \frac{2}{\sqrt{\pi}}\int_0^{\xi} e^{-x^2}dx \qquad erfc\{\xi\} = 1 - erf\{\xi\}$$

$$ierfc\{\xi\} = \int_{\xi}^{\infty}[1 - erf\{x\}]dx$$

Expression 33, which is not very transparent, can be further approximated in two cases. First the situation in which the absorption length $1/\alpha$ is much smaller than the thermal diffusion length $\sqrt{Dt}$. This condition is often fulfilled when α-Si is irradiated with pulses of long duration.

$$\alpha^{-1} \ll \sqrt{Dt} \rightarrow T(z,t) = T_0 + 2I_0(1-R)\frac{\sqrt{Dt}}{\kappa}\ ierfc\left\{\frac{z}{2\sqrt{Dt}}\right\} \qquad (34)$$

For z=0 this equation reduces to:

$$T(0,t) = T_0 + \frac{2I_0(1-R)}{\kappa}\sqrt{\frac{Dt}{\pi}} \qquad (35)$$

This result can be used to determine the threshold energy-density, E_0, for which melting occurs at the surface, i.e. $T(0,t) = T_m$, for laser pulses with a duration of τ seconds. Using that $I_0 = \frac{E_0}{\tau}$ for these conditions, eq. 35 can be rewritten as:

$$T_m - T_0 = \frac{2(E_0/\tau)(1-R)}{\kappa}\sqrt{\frac{D\tau}{\pi}} \quad \rightarrow \quad E_0 = \frac{\kappa(T_m - T_0)}{2(1-R)\sqrt{D/\pi}}\sqrt{\tau} \qquad (36)$$

E_0 depends on the square root of the pulse duration and is completely independent of the absorption coefficient.

The other simplified expression can be obtained when the absorption length is much larger than the thermal penetration depth, a situation which is encountered in the irradiation of c-Si with short laser pulses:

$$\alpha^{-1} \gg \sqrt{Dt} \quad \rightarrow \quad T(z,t) = T_0 + \frac{\alpha I_0(1-R)}{C_p}\, t\, e^{-\alpha z} \qquad (37)$$

Also this expression can be further reduced for $z = 0$:

$$T(0,t) = T_0 + \frac{\alpha I_0(1-R)}{C_p}\, t \qquad (38)$$

Applying the same procedure on eq. 38 as used to derive eq. 36 from eq. 35, we obtain:

$$T_m - T_0 = \frac{\alpha(E_0/\tau)(1-R)}{C_p}\tau \quad \rightarrow \quad E_0 = \frac{C_p(T_m - T_0)}{(1-R)\alpha} \qquad (39)$$

In this case, the threshold energy-density for surface melting is proportional to the inverse of the absorption coefficient and completely independent of the pulse duration. The formulas given in this section will be used to test the computer simulations based on a description of the heat-flow problem in terms of a finite-difference equation as given in the next section.

IV.2.3 Finite-difference description of the heat-flow problem

Unfortunately, the optical and thermophysical properties of Si are far from constant as was discussed in section I.3. Moreover, one of the main objectives in developing computer models was to calculate the melt depth, and thus the model must cope with phase transitions. Finally, no pulsed-laser has a power which is constant in time. It is clear from this discussion that eqs. 31 and 32 must be transformed into a finite-difference form and solved numerically. Both time and depth are divided into discrete steps n×dt respectively i×dZ. The first term of eq. 31, containing the derivative of the temperature versus time, transforms into:

$$C_p(z,T(z,t))\,\frac{\partial T(z,t)}{\partial t} \quad \rightarrow \quad C_p(i,T(i,n))\,\frac{T(i,n+1)-T(i,n)}{dt}$$

The term containing the second derivative of the temperature versus depth is now written as the difference of the heat-flow between slab i-1 and i, the left hand side, and that between i + 1 and i, the right hand side:

$$\frac{\partial}{\partial z}\left\{\kappa(z,T(z,t))\,\frac{\partial T(z,t)}{\partial z}\right\} \quad \rightarrow \quad \kappa(i,i-1)\,\frac{T(i-1,n)-T(i,n)}{dZ^2} + \kappa(i,i+1)\,\frac{T(i+1,n)-T(i,n)}{dZ^2}$$

Where $\kappa(i,j) = \dfrac{2\,\kappa(i,n)\,\kappa(j,n)}{\kappa(i,n)+\kappa(j,n)}$, the effective heat conductivity coefficient between two neighbouring slabs. Finally, the source function described by eq. 32 transforms into:

$$S(z,t,T(z,t)) = \frac{\partial I(z,t)}{\partial z} \quad \rightarrow \quad \frac{I(i,n)}{dZ}\left\{1-e^{-\alpha(i,T(i,n))\,dZ}\right\}$$

The combination of the last three expressions gives the final finite-difference equation for the heat-flow problem:

$$C_p(i,T(i,n))\,\frac{T(i,n+1)-T(i,n)}{dt} - \frac{1}{dZ}\left[\kappa(i,i-1)\,\frac{T(i-1,n)-T(i,n)}{dZ}\right.$$

$$- \kappa(i+1,i)\,\frac{T(i,n) - T(i+1,n)}{dZ}\Bigg] \quad (40)$$

$$= \frac{I(i,n)}{dZ}\left\{1 - e^{-\alpha(i,T(i,n))\,dZ}\right\}$$

When a slab dZ consists of more than one phase, all its properties are averaged with respect to the fractions of the phases. With the transformation of the differential equation 31 into the finite-difference form of equation 40, we are now able to perform a completely realistic calculation including depth and temperature dependent parameters. The incorporation of phase changes will be discussed in the next section.

IV.2.4 Boundary conditions, stability and phase changes

The heat-flow problem has two boundary conditions, one related to the heat-flow out of the surface and one associated with the substrate temperature for $z \to \infty$. Next it will be shown that there is virtually no loss of heat from the surface for pulses in the nanosecond regime. In principle there are two loss mechanisms: radiation and convection. The first one is governed by the Stefan-Boltzmann law. Using the maximal value for the emisivity (1) to calculate the loss of heat by black-body radiation during one microsecond for a surface at the melting temperature of c-Si we get 0.2 Jm^{-2}. Compared to the threshold energy-density of 2000 Jm^{-2} for melting c-Si with a 7.5 ns FWHM pulse from a frequency-doubled Nd:YAG laser this is completely negligible. The convection of heat from the surface is even less important. With an average heat transfer coefficient of 15 $Wm^{-2}K^{-1}$ for a surface perpendicular to the ground plane (Smith and Stammers, 1973), our standard annealing geometry, the heat convection gives a loss of only 0.02 Jm^{-2} under the same conditions. The fact that there is no heat-flow through the surface implies that the temperature gradient $\frac{\partial T}{\partial z}$ must be zero there, which is accounted for in the simulations by adding a dummy slab with the same temperature as the surface.

The other boundary condition $T(\infty, t) = T_0$ has its implications for the total number of slabs for which the temperature must be calculated. In our

model the absorbing film is divided into slabs of equal thickness dZ. The substrate has only one slab of thickness dZ at the beginning of the calculation. Every time that the temperature of the last slab rises above T_0, an extra slab is added with doubled thickness of the previous one (dZ, 2dZ, 4dZ, ..., see figure IV.1). This procedure minimizes the total computing time while maintaining a good simulation of the temperature profile in the substrate. The heat-flow in the substrate is only by diffusion, which gives a decreasing temperature gradient with depth. This makes it possible to use larger slabs at greater depth without much loss of accuracy.

To obtain the right solution, dZ and dt must at least fulfill the stability criterion for parabolic partial differential equations (Arden and Astill, 1970):

$$\frac{\kappa\, dt}{C_p\, dZ^2} < \frac{1}{2} \quad \rightarrow \quad dt < \frac{dZ^2}{2\,D} \tag{41}$$

This expression can be deduced if one bears in mind that the increase in temperature during dt is not allowed to exceed the original temperature difference between neighbouring slabs. The lowest diffusivity value $D = 8.8 \times 10^{-5} m^2 s^{-1}$, reached for c-Si at room temperature, results in a dt of <0.57 ps for the frequently used slab size of 10 nm. The choice of the slab size depends on the type of calculation. Simulations involving large gradients and temperature or heat-flow sensitive effects require small slab sizes. The total calculation time scales with dZ^{-3}, since the number of time steps is proportional to dZ^{-2} and the number of slabs to dZ^{-1}. This strong dependence on the slab size severely limits the possibility of variation due to total run time restrictions. unfortunately not possible to use a more complex discretization scheme. The advantage of higher order methods is that they use larger time steps at the cost of computational effort. However, the pulse power is usually so large and changes so rapidly that large time steps can not be afforded. Moreover, this extreme driving force can cause the melt front to move at velocities up to hundreds of meters per second signifying that a slab of 10 nm is melted in only 100 ps. Unless stated otherwise, all calculations involving Si were done with dt = 0.5 ps for dZ = 10 nm.

In general there are two ways to deal with phase changes in the model. The first one is by using a continuous transition in which the effect of the latent heat L_h is incorporated in the specific heat. This is done by adding a Gaussian term which has its peak at the melting point and the latent heat as its integrated value. This approach has the disadvantage that the steps in temperature, for given dt, can be so large that the latent heat is not correctly accounted for. To avoid this, the phase change has to be made discontinuous. Without the dynamical velocity-superheating/undercooling effect this is rather easy since there is only one melting temperature. As soon as the temperature of a given slab reaches T_m, the in- or outgoing flow of energy, dQ, in a time step dt is used to melt or solidify:

$$dQ = -\partial DZ\, L_h \rightarrow \partial DZ = \frac{-dQ}{L_h} \tag{42}$$

where ∂DZ represents the change in the amount of solid material in the slab. The temperature is again allowed to change when the slab is completely melted respectively solidified. If the velocity- superheating/undercooling relation is built in, the melt temperature becomes dynamical T_m^{dyn}, and dQ is used both to melt/solidify and to heat/cool the slab:

$$dQ = -\partial DZ\, L_h + C_p\, (T_m^{dyn} - T)\, dZ \tag{43a}$$

in which $C_p\,(T_m^{dyn} - T)\,dZ$ accounts for the energy needed to change the temperature of the slab from T to T_m^{dyn}. The dynamical melt temperature can be expressed in terms of the melt velocity V, see eq. 16 in section 1.4 with $T_i = T_m^{dyn}$.

$$T_m^{dyn} = T_m + \zeta V \tag{43b}$$

This result is again used in equation 43a leading to:

$$\partial DZ = \frac{C_p\, (T_m - T + \zeta V)\, dZ - dQ}{L_h} \tag{43c}$$

This is the input for the new amount of solid material in the slab, DZ, phase change velocity, and melt temperature:

$$DZ = DZ_{old} + \partial DZ \tag{44a}$$

$$V_{new} = -\frac{\partial DZ}{dt} \tag{44b}$$

$$T_m^{dyn} = T_m + \zeta V_{new} \tag{44c}$$

The constants in these equations still depend on the phase of the Si and possibly even on whether melting or solidification occurs (see section I.4). The model assumes that crystalline growth occurs as soon as l-Si is in contact with c-Si; it is not necessary to have an interfacial temperature above 1685 K to obtain epitaxial growth.

There is yet another change of phase involved. As already mentioned in chapter I, when Si is forced to solidify with a velocity exceeding 15 m/s it can grow only in the amorphous phase. This is not incorporated in the model but can easily be implemented by means of a statement which changes the latent heat and melting temperature of all non-solid slabs in that case. It is necessary to do this for all non-solid slabs and not just for the one which is solidifying because c-Si can not grow on top of α-Si. The special cases of XCR and amorphous regrowth from both the interior and the surface are described in two separate sections of this chapter.

IV.2.5 The source function

The source function is the basis of the calculations. It contains three elements: the reflectivity, temporal pulse shape, and absorption. The reflectivity shows a rather abrupt increase from ≃45 % to ≃75 % upon melting, for wavelengths in the visible region. The high reflectivity value of l-Si is reached for a melt depth exceeding approximately two times its optical penetration depth, ≃20 nm. A linear interpolation between the reflectivity values of the solid and the liquid, with the melt depth as parameter, is used in the model. In general it is very difficult to do heat-flow calculations on interference structures such as silicon on sapphire. The correct way would be to do a simultaneous optical matrix calculation to obtain the temporal reflectivity. This procedure is, however, seldom found in the literature because it costs a lot of computing time. Instead

the reflectivity value of the solid is adapted to give the measured threshold energy-density for melting. Since the high absorptivity of l-Si damps interferences, it is thus possible to calculate the melt depth as a function of energy-density of these structures.

The temporal shape of the power of most pulsed-lasers is approximately Gaussian. This also leads to a Gaussian intensity at the surface:

$$P_0(t) = \frac{E_{tot}}{\sqrt{2\pi}\,\sigma}\, e^{-(t-\mu)^2/(2\sigma^2)} \tag{45}$$

The pulse duration is expressed in terms of the full width at half maximum value τ_p. This value is converted to obtain σ, which governs the width of the Gaussian $\sigma = \tau_p/\sqrt{8\ln(2)}$. The integral versus time of eq.45 gives the energy-density, represented by E_{tot}. The position in time of the peak value is given by μ. In the calculations we have chosen $\mu = 2.25\ \sigma$ and a total pulse duration of $4.5\ \sigma$. To correct for the fact that the Gaussian is not integrated from $-\infty$ to $+\infty$ but from $-2.25\ \sigma$ to $+2.25\ \sigma$, the inputted energy-density is multiplied by 1.025 in the program.

Equation 40 shows that the absorbed energy in slab i during time step n is given by $I(i,n)\,\{1 - e^{-\alpha(i,T(i,n))\,dZ}\}dt$. One could choose $dZ \ll \alpha_{l\text{-}Si}^{-1} \simeq 10$ nm so that the exponential factor can be linearized into $\alpha(i,T(i,n))\,I(i,n)\,dZ\,dt$. The resulting slab size is, however, excessively smaller than that needed on the basis of heat diffusion. Moreover, it would lead to unrealistic computing times. The first real slab starts with the full intensity, corrected for the surface reflectivity. The absorption of every following slab is evaluated with the end intensity of its predecessor. If necessary a non-coherent reflection from the substrate can be taken into account. This double pass absorption scheme gives another, more sophisticated, possibility to deal with interference structures. The method enables one to start with a high effective surface reflectivity, which decreases with temperature to a lower value. This is caused by screening of the reflection from the substrate due to the high absorption between the surface and the substrate at high temperatures. Both methods, the adaption of the surface reflectivity and the double pass absorption, can only be used to calculate global parameters,

such as the maximum melt depth or the threshold energy-density for epitaxial growth, and not to gain insight into local features as the temperature profile or melt velocity.

IV.3 The Testing of the Model

IV.3.1 Heat diffusion

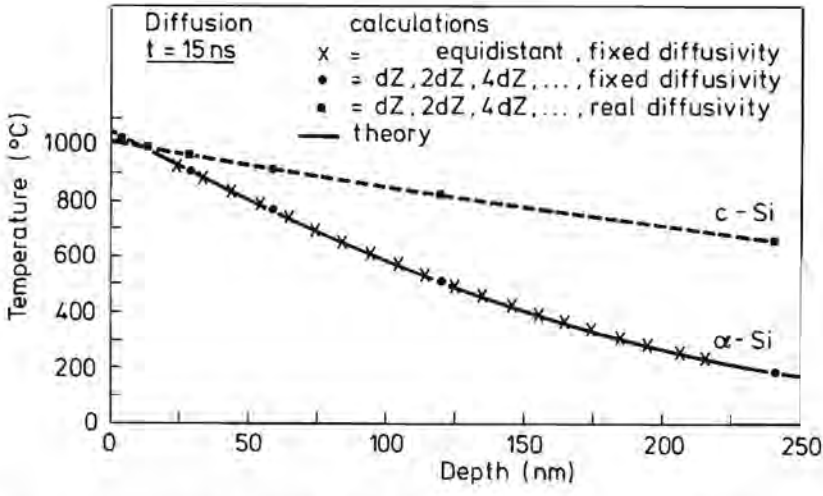

Figure IV.2. Comparison between the simulations for dZ = 10 nm and the theory for pure heat diffusion from a surface held at 1000 °C for 15 ns. The thermal diffusivity was either set at 10^{-6} $m^2 s^{-1}$, characteristic for α-Si (x, •), or that of c-Si, $\simeq 1.5 \times 10^{-4}$ $m^2 s^{-1} e^{-T/405\,K}$ (squares).

The correctness of the heat diffusion algorithm was tested separately for an equidistant subdivision and for one having dZ, 2dZ, 4dZ,... slabsizes. In both cases the impinging laser intensity was zero and the temperature of the first slab fixed at 1000 °C. The thermal diffusivity was taken as either 10^{-6} $m^2 s^{-1}$, characteristic for α-Si, or 1.5×10^{-4} $m^2 s^{-1} e^{-T/405\,K}$, that of c-Si. For pure heat diffusion, the the temperature profile in the medium is given by:

$$T(z,t) = T_0 - \Delta T \; erfc\left\{ \frac{z}{2\sqrt{Dt}} \right\} \qquad (46a)$$

where ΔT is the temperature difference between the heat source and the medium at $z \to \infty$ and D must be constant. To a first approximation this can be written as:

$$T(z,t) = T_0 - \frac{z\,\Delta T}{\sqrt{\pi D t}} \qquad (46b)$$

Beyond this simplified expression one has to use tabels, e.g. by Abramowitz and Stegun (1964). When comparing the simulated result with expressions 46a and 46b, one has to take into account that the algorithm calculates the temperature averaged over the slabsize. As can be seen in figure IV.2, the outcome of the heat diffusion simulation for the top layer is in excellent agreement with expressions 46a and 46b. The same procedure was followed to test the heat diffusion in the substrate. Figure IV.2 shows that the increasing slabsize still gives the correct representation of the temperature profile. To illustrate the effect of the temperature dependence of the thermal properties, a simulation for the real κ and C_p of c-Si is added in figure IV.2. It is clear from this comparison that, under identical conditions, the temperature gradient in c-Si is much smaller than that in α-Si

IV.3.2 Absorption

The implementation of the optical absorption in the model can be tested by a comparison with the analytical expression for that case, given in equation 37. In order to obtain the pure optical absorption regime, without any diffusion, the thermal conductivity coefficient κ was set to zero. The incident power (1-R) I_0 was taken as 1.87×10^{10} Wm^{-2}, giving an equivalent energy-density of 0.05 Jcm^{-2} after 15 ns. C_p and α had the values of 2×10^6 $Jm^{-3}K^{-1}$ and 10^7 m^{-1} respectively. The chosen parameters give a calculated surface temperature of 1234 °C at t = 13 ns. Both the analytical and the calculated temperature profile are given in figure IV.3.

IV.3.3 Melting and solidification

Since phase changes could not be incorporated into the analytical expressions of section IV.2.2, the implementation of melting and solidification can not compared with them. The only way to prove the correctness of the model in this respect is to compare the calculations with the experiments, which is re-

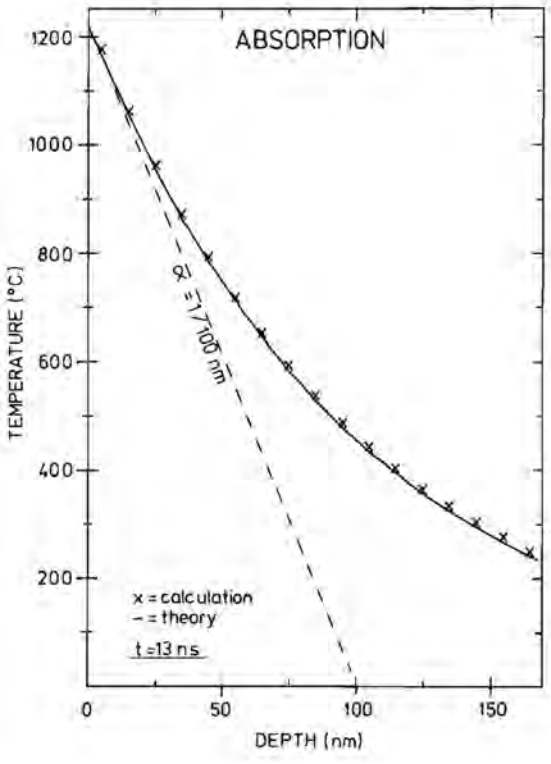

Figure IV.3. Test of the implementation of pure optical absorption in the model for $\alpha = 10^7\ m^{-1}$, R = 0.44, t = 13 ns, $\kappa = 0\ Wm^{-2}K^{-1}$, $I_0 = 3.33 \times 10^{10}\ Wm^{-2}$, and dZ = 10 nm.

served for chapter V. However, the conservation of energy during the melting process can be tested rather easily. In that case the initial temperature is set to 1459 K, just one degree below the melting point of α-Si, and superheating is neglected ($\zeta = 0$). This procedure ensures that all absorbed energy is used for melting and not for heating. Several calculations have been performed in this way, each with a different energy-density. The calculated melt depths were all in excellent agreement with the absorbed energy.

Although superheating and undercooling can also not be analytically verified, it is interesting to look at the implications of e.g. superheating on the melt velocity and melt depth.

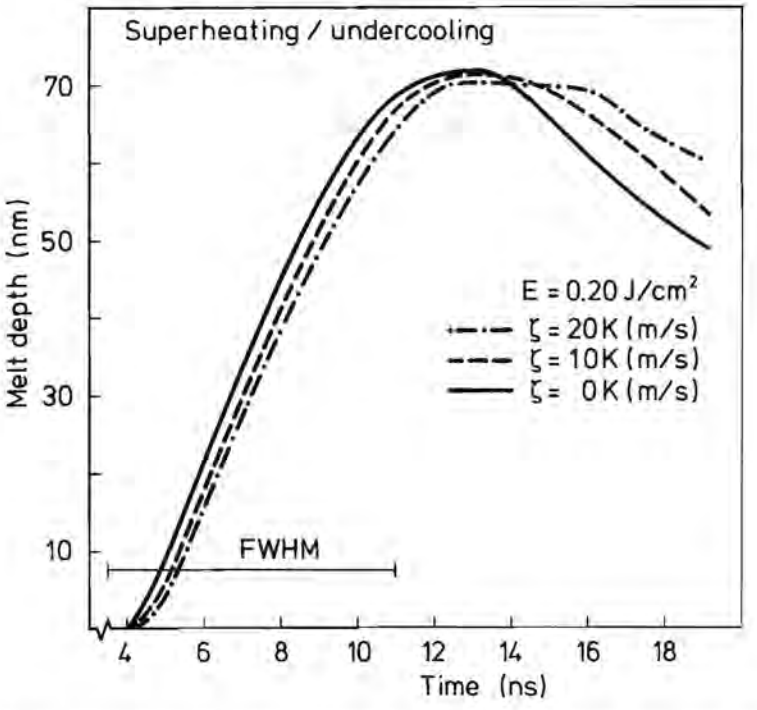

Figure IV.4. Example of the influence of superheating on the simulated temporal melt depth for irradiation of 220 nm α-Si on c-Si with a 7.5 FWHM & 0.2 Jcm^{-2} pulse from a frequency-doubled Nd:YAG laser, dZ = 10 nm.

Figure IV.4 shows the melt depth versus time upon irradiation by a 7.5 ns FWHM & 0.2 Jcm^{-2} pulse from a frequency-doubled Nd:YAG laser of a 220 nm thick α-Si on c-Si layer, for different values of ζ. The superheating has only a small effect on the melt velocity and melt depth. However, the time at which the maximum melt depth is reached shifts to longer values with increasing ζ. This is caused by the fact that the release of heat from the superheated l-Si is by diffusion, a slow process compared to the input of energy by the laser pulse. The effect of undercooling on the phenomenon of amorphous regrowth from both the interior and the surface is discussed in section IV.8.1 and chapter V.

IV.4 The Modeling of Amorphous Regrowth from the Surface and Explosive Crystallization

IV.4.1 Amorphous regrowth from the surface

The physical principles of amorphous regrowth from the surface are not well understood. The now generally accepted explanation for this phenomenon was given by Cullis et al. (1982, 1984). They proposed that its cause is the possibility of "nucleation" of α-Si at the free surface in the presence of l-Si, highly undercooled with respect to the melting point of α-Si. This severe undercooling results from the growth of α-Si from the interior in combination with a melting point depression due to segregation of implanted impurities at the solidification front. Both the "nucleation" temperature and the value of the velocity-undercooling relationship are unknown for α-Si. These two parameters can in principle be obtained from a comparison between simulations and measurements. The "nucleation" temperature determines the moment in time at which growth from the surface starts. The value of ζ, and its dependence on impurity segregation, can be deduced from the temporal evolution of the regrowth velocity. It is very unlikely that growth of α-Si can occur from the surface at a temperature above its melting point.

The framework described above can be realized in a computer model by introducing two separate dynamical melt temperatures and solidification velocities, one for the interior and one for the surface. Solidification from the surface is allowed to start as soon as the temperature of the first slab decreases below its own melting point. The value of the velocity-undercooling parameter ζ plays an important role in these calculations. As already mentioned, it is unrealistic that the growth of α-Si from the surface can take place at a temperature above its melting point. This signifies that, in the absence of a melting point depression due to impurity segregation, it will never occur for ζ equals zero.

An illustration of the influence of ζ on the regrowth from the surface is given in figure IV.5. The simulated situation is the irradiation of 220 nm α-Si on c-Si with a 7.5 ns FWHM & 0.44 Jcm^{-2} pulse from a frequency-doubled Nd:YAG laser. Both melt temperatures were taken as that of α-Si. The figure shows that

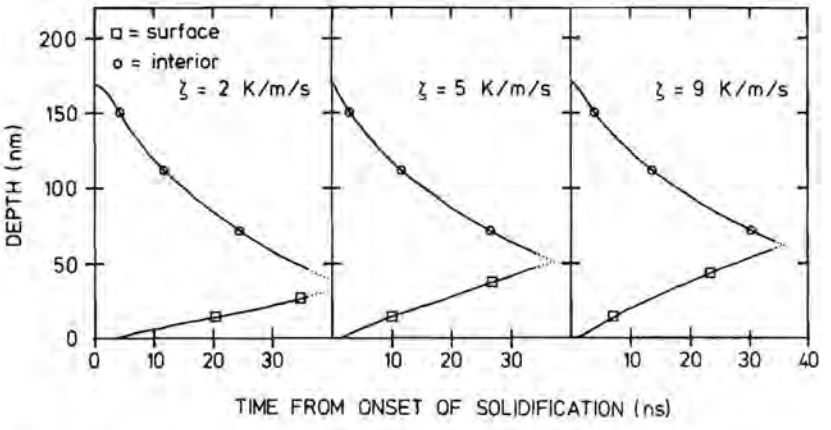

Figure IV.5. The influence of the value of ζ on the growth of α-Si from the interior and the surface. The solidification process was calculated for irradiation of 220 nm α-Si on c-Si with a 7.5 ns FWHM & 0.44 Jcm^{-2} pulse from a frequency-doubled Nd:YAG laser. The maximum melt depth was ≃170 nm, dZ = 10 nm.

ζ determines the ratio between the two growth velocities. It can be proven that this ratio goes to unity for $\zeta \rightarrow \infty$ and/or for small melt depths, which would result in a meeting point of both fronts in the middle of the originally melted region. It was derived in section I.4 that the value of ζ for α-Si can be anything between 0 and 7 K/(m/s).

Both solidification velocities depend strongly on temperature. This makes that the simulation of amorphous regrowth is more sensitive to the size of the slabs than that of e.g. the melt depth, since a difference of only a few Kelvin between the (virtual) interface temperature and the (calculated) temperature at the center of the slab has a relatively large effect on the solidification velocities. The absolute value of the calculated solidification velocity from the rear is therefore too high and that from the surface too low. The dominant temperature gradient is that in the interior α-Si layer. It reaches values of the order of 20 K/nm for the conditions of figure IV.5. The effect of the slabsize dZ on the thickness of the regrown surface layer versus time is illustrated in figure IV.6.

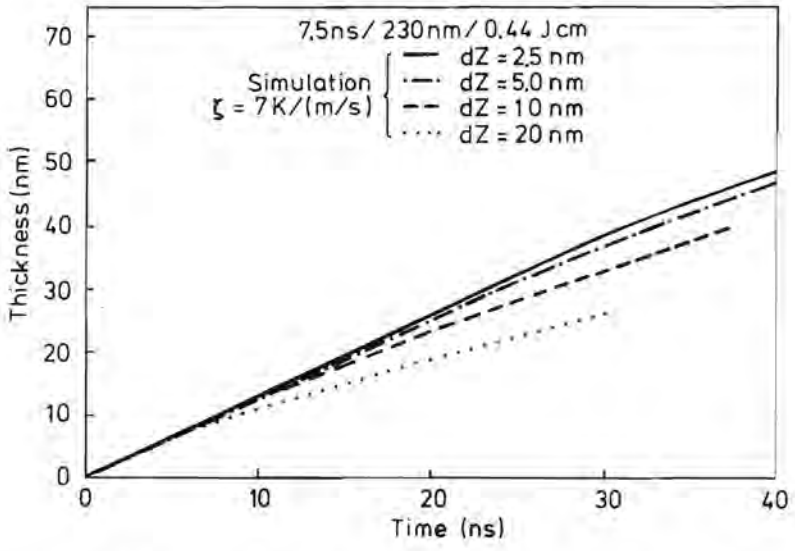

Figure IV.6. The effect of the slabsize on the simulation of regrowth from the surface for $\zeta = 7$ K/(m/s) and dZ = 2.5 (full line), 5 (dash dot), 10 (dashed), and 20 nm (dots).

The results seem to converge at a slabsize of about 1 nm. This would yield a total computation time of two full days. Fortunately, it is also possible to obtain a reasonable estimate from an extrapolation of the data in figure IV.6.

IV.4.2 Explosive crystallization

This section about XCR is built up out of two subdivisions: one concerning homogeneous / heterogeneous nucleation and one devoted to the model by Wood and Geist (1986a, 1986b). The theory of nucleation used has already been presented in chapter I. In this first section the focus will be on the implementation of two nucleation concepts: homogeneous (bulk) nucleation and heterogeneous (interface) nucleation. The two concepts do not differ much in the computer simulations, except for the value of the constants and the imbedding into the program. For each step in time dt, the number of new nuclei have to be calculated as well as the growth of the existing ones. Eventually this gives the total amount of solidified material and the released latent heat. For convenience,

the surface energy γ is taken temperature independent and a possible incubation time for nucleation has been omitted. First we consider the case of homogeneous nucleation.

The change in volume dV during the increment in time dt can be written as:

$$dV = dN\, V_{nucl} + \sum_{i=1}^{N} \frac{4\pi}{3} [(r_i + u\, dt)^3 - r_i^3] \qquad (47a)$$

where dN is the increment in the number of critical nuclei, V_{nucl} the volume of the critical nucleus, r_i the radius of the existing nucleus i, and u the growth velocity of the nuclei. If we consider the fact that $r_i \gg u\, dt$, equation 47a can be reduced to the sum of the volume change due to new nuclei and the total area of all existing nuclei times the increment in radius:

$$dV = dN\, V_{nucl} + O_{tot}\, u\, dt \qquad (47b)$$

The same reasoning can be used to obtain the change in the total area, which leads to equation 48:

$$dO = dN\, O_{nucl} + 8\pi R_{tot}\, u\, dt \qquad (48)$$

The change in the total area is the sum of the change due to new nuclei, $dN\, O_{nucl}$, and the increment in radius times 8π times the total radius of the existing nuclei, $R_{tot} \equiv \sum_{i=1}^{N} r_i$. So eventually it all comes down to the total radius and the number of nuclei:

$$dR = dN\, r_{nucl} + N\, u\, dt \qquad (49)$$

The number of new nuclei, dN, formed in the time dt is calculated by multiplying the nucleation rate I from equation 24, by the effective volume of l-Si, the slabsize dZ minus the amount of solidified material DZ, and the increment in time dt, $dN = I\,(dZ - DZ)\,dt$. Equation 16 of chapter I gives the growth velocity, $u = -85\ \mathrm{ms}^{-1}\ (1 - T_i / 1685\ \mathrm{K})$, where we used the experimentally determined value of 17 K/(m/s) for ζ to obtain the prefactor of -85 ms^{-1}. This all culminates in a change in the amount of solidified material, equation 47b, and

the corresponding release of latent heat $dV L_h$. In the case just described, nucleation and growth occur whenever l-Si is present, even during melting. This is the difference of our approach with that of Wood et al. (1984), who simulated homogeneous nucleation on an ad hoc basis by releasing a certain fraction of the latent heat for all slabs for which the temperature was below a nucleation temperature T_n at the moment in time at which solidification starts. Figure IV.7 shows an example of a simulation including homogeneous nucleation for $\zeta = 0$. The conditions were chosen to correspond with an experiment showing XCR by Sinke and Saris (1984): 220 nm α-Si on c-Si irradiated with a 32 ns FWHM & 0.2 Jcm^{-2} pulse from a ruby laser ($\lambda = 694$ nm). It is clear from the figure that homogeneous nucleation is extremely sensitive to the surface energy γ. Moreover, its value had to be reduced to about 50 % of the 0.4 Jm^{-2} obtained with expression 26 to see some effect. This observation is in good agreement with the discussion concerning this subject in section I.4. The simulations including homogeneous nucleation do not agree with the observation that the laser pulse first creates a so called primary melt, from which XCR starts (Thompson et al. 1984; Sinke and Saris, 1984). This could be the result of the omission of superheating, which would give a higher temperature in the l-Si during melting and thus a lower nucleation rate.

The modeling of heterogeneous (interface) nucleation basically uses the same equations as for homogeneous nucleation but with some adjustments. Nucleation is only permitted in a certain slab when it is melting or solidifying. Moreover, the nucleation rate and the radius/volume of the critical nucleus must be adjusted to account for the reduced surface energy term in equation 22. In this section we use the approach in which the region in which nucleation takes place is proportional to the radius of the critical nucleus, see I.4. The outcome of the simulations does not differ much from those of homogeneous nucleation except for the important fact that the value of the surface energy does not need to be changed drastically to obtain XCR (see figures IV.7 and IV.8). Again there is no indication of a primary melt, the nucleation and growth of p-Si starts immediately after melting of the surface. As with homogeneous nucleation, this could result from the omission of superheating.

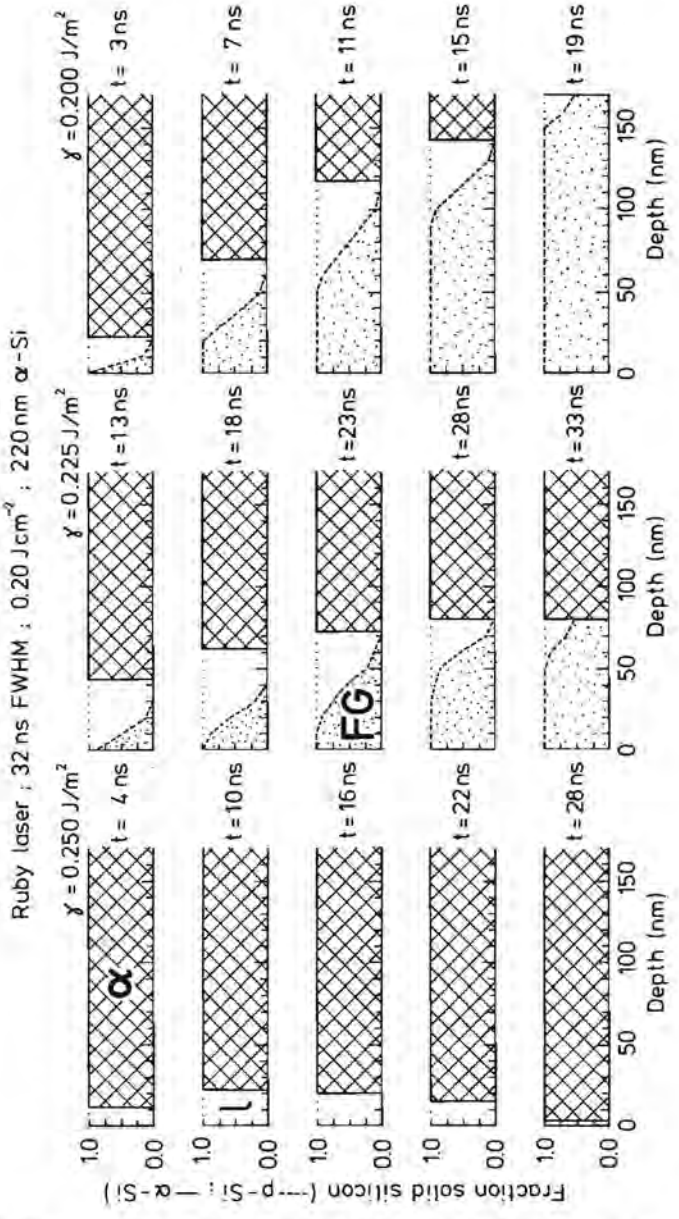

Figure IV.7. Simulation including homogeneous nucleation of the melting and solidification of 220 nm α-Si on c-Si upon irradiation with a 32 ns FWHM & 0.2 Jcm^{-2} pulse from a ruby laser ($\lambda = 694$ nm), for three values of the surface energy, dZ = 10 nm, and without superheating/undercooling ($\zeta = 0$).

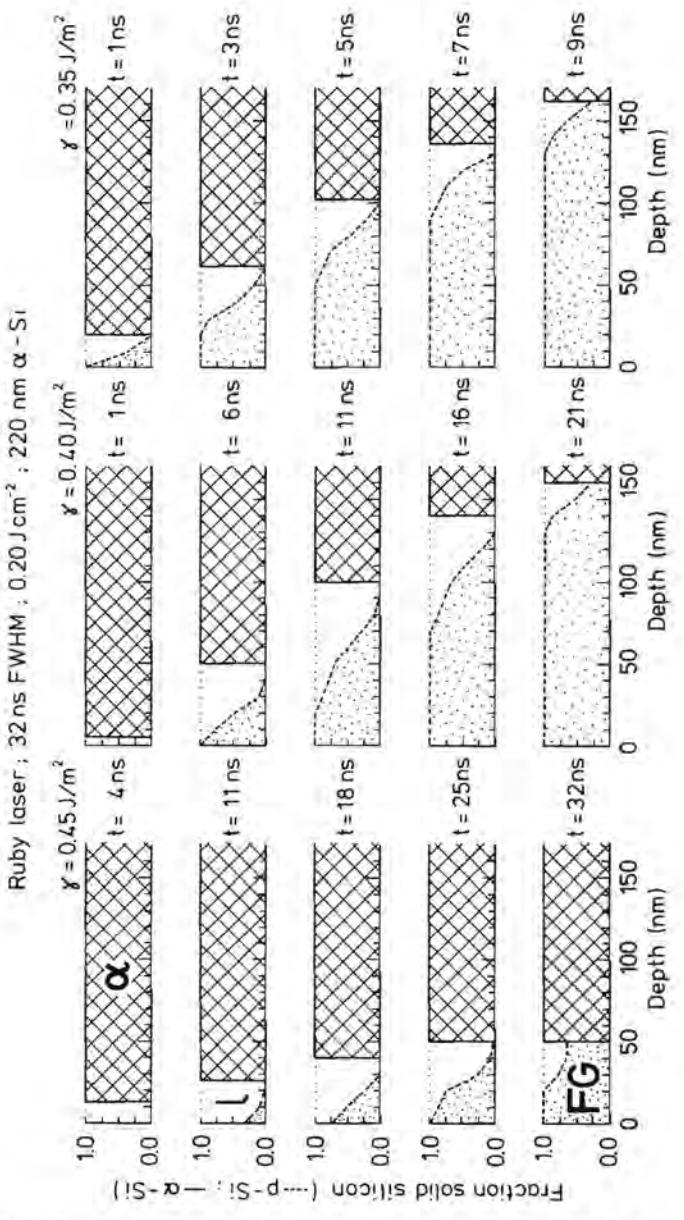

Figure IV.8. Simulation with heterogeneous nucleation of the melting and solidification of 220 nm α-Si on c-Si upon irradiation with a 32 ns FWHM & 0.2 Jcm^{-2} pulse from a ruby laser ($\lambda = 694$ nm), for three values of the surface energy, $dZ = 10$ nm, and without superheating/undercooling ($\zeta = 0$).

Recently, Wood and Geist (1986a, 1986b) published a computer model which described XCR on an ad hoc basis. With this model, the authors were able to simulate the experimental results of Thompson et al. (1984). The representation of XCR was incorporated in the following way. The absorbed energy from the impinging laser pulse melts the α-Si. If the melted slab has been below a certain nucleation temperature T_n for a certain period of time τ_n, the slab is converted to FG p-Si and is given the melting temperature of c-Si. The remaining part of the latent heat is used to melt underlying α-Si. After nucleation, the same slab acts as a seed for both the l-Si to FG p-Si transition, causing XCR to move inwards, and the l-Si to LG p-Si transformation, which grows upwards to the surface. This last process again involved a nucleation timer τ_k. The model does not contain any physical mechanism for nucleation and T_n and τ_n, τ_k have no direct physical meaning. The simulation of the experiments by Thompson et al. (1984) were done for a melting point of α-Si of 1483 K, nucleation temperature of 1523 K, FG p-Si nucleation time of 4 ns, and LG p-Si nucleation time of 8 ns. The authors did not investigate whether or not these parameter values were universal, i.e. if this set of values could be used for all experimental conditions (Wood, 1986).

A simulation of the melt and solidification behaviour for the same experimental circumstances as used above for both homogeneous and heterogeneous nucleation, with the aid of the computer model by Wood and Geist (1986), is given in figure IV.9. The calculation with the built in value of 4 ns for the nucleation time τ_n, does not show XCR. However, the reduction of τ_n to 2 and 1 ns resulted in the formation of 70 and 130 nm FG p-Si. The model did not indicate any LG p-Si formation for the given conditions. A further analysis of this model and its results will be given in chapter V.

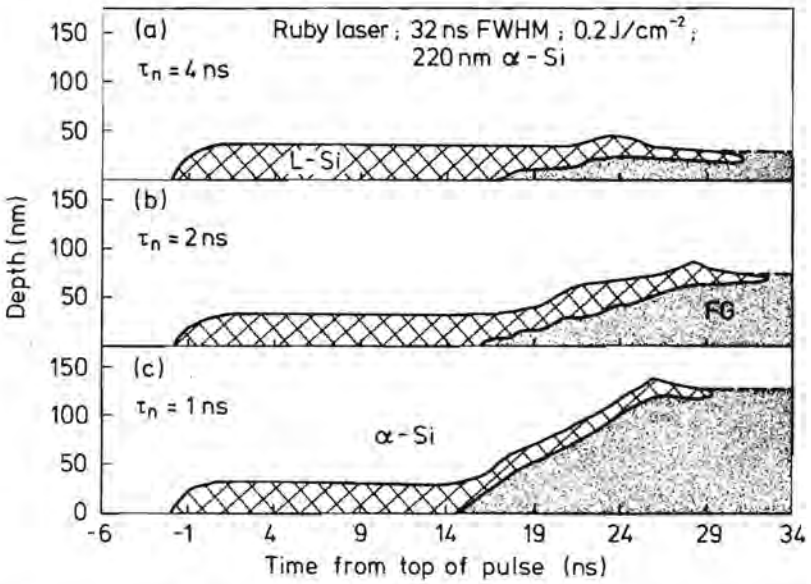

Figure IV.9. Simulation with the aid of the computer model by Wood and Geist (1986a, 1986b) of the melting and solidification of 220 nm α-Si on c-Si upon irradiation with a 32 ns FWHM & 0.2 Jcm $^{-2}$ ruby laser pulse ($\lambda = 694$ nm), for three values of the nucleation time τ_n, and $dZ = 10$ nm.

References Chapter IV

Abramowitz, M. and Stegun, I.A. (1964); *Handbook of Mathematical Functions*, (Dover Publications inc., New York, 1964), page 295.

Arden, B.W. and Astill, K.N. (1970); *Numerical Algorithms: Origins and Applications*, (Addison-Wesley, London, 1970) , page 280.

Baeri, P., Campisano, S.U., Foti, G., and Rimini, E. (1978); J. Appl. Phys. **50**, 788.

Cullis, A.G., Chew, N.G., Webber, H.C., Smith, D.J. (1984); J. Crystal Growth **68**, 624.

Cullis, A.G., Webber, H.C., and Chew, N.G. (1982); Appl. Phys. Lett. **40** , 998.

Lietoila, A. and Gibbons, J.F. (1982a); Appl. Phys. Lett. **40** , 624.

Lietoila, A. and Gibbons, J.F. (1982a); J. Appl. Phys. **53**, 3207.

Lowndes, D.H., Wood, R.F., and Narayan, J. (1984); Phys. Rev. Lett. **52** , 561.

Shank, C.V., Yen, R., and Hirliman, C. (1983a); Phys. Rev. Lett. **50** , 454.

Shank, C.V., Yen, R., and Hirliman, C. (1983b); Phys. Rev. Lett. **51** , 900.

Sinke, W. and Saris, F.W. (1984); Phys. Rev. Lett. **22**, 2121.

Smith, J.M.M. and Stammers, E. (1973); *Fysische Transportverschijnselen I*, (DUM B.V., Delft, 1973), page 101,116/117.

Thompson, M.O., Bucksbaum, P.H., and Bokor, J. (1985); Mat. Res. Symp. Proc. **35**, 181.

Thompson, M.O., Galvin, G.J., Mayer, J.W., Peercy, P.S., Poate, J.M., Jacobson, D.C., Cullis, A.G., and Chew, N.G. (1984); Phys. Rev. Lett. **52**, 2360.

Tsao, J.Y. and Peercy, P.S. (1987); Phys. Rev. Lett. **58**, 2781.

van Driel, H.M., Preston, J.S., and Gallant, M.I. (1982); Appl. Phys. Lett. **40**, 385.

van Vechten, J.A., Tsu, R., Saris, F.W., and Hoonhout, D. (1979a); Phys. Rev. Lett. **74A**, 417.

van Vechten, J.A., Tsu, R., and Saris, F.W. (1979b); Phys. Rev. Lett. **74A**, 417.

Wang, J.C., Wood, R.F., and Pronko, P.P. (1978); Appl. Phys. Lett. **33** , 455.

Wood, R.F. (1986); private communication.

Wood, R.F. and Geist, G.A. (1986a); Phys. Rev. B **34**, 2606.

Wood, R.F. and Geist, G.A. (1986b); Phys. Rev. Lett. **57**, 873.

Wood, R.F., Lowndes, D.H., and Narayan, J. (1984); Appl. Phys. Lett. **44**, 770.

Wood, R.F. and Giles, G.E. (1981); Phys. Rev. B **23**, 2923.

V. COMPARISON BETWEEN THEORY AND EXPERIMENTS

V.1 Introduction

This chapter gives the synthesis of the experimental results presented in chapter III and the model calculations introduced in chapter IV. The main part of this introduction consists of a summary of the conclusions which can be drawn from the experiments in chapter III. Section V.2 contains a comparison between the experiments that show growth from the surface and model calculations. The analysis of the data results in an estimate for the value of ζ for α-Si and reveals the influence of Cu, and probably also of every other element that shows segregation in Si, on amorphous regrowth. Section V.3 deals with the nucleation of XCR, both on itself and during amorphous regrowth. The previously determined estimate for the value of ζ is used in simulations to obtain the melt and solidification velocities as a function of time. The comparison between the experiments and the simulations leads to the formulation of a criterion for the initiation of XCR during amorphous regrowth. As an illustration of the universal character of this criterion it will be shown that, under special conditions, amorphous regrowth and XCR can also occur when working with c-Si. Associated heat-flow calculations yield a melting point of α-Si which is in good agreement with that determined by Thompson et al. (1985). The section ends with a discussion of the implication of the derived criterion for the ruby laser experiments. Eventually this leads to the conclusion that the α-Si contained c-Si nuclei before melting, probably formed during the heating phase of the laser pulse, which dominate solidification at low intensities. This is followed by section V.4, which contains the first model calculations of XCR via the process of heterogeneous nucleation proposed by Tsao and Peercy (1987). This new model is compared with the one obtained from Wood and Geist (1986), leading to a discussion of the value of the two computer models and their parameters. The chapter ends with a summary of the conclusions and a discussion of their

meaning for the understanding of the melt and solidification phenomena in α-Si on laser annealing.

The data obtained on the annealing of 225, Cu implanted, and 230 nm, Si implanted α-Si with 7.5 ns FWHM pulses from a frequency-doubled Nd:YAG laser indicate the following melting and solidification scheme: (1) The absorbed energy of the laser pulse melts the α-Si to a certain depth, which depends on the energy-density. (2) The l-Si starts to solidify into α-Si at the l-Si/α-Si interface with an average velocity of ≃2 m/s. (3) Growth of α-Si is also initiated at the surface with an average velocity of ≃1 m/s. (4) P-Si is nucleated at a liquid-solid interface during this solidification into α-Si. (5) Part of the remaining l-Si and regrown α-Si are transformed into p-Si. It is clear from the TRR and TEM results that the segregating Cu frustrates amorphous regrowth and the formation of p-Si but is not essential for the onset of growth from the surface.

In essence the same scheme applies upon irradiation of the above described Si implanted material with quasi 18 ns pulses from a frequency-doubled Nd:YAG laser. In this case, however, the longer pulse duration makes things happen at higher energy-densities. Except for low energy-densities, there is virtually no difference between the TRR data for a 7.5 ns or a 18 ns pulse for equal melt depths. This implies that the temperature gradient is mainly determined by the unmelted α-Si thickness for both cases. TEM micrographs only show p-Si which extends beyond the calculated melt depth throughout the irradiated spot. LG p-Si was not found. This points again towards growth of α-Si from both the interior and the surface, interrupted by the formation of p-Si. The longer pulse duration slightly enhances the formation of p-Si with respect to the 7.5 ns pulses.

The TRR-F and TRR-R measurements upon annealing of 440 nm, Cu implanted α-Si on 60 nm c-Si on sapphire with pulses of 7.5 ns FWHM duration from a frequency-doubled Nd:YAG laser revealed the initiation and development of XCR. Again the scheme discussed above applies. First the laser pulse melts the α-Si to a certain depth. Then solidification occurs at both the interior and the surface. However, p-Si is nucleated in a very early stage, initiating

XCR, which erases all traces of the original growth of α-Si. The fact that the doubling of the α-Si thickness has far more effect than the extension of the pulse duration proves that the effective thermal penetration depth is limited by the α-Si thickness for the case of the thinner layers.

When a 32 ns FWHM ruby laser is used to anneal the Cu implanted sample, the TRR does not appear to show amorphous regrowth anymore. Instead, interferences from an explosively propagating l-Si layer can be detected for low energy-densities. A maximum mean velocity of 13 ± 2 m/s could be determined for the XCR front from these interferences. The high reflectivity peak at moderate energy-densities, associated with surface melting, does not reach the value for pure l-Si. Its behaviour in time and with energy-density, points towards the presence of p-Si in the primary melt.

In the remaining part of this chapter we focus on the comparison between the experiments and the model calculations in order to unravel the observed phenomena and to study the underlying physical principles and parameters.

V.2 Amorphous Regrowth: a Comparison between Model Calculations and Experiments

There are two adjustable parameters in the model described in chapter IV: ζ, the velocity-superheating/undercooling factor, and T_{init}, the initiation temperature for growth from the surface. The value of ζ determines the ratio between both solidification velocities, see section IV.8. T_{init} mainly influences the starting point in time for growth from the surface. ζ is affected by the presence of impurities at the solidification fronts, while T_{init} could e.g. depend on the structure and composition of the surface. If α-Si really has a well defined melting point, however, T_{init} is not expected to differ from it. Moreover, the variation in starting time as a function of T_{init} is of the order of the experimental uncertainty in the timing. We have therefore chosen to fix T_{init} at 1460 K and perform a one parameter fit to ζ. Very little is known about the parameters governing amorphous regrowth. Computer simulations can yield an estimate for the value of ζ and will increase the insight into the role of impurities on the phenomenon of amorphous regrowth from the surface.

To be able to compare the simulations with the experiments, the TRR data were translated into an α-Si thickness, and the simulations have been used to obtain a reflectivity value with the aid of the data given in figure III.4 for $\lambda = 633$ nm. The fact that many TRR measurements were obtained at a different wavelength, $\lambda = 647$ nm, is of no concern since the location of the extrema is nearly the same for both probe wavelengths. A reasonable estimate for the ζ of α-Si can only be obtained from the comparison between simulations and well defined and clear TRR data. This means that, in the first instance, the experiments on the Cu implanted material and with the extended pulse duration can not be used for this purpose, which leaves the irradiation of the Si implanted α-Si with 7.5 ns pulses. To avoid computational difficulties, all simulations in this chapter were performed with a symmetrical velocity-superheating/undercooling relationship. The argument against such a symmetric relation given by Tsao et al. (1986) is based on the difference in entropy between c-Si and l-Si. Since the entropy difference between α-Si and l-Si is smaller, the

proposed asymmetry must be reduced. Moreover, the effect of superheating on solidification is always small (see section IV.3.1).

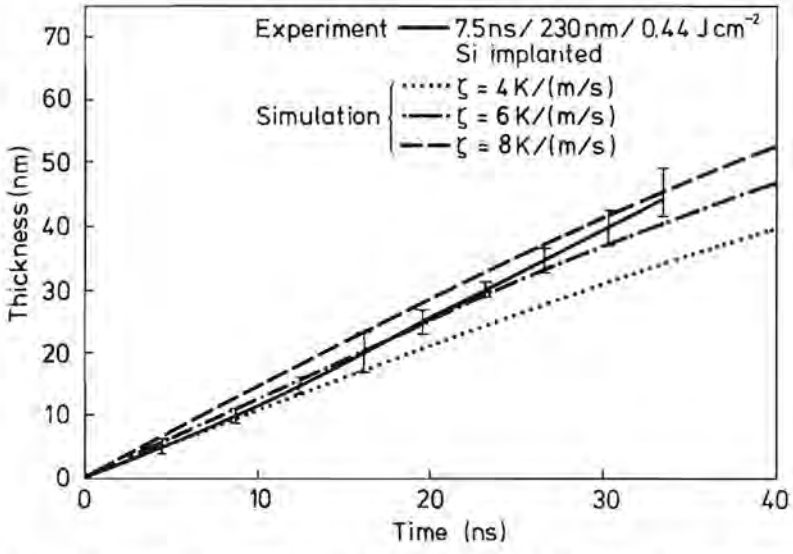

Figure V.1. Thickness versus time of the solidified α-Si surface layer after irradiation of 230 nm, Si implanted α-Si with a 7.5 ns FWHM pulse from a frequency-doubled Nd:YAG laser at 0.44 Jcm^{-2}. Comparison between values deduced from the measured TRR data (full line) and model calculations for $dZ \rightarrow 0$ and $\zeta = 4$ (dots), 6 (dash dots), and 8 (dashes) K/(m/s).

Figure V.1 shows the thickness versus time of the solidified α-Si surface layer after irradiation of 230 nm, Si implanted α-Si with a 7.5 ns FWHM & 0.44 Jcm^{-2} pulse from a frequency-doubled Nd:YAG laser, both deduced from the TRR data (full line) and simulated for $\zeta = 4$ (dots), 6 (dash dot), and 8 (dashes) K/(m/s). The calculated curves are extrapolations for $dZ \rightarrow 0$, see section IV.4.1. The error bars in the experimental curve are based on an uncertainty in the initial (static) reflectivity of ±2 %. The error increases with increasing thickness because the extrema are filled up at greater depth due to absorption. It is obvious that growth from the surface can be simulated rather well for $\zeta \simeq 6$ K/(m/s). The slope (=velocity) of the experimental curve seems to increase in time while that of the simulations decreases, but this is only a minor effect. The fit is further illustrated in figure V.2, which shows the measured and simulated

TRR data for growth from the surface. The measured temporal reflectivity evolves slightly faster than the simulated ones after the minimum at t≃15 ns. Note that this situation applies for self-implanted material.

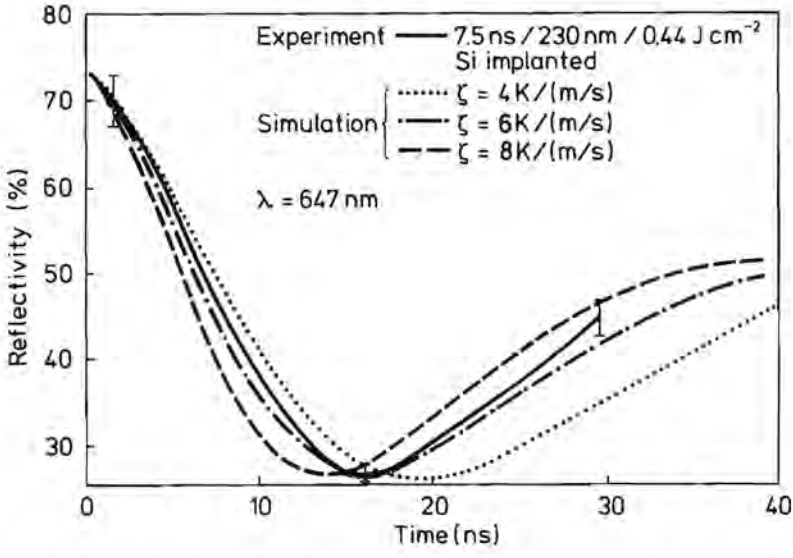

Figure V.2. Comparison between the measured and the simulated TRR signals for the annealing of 230 nm, Si implanted α-Si by a 7.5 ns FWHM & 0.44 Jcm^{-2} pulse from a frequency-doubled Nd:YAG laser. The simulations were performed for $dZ \rightarrow 0$ and $\zeta = 4$ (dots), 6 (dash dot), and 8 (dashed) K/(m/s).

Based on the data discussed above and given the experimental uncertainties we come to the following conclusion:

The value of ζ for the solidification of α-Si is 6±2 K/(m/s).

This value is within the range of 0-7 K/(m/s) deduced in section 1.4 and equal to the upper limit for superheating in c-Si discussed by Peercy et al. (1987). Note that this value applies to solidification i.e. it gives the relation between the velocity of and the undercooling at the solidification front.

It is interesting to compare the simulated curves of figures V.1 and V.2 with the data for the Cu implanted sample. Figure V.3 shows the deduced temporal thickness of the regrown surface layer together with the simulated data of figure V.1. The experiment does not fit the simulations for ζ between 4 and 8 K/(m/s), except for times <5 ns. The experimental curve exhibits an increas-

ing slope for α-Si thicknesses below 20 nm. Beyond this value the growth proceeds with a more or less constant velocity of 1.5 m/s. For comparison, the calculated curves correspond to a growth velocity of approximately 1.2, 1.1, and 1.0 m/s for ζ values of 8, 6, and 4 K/(m/s) respectively. The final α-Si surface layer thickness, 70 nm, is more than 20 nm above the value for the Si implanted material.

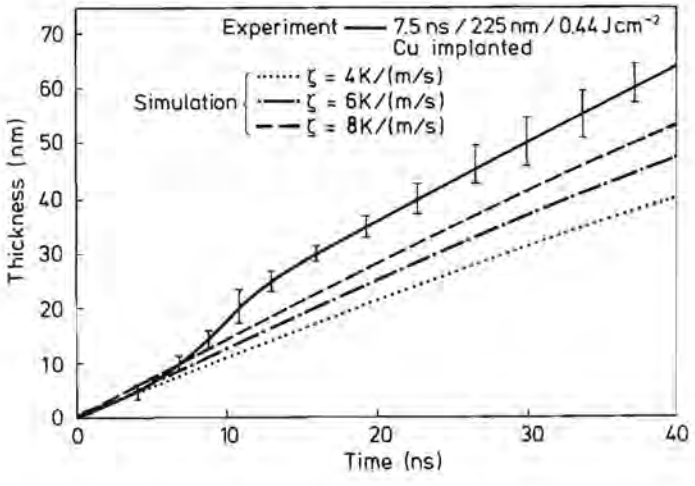

Figure V.3. Thickness versus time of the solidified α-Si surface layer after irradiation of 225 nm, Cu implanted α-Si with a 7.5 ns FWHM pulse from a frequency-doubled Nd:YAG laser at 0.44 Jcm^{-2}. Comparison between values deduced from the measured TRR data (full line) and model calculations for $dZ \rightarrow 0$ and $\zeta = 4$ (dots), 6 (dash dot), and 8 (dashes) K/(m/s).

Figure V.4 shows the associated measured and simulated TRR signals. It is again obvious that the experimental data can not be fitted for a fixed value of ζ. We have already stated in chapter III that the segregating Cu could increase the effective value of ζ and/or cause a significant melting point depression. Both phenomena tend to equalize the solidification velocities, decreasing that from the rear and increasing that from the surface, see section III.2.6. This hypothesis is clearly supported by the temporal behaviour of the experimental data in figure V.4. In conclusion:

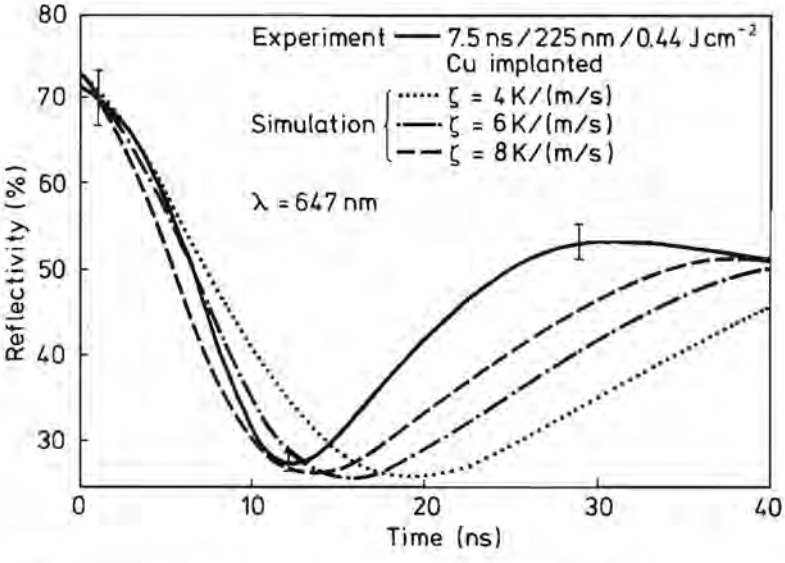

Figure V.4. Comparison between the measured and the simulated TRR signals for the annealing of 225 nm, Cu implanted α-Si by a 7.5 ns FWHM & 0.44 Jcm^{-2} pulse from a frequency-doubled Nd:YAG laser. The simulations were performed for $dZ \rightarrow 0$ and $\zeta = 4$ (dots), 6 (dash dots), and 8 (dashes) K/(m/s).

the segregating Cu increases the effective value of ζ

It it very likely that all elements which show segregation will have this effect on amorphous regrowth.

Unfortunately, the model can not deal with a full calculation inclusive of the segregation of Cu and a melting point depression. This is not merely an implementation problem. It would require the velocity and concentration dependent segregation coefficient and the value of $\partial T_{melt}/\partial[Cu]$ for the Cu/l-Si/α-Si system, which are completely unknown. Assuming equal velocities, we obtain a total solidification velocity of $\simeq 3$ m/s, in good agreement with model calculations, see figure V.7.

Figure V.5 shows the temporal surface layer thickness both deduced from the TRR signal after irradiation of the Si implanted material with an 18 ns & 0.44 Jcm^{-2} pulse and simulated for $\zeta = 6$ K/(m/s). The curves are reasonably similar, despite the different pulse shapes in the experiment and the simulation. This is in line with our earlier statement that the pulse duration has only a mi-

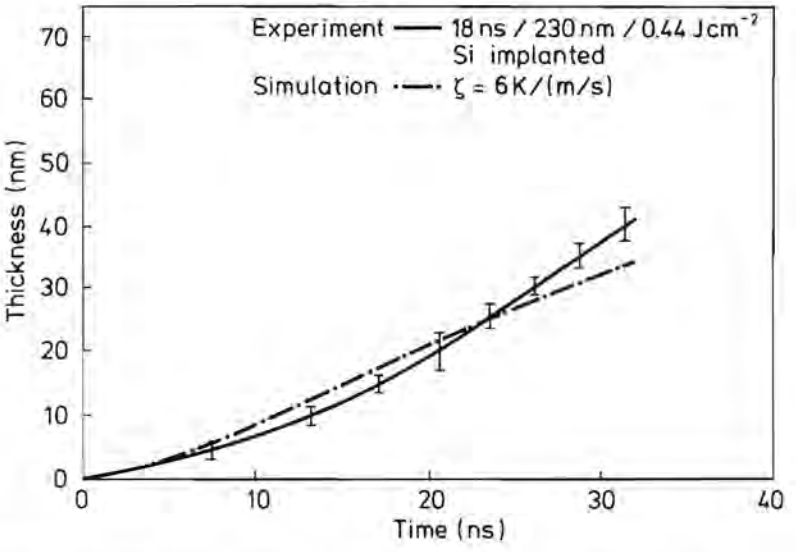

Figure V.5. Thickness versus time of the solidified α-Si surface layer after irradiation of 230 nm, Si implanted α-Si with a 18 ns pulse from a frequency-doubled Nd:YAG laser at an energy-density of 0.44 Jcm^{-2}. Comparison between values deduced from the experimental TRR data (full line) and model calculations for $dZ \rightarrow 0$ and $\zeta = 6$ K/(m/s) (dash dotted line).

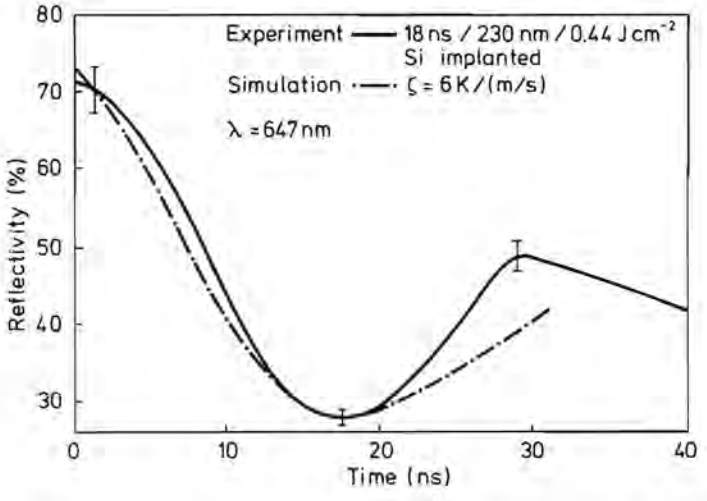

Figure V.6. The measured and simulated TRR signals for the annealing of 230 nm, Si implanted α-Si by an 18 ns & 0.44 Jcm^{-2} pulse from a frequency-doubled Nd:YAG laser. The simulations were performed for $\zeta = 6$ K/(m/s) (dash dotted line).

nor effect on the solidification. The curvature of the experimental data, indicating a continuously increasing velocity, is somewhat more pronounced than for the 7.5 ns pulse. This could, however, be caused by the difference in melt depth between the two situations. Figure V.6 shows the TRR signals corresponding with the data of figure V.5.

V.3 The Nucleation of Explosive Crystallization

V.3.1 The nucleation of XCR during α-Si growth

The analysis in the previous section has yielded an estimate for the value of ζ for α-Si. This estimate enables us to calculate the melt and solidification velocities versus time for the various experimental conditions. Figure V.7 shows such a simulation for the irradiation of 230 nm α-Si with a 7.5 ns FWHM pulse from a frequency-doubled Nd:YAG laser at an energy-density of 0.44 Jcm^{-2}.

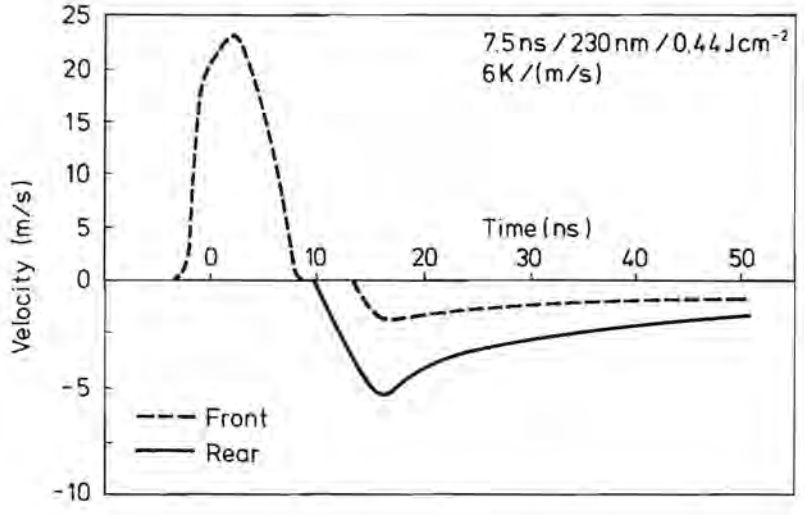

Figure V.7. Simulated melt and solidification velocities versus time for the irradiation of 230 nm α-Si with a 7.5 ns FWHM pulse from a frequency-doubled Nd:YAG laser at an energy-density of 0.44 Jcm^{-2} and $\zeta = 6$ K/(m/s). Positive velocities correspond with melting and negative velocities with solidification. Note the change in the velocity scale.

The simulations indicate a maximum melt velocity of 20 m/s. Solidification starts with amorphous growth from the rear (full line), which is followed by amorphous growth from the surface (dashed line). The total solidification velocity, the sum of the absolute value of the growth velocity from the rear and that from the surface, has a maximum of approximately 7 m/s. The experiment only showed amorphous regrowth upto ≃48 ns after the peak of the laser pulse.

According to the simulations, there is still a l-Si layer of about 20 nm present at that time. Note that the model predicts that the velocity of growth from the surface has a reasonably constant value of $\simeq 1$ m/s during tens of nanoseconds.

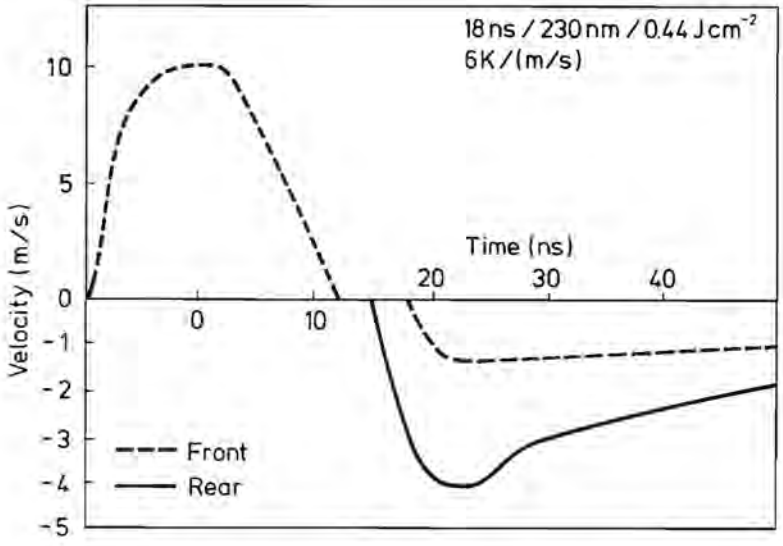

Figure V.8. Simulated melt and solidification velocities versus time upon annealing of 230 nm α-Si with an 18 ns FWHM & 0.44 Jcm^{-2} pulse from a frequency-doubled Nd:YAG laser, for $\zeta = 6$ K/(m/s). Positive velocities correspond with melting, negative velocities with solidification. Note the change in the velocity scale.

The simulated temporal melt and solidification velocities upon irradiation of 230 nm α-Si with an 18 ns FWHM pulse from a frequency-doubled Nd:YAG laser at an energy-density of 0.44 Jcm^{-2} are depicted in figure V.8. The melt velocity is approximately halved compared to the data for the 7.5 ns pulse. However, the longer pulse duration hardly influences solidification. The maximum total solidification velocity is $\simeq 5.5$ m/s, only 1.5 m/s less than for the shorter pulse. This difference will be even smaller if we compare results of equal melt depth instead of equal energy-density. Experimentally, amorphous regrowth ends approximately 50 ns after the peak of the laser pulse. The simulations indicate the presence of a l-Si layer of about 30 nm at that moment. The

growth velocity from the surface (dashed line) is again approximately 1 m/s during tens of nanoseconds, analogous to the behaviour for the shorter pulse.

The scenarios discussed above both suggest that it is the combination of velocity and time, rather than just the velocity, which triggers the formation of p-Si during amorphous regrowth. Unfortunately the definition of the moment of nucleation, for these experiments, is insufficiently accurate for a quantitative analysis. The situation is much better for the experiments on the 440 nm thick α-Si layer. The simultaneously recorded TRR-F and TRR-R signals enable us to determine the moment of nucleation more precisely. It is therefore the comparison between these experiments and their simulation which ultimately leads to a criterion for the initiation of XCR during amorphous regrowth.

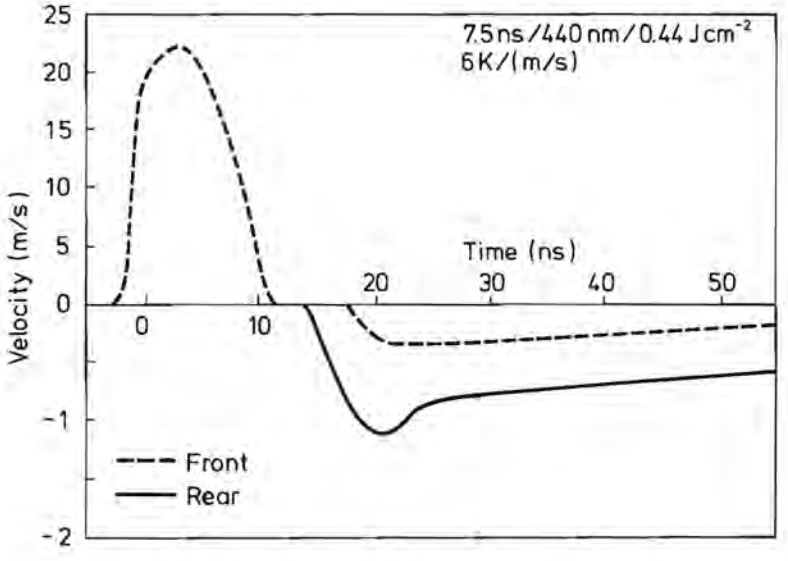

Figure V.9. Simulated melt and solidification velocities versus time for the irradiation of 440 nm α-Si on 60 nm c-Si on sapphire with a 7.5 ns FWHM pulse from a frequency-doubled Nd:YAG laser at an energy-density of 0.44 Jcm^{-2}, for $\zeta = 6$ K/(m/s). Positive velocities correspond with melting, negative velocities with solidification. Note the change in the velocity scale.

The simulated temporal melt and solidification velocities upon annealing of 440 nm α-Si on 60 nm c-Si on a sapphire substrate with a 7.5 ns FWHM

& 0.44 Jcm ^{2} pulse from a frequency-doubled Nd:YAG laser are depicted in figure V.9. As can be expected, the temporal behaviour of the melt velocity is nearly the same as for the thinner layer and the same pulse, see figure V.7. The maximum value is a little higher and the slope of the falling edge (deceleration) somewhat weaker because of the thicker unmelted α-Si layer and thus less loss of heat. This effect is much more pronounced for the solidification velocities. Apart from a short period of time, both the regrowth velocity from the rear (full line) and that from the surface (dots) are below 1 m/s. The solidification front from the surface in fact never propagates faster than 0.5 m/s, according to the simulations.

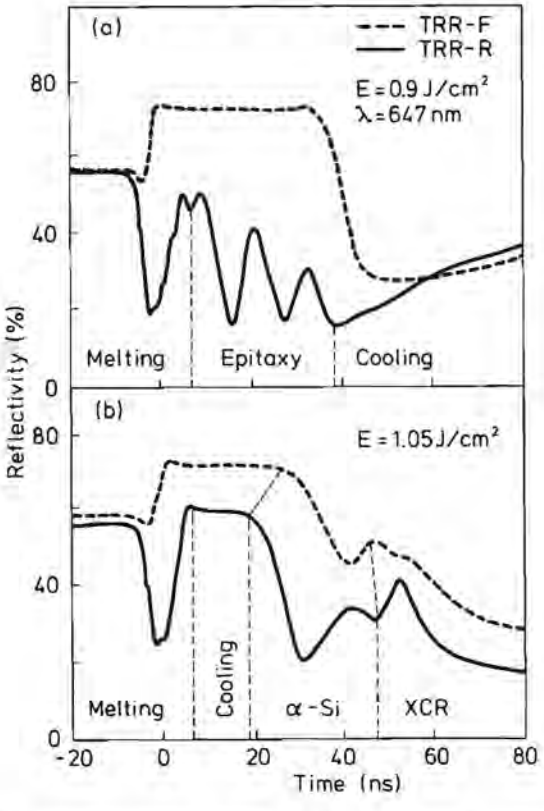

Figure V.10. TRR measurements from the front (upper curve) and the rear (lower curve) for irradiation with a 7.5 ns FWHM & 0.41 Jcm^{-2} pulse from a frequency-doubled Nd:YAG laser of 440 nm α-Si on 60 nm c-Si on sapphire. Both signals are normalized with respect to their initial (static) reflectivity value.

Figure V.10 shows the TRR-F and TRR-R signals upon irradiation at 0.41 Jcm^{-2}, which can be compared with the data in figure V.9. The slight difference in energy-density between the simulation and the experiment is not significant. Melting starts approximately 2 ns before and ends about 10 ns after the top of the laser pulse according to the TRR data, in good agreement with the simulation. Next, the liquid-solid front reverses and the TRR-R signal decreases slightly, followed by a slow increase. The onset of the falling edge in the high reflectivity phase of the TRR-F measurements occurs about 15 ns after the peak of the laser pulse. It has been argued in chapter III that this feature marks the beginning of growth from the surface. This timing is in reasonable agreement with the simulation which gives $\simeq$17 ns as the starting point. The position of the minimum in the TRR-F corresponds with the end of regrowth from the surface. This can be inferred from the observation that there is no time delay between the minima at different wavelengths, see section III.4. Both the TRR data and the simulation indicate that there is still a l-Si layer of more than 100 nm left at that time. The TRR-R suggests that the solidification from the interior has also stopped at this point and is followed by the initiation of XCR after a delay of about 4 ns.

The TRR measurements of the three cases just described all indicate the end of amorphous regrowth at a time for which the corresponding simulations still exhibit a l-Si layer which is undercooled with respect to the α-Si melting point. We therefore believe that the end of amorphous regrowth in the experiments is caused by the nucleation of p-Si at the upper solidification front and that this nucleation is soon followed by the formation of p-Si at the interior liquid-solid interface. The small peak after the minimum in the TRR-F can then be associated with the transformation of the thin (<20 nm) α-Si surface layer into p-Si. This statement is consistent with the observed time delay between the end of growth from the surface and the initiation of XCR at the rear. The time delay is, however, too short to explain the observed phenomena by the nucleation at the α-Si surface layer alone. Even with the maximum c-Si growth velocity of 15 m/s it takes longer than the observed 4 ns to solidify the more than 100 nm of l-Si. This hypothesis is confirmed by the data in figure V.11.

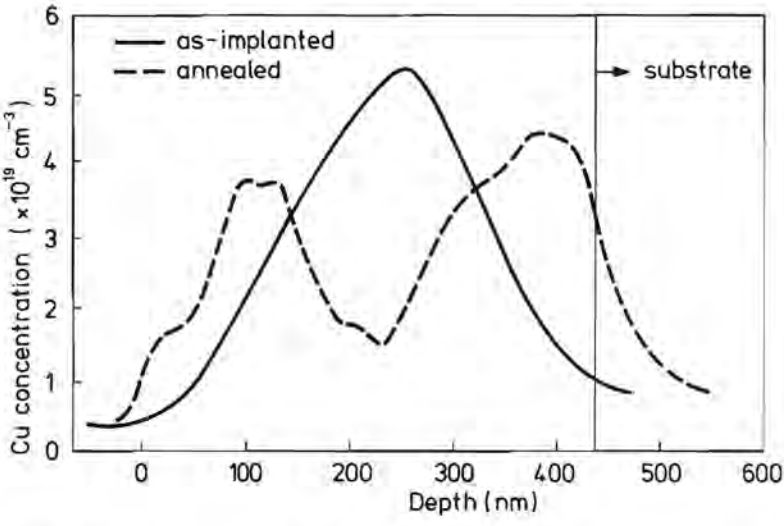

Figure V.11. RBS measurement of the Cu distribution before (dashed line) and after (full line) irradiation of 440 nm α-Si on 60 nm c-Si on sapphire with a 7.5 ns FWHM & 0.49 Jcm^{-2} pulse from a frequency-doubled Nd:YAG laser.

It shows the Cu profile before and after irradiation of this material at an energy-density of 0.49 Jcm^{-2}. After annealing (dashed line), the Cu profile clearly shows two peaks; one ≃100 nm below the surface and one at the original α-Si/c-Si interface. The latter one originates from the XCR front which starts at ≃200 nm and ends at or very near the substrate. The buried Cu peak at ≃100 nm results from two p-Si fronts: again the one starting at ≃200 nm, since it travels both ways thereby transforming as well α-Si as l-Si into p-Si, and the one starting from the upper solidification front going downward. They apparently travelled about the same distance, since the peak lies half-way between the melt depth inferred from the corresponding TRR data and the simulation. In summary, the TRR, RBS and simulated data show that the p-Si was nucleated at the solidification front from the surface, after ≃10 ns of growth at a velocity <0.5 m/s. The data for the thinner α-Si layer in this section suggest that this incubation time is ≃20 ns at about 1 m/s. This brings us to the following conclusions:

1. **Amorphous regrowth is the basic solidification process on irradiation of α-Si with short laser pulses.**
2. **Polycrystalline Si is nucleated if the growth of α-Si proceeds at a velocity of 0.5(1) m/s during 10(20) ns.**

The presence of a non-negligible incubation time was never observed before. The analysis in section 1.4 indicates that it is not impossible. Moreover, an incubation time of the same order of magnitude has been derived by Devaud (1986). The nucleation mechanism itself is unknown. Two possible candidates are nucleation in solid &aSi, (Roorda et al. 1988) and nucleation at the α-Si/l-Si interface (Tsao and Peercy; 1987). The observed velocity dependence of the incubation time seems to favour the latter one.

The phenomenon of the initiation of XCR during amorphous regrowth, just described, is not limited to the irradiation of α-Si on c-Si but can also occur in c-Si on sapphire. For energy-densities below the threshold for total melt-through, solidification proceeds via epitaxial growth on the remaining c-Si. However, amorphous regrowth will take place for energy-densities sufficient to completely melt the c-Si layer. The idea behind this is that the sapphire substrate will look amorphous to the solidifying Si because it has a lattice constant which is ≃10 % smaller. This is demonstrated in figure V.12 which shows the TRR-F and TRR-R signals upon irradiation of 200 nm c-Si on sapphire with 7.5 ns FWHM pulses from a frequency-doubled Nd:YAG laser at (a) 0.9 Jcm^{-2} and (b) 1.05 Jcm^{-2}. The TRR-F signal in figure V.12a, at 0.9 Jcm^{-2}, has a HRP with a duration of ≃40 ns. Apart from the HRP, there is no further structure. The corresponding TRR-R measurement is full of oscillations due to the inward moving melt- and upward moving solidification front. The end of the melt-in phase can be recognized by the reversal of the liquid-solid interface at t≃5 ns. The interferences caused by the propagating melt front are not resolved, which can be understood if one bears in mind that the reflectivity oscillations following t=5 ns are also present during melt-in but now within a time interval of only 7 ns. The TRR-R signal does not have a plateau, which indicates that the melt front did not reach the sapphire substrate for this energy-density. Moreover, the moment in time for which the HRP ends corresponds

with the end of the interferences in the TRR-R signal. From the oscillations during the solidification phase we estimate a melt depth of ≃180 nm and a solidification velocity of ≃6 m/s. The (static) reflectivity values before and after the experiment were identical. In summary, the TRR-F and TRR-R measurements of figure V.12a correspond with melting and epitaxial regrowth of the c-Si layer.

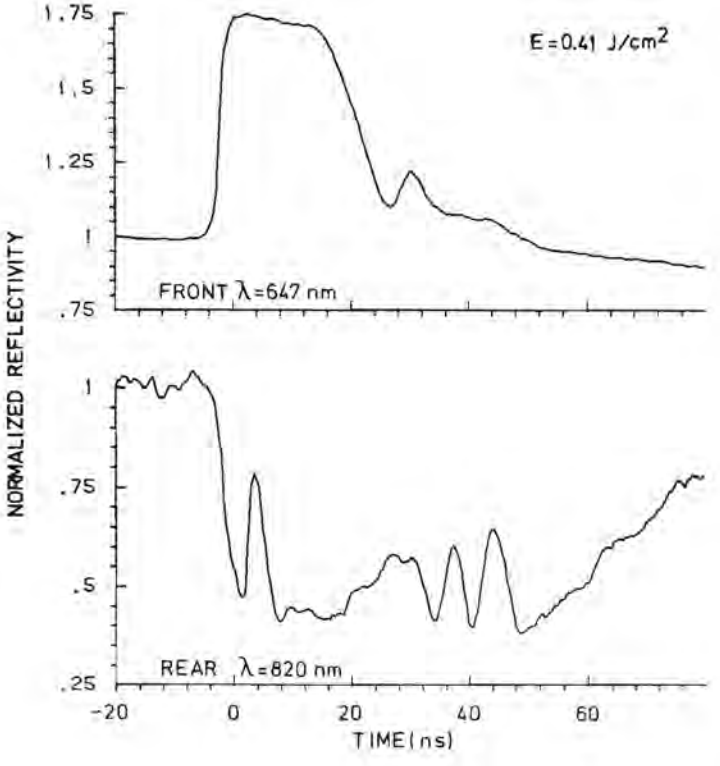

figure V.12. TRR-F and TRR-R measurements at $\lambda = 647$ nm upon annealing of 200 nm c-Si on sapphire with 7.5 ns FWHM pulses from a frequency-doubled Nd:YAG laser at (a) 0.90 Jcm^{-2}, and (b) 1.05 Jcm^{-2}.

This situation is different for the case of 1.05 Jcm^{-2}, figure V.12b. The first interesting observation is that the HRP in the TRR-F has a duration of only $\simeq$25 ns. This is rather unexpected, since the HRP duration of the experiment at 0.9 Jcm^{-2} was $\simeq$40 ns. Furthermore, the TRR-F signal contains a structure after the HRP, at t$\simeq$45 ns, similar to those observed on irradiation of the 440 nm α-Si on 60 nm on sapphire with the same laser (see figure III.21). The simultaneous measurement of the TRR-F at two wavelengths revealed that the minimum is a real interference minimum and that the small maximum is caused by the end of growth from the surface. The TRR-R signal also has intriguing features. It is obvious that the interferences during melting are again unresolved. However, the minimum at t$\simeq$0 ns is now followed by a HRP with a surprisingly long duration of approximately 16 ns. The end of the HRP in the TRR-R at t$\simeq$21 ns is followed by that in the TRR-F with a delay of about 5 ns. A heat-flow calculation revealed that both events occur at a temperature of 1470$\pm$40 K, close to the 1460$\pm$25 K for the melting point of α-Si determined by Thompson et al. (1985). The HRP's are succeeded by slow oscillations in the reflectivity. The time scale of the oscillations indicates a solidification velocity of $\simeq$1 m/s from the surface and $\simeq$2 m/s from the rear. It is clear that the amplitude of the slow interferences in the TRR-R does not compare with that in figure V.12a. The reduced value of the first maximum points towards growth of a phase with a higher absorption compared to c-Si. The slow interferences are suddenly followed by a fast phenomenon. From the magnitude of the sharp peak at t$\simeq$53 ns, and from experiments with two probe wavelengths it follows that the liquid-solid front reverses once more at the onset of the fast feature at t$\simeq$47 ns. The irradiated area showed a decreased reflectivity and enhanced absorption after the experiment. A TEM picture of the material after irradiation at 1.16 Jcm^{-2} is given in figure V.13. The image features a completely crystallized layer with a very interesting polycrystalline structure which we have seen before in section III.2.8: fine grain p-Si at the surface and large grain p-Si at the interior. This inversion of the FG and LG p-Si, if compared to XCR, has also been observed in α-Si at high energy-densities by Narayan and White (1984), who did not give an explaination for it.

The following scheme emerges when the TRR-F and TRR-R signals of figure V.12b are compared. The laser pulse melts the c-Si layer up to the sapphire substrate. Since the Si does not fit on the sapphire, it can not grow epitaxially and the temperature of the liquid decreases below 1685 K, the melting point of c-Si. Solidification can only start after that the temperature has dropped below the melting point of α-Si. This solidification bottle-neck explains the relatively long duration of the HRP in the TRR-R signal. At this point the liquid has no longer any memory of the fact that it was formed out of c-Si and it starts to solidify into α-Si, first at the interior later also at the surface. Nucleation occurs at the upper solidification front after about 20 ns of growth at a velocity of approximately 1 m/s. The c-Si nuclei expand rapidly in the melt and the with this growth associated release of latent heat raises the temperature so that the α-Si at the interior is melted again. Since crystallization proceeds towards the rear, the grain size will increase in that direction due to preferential growth. This explains the occurrence of FG p-Si at the surface and LG p-Si at the interior.

Figure V.13. TEM image of after irradiation of 200 nm c-Si on sapphire with a 7.5 ns FWHM & 1.16 Jcm^{-2} pulse from a frequency-doubled Nd:YAG laser.

The experiments with the c-Si on sapphire show once more that XCR is initiated after ≃20 ns of amorphous growth at a velocity of about 1 m/s. Furthermore, it can be concluded that the sapphire indeed acts as an amorphous substrate at these solidification velocities. The comparison between the TRR data and model calculations yields that amorphous regrowth occurred at a

temperature of 1470±40 K, close to the 1460±25 K found for the melting point of α-Si by Thompson et al. (1985) under similar conditions.

V.3.2. The initiation of XCR in the ruby laser experiments

It is clear from the data presented in chapter III that the ruby laser experiments do not satisfy the schemes derived in the previous section. The seemingly instantaneous presence of c-Si nuclei in the primary melt at low energy-densities, suggested for the ruby laser measurements, is in contrast to the apparent incubation time for nucleation of tens of nanoseconds in the Nd:YAG experiments. In general there are three possible causes for the presence of nuclei in the liquid: (1) homogeneous nucleation in the l-Si, (2) heterogeneous nucleation at a l-Si/α-Si interface, and (3) at nuclei already present before melting. The first possibility can be ruled out based on the experiments of Devaud and Turnbull (1985) previously discussed. The second mechanism would require a very short (< 1 ns) incubation time and is therefore unrealistic given the values found in section V.3.1 which are reasonably long (> 10 ns). The third possibility, however, is not unrealistic at all.

Homogeneous nucleation can also occur in the solid phase, as was discussed in section I.4. An extrapolation of the data of Roth and Olson (1987) to 1460 K, the apparent melting point of α-Si when irradiated with pulses in the nanosecond regime (Thompson et al. 1985, Sinke et al. 1988), yields a nucleation rate of one per 10 μm^3 per nanosecond. Roorda et al. (1988) recently showed that a density of $\simeq 10^{17}$ nuclei per m^{-3} can be achieved in only one 32 ns FWHM pulse from a ruby laser, the same laser conditions as in our experiments, at 90 % of the energy-density for surface melting. Upon melting, the density of nuclei can be many orders of magnitude higher since the nucleation rate increases drastically with temperature. Narayan et al. (1984) observed the presence of microcrystallites near the surface and the α-Si/c-Si interface in high-resolution TEM (HTEM), in as-implanted layers which would normally be considered completely amorphous. The size of these nuclei is so small (<30Å) that they can not be detected by normal TEM, e.g. in figure II.15. Also

a HTEM study of our 225 nm Cu implanted α-Si, however, did not give any evidence for the existence of such c-Si embryos. Therefore we can state that:

The formation of c-Si nuclei during heating of solid α-Si dominates melting and solidification at low energy-densities for long laser pulses.

High energy-density pulses result in a short heating time of the solid and high temperatures in the liquid, thus low densities and/or melting of nuclei. Simulations, including superheating and reflectivity effects, show that the surface temperature reaches the c-Si melting point at $\simeq 0.5$ Jcm^{-2} for the ruby laser experiments. The actual melting temperature of the nuclei can be anything between the melting point of α-Si , for small particles, and that of c-Si, for large particles (see eq. 22). Therefore, it is presumably not necessary to exceed the melting temperature of c-Si in order to melt all nuclei. The Nd:YAG experiments have larger heating rates and higher l-Si temperatures. Heat-flow calculations indicate that the surface temperature reaches the melting point of c-Si already for 0.2 Jcm $^{-2}$. The influence of nucleation in the solid phase is therefore not only reduced but also confined to a narrow energy-density interval, which explains the inconspicuousness of solid phase nucleation in the experiments with the Nd:YAG laser.

V.4 The Simulation of Explosive Crystallization via Heterogeneous Nucleation

V.4.1 General considerations

The Nd:YAG laser experiments have shown the existence of an incubation time for the nucleation of p-Si at the l-Si/α-Si front. In the previous section we have discussed that the ruby laser experiments indicate the formation of c-Si nuclei in the solid α-Si during heating. This suggests that XCR is initiated by this mechanism, but does not necessarily mean that its also sustained in this way. It is therefore still interesting to investigate whether the process of heterogeneous nucleation at the l-Si/α-Si front, proposed by Tsao and Peercy (1987), can be the nucleation mechanism which drives the explosively propagating l-Si layer. The basic methods for the simulation of heterogeneous nucleation have been presented in chapter IV. However, the initiation and growth of LG p-Si remains to be discussed.

The basic ideas underlying our model are that the FG p-Si is formed at the l-Si/α-Si interface and that growth of LG p-Si initiates at the l-Si/FG p-Si front. Nucleation was allowed to take place as soon as the melt front stopped. In other words, an incubation time of 0 ns. The underlying idea is that the already present c-Si embryos will initiate XCR as soon as the temperature at the interface approaches the melting point of the α-Si. The formation rate of the FG p-Si is described by equations 24a and 24b of chapter I, where the density of atoms in the volume of the liquid $N_{l\text{-}Si} = 5.5 \times 10^{28}\ m^{-3}$ is replaced by the density of atoms per unit area of the c-Si (100) plane $6.8 \times 10^{18}\ m^{-2}$, see section I.4. The growth velocity of the LG p-Si is determined by the ζ value for c-Si: 1 m/s for every 17 K undercooling of the melt with respect to 1685 K. All calculations shown were performed for a symmetrical velocity-superheating/undercooling relationship, with a ζ value of 7 K/(m/s) for the α-Si, and with fully temperature dependent parameters. The surface energy γ between the liquid and the crystal, the only surface energy which enters into the calculations, is a fit parameter in the model. For that purpose, expression 26 is multiplied by a so called reduction factor.

V.4.2. Simulations

Figure V.14a shows the simulation of the irradiation of 220 nm α-Si with a 32 ns FWHM & 0.20 Jcm^{-2} pulse from a ruby laser for a γ reduction of 0.8. The slab size dZ was taken as 5 nm with a corresponding time step dt of 0.02 ps. The simulation of 90 ns, consumed 48 minutes on an IBM 3081 for a program code in pascal. The first two frames, for 4.4 and 9.4 ns after the top of the laser pulse, correspond with melt-in. The final primary melt depth is 30 nm, slightly less than the experimental result. The primary melt has completely solidified into LG p-Si at t = 14.4 ns, and a l-Si layer of ≃30 nm, with some FG p-Si in it, has formed underneath. The next three frames depict the evolution of a self-propagating l-Si layer. It covers a distance of about 110 nm in approximately 16 ns, with an average velocity of 6 m/s. It never propagates faster than 8 m/s according to the calculations. The corresponding TRR data gave a maximum velocity of 13±2 m/s, while the RBS data indicated a secondary melt depth of ≃190 nm, 50 nm more than in the simulations. The calculations show an explosively propagating layer of ≃40 nm, with an effective l-Si thickness of about 30 nm. This last value is of the same order as measured in the experiments by Thompson et al. (1984), for different conditions. Note that the melt front is sharp while solidification proceeds via a mushy state, a mixture of c- and l-Si. This would result in weak interferences from the front and strong interferences from the rear, as has indeed been observed (see e.g. figs. III.20 and III.21). The calculated average FG p-Si grain diameter is roughly 20 nm, not unreasonable when compared with TEM studies (Narayan and White, 1984; Wood et al. 1984; Narayan et al. 1985).

A schematic picture of the evolution of XCR upon irradiation at 0.46 Jcm^{-2} is shown in figure V.14b. Melting occurs much earlier and deeper now, compared to the case of 0.2 Jcm^{-2}. The maximum primary melt depth of 130 nm is reached approximately 11 ns after the top of the laser pulse. The last two frames, taken at 18.4 and 25.4 ns respectively, contain the actual evolution of XCR. It is striking that the self-propagating l-Si is thinner than for the lower energy-density. The final FG p-Si layer contains grains with a diameter of again roughly 20 nm and extends to a depth of 205 nm. The maximum XCR velocity

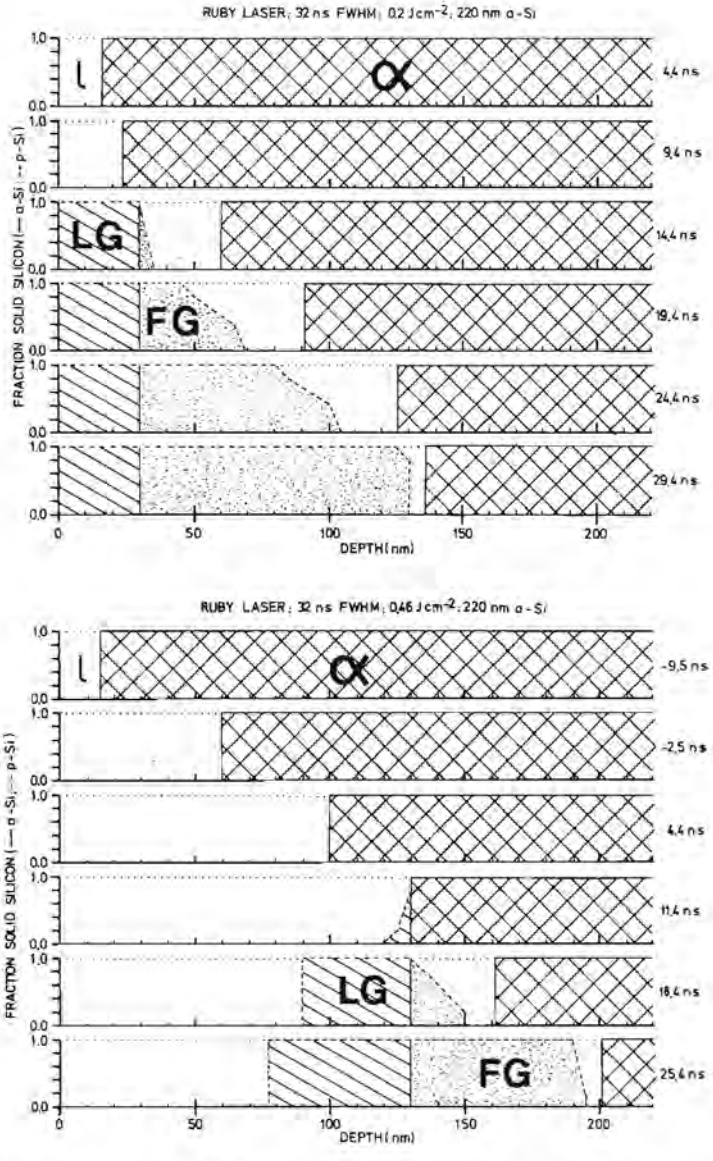

Figure V.14. Simulation of explosive crystallization upon irradiation of 220 nm α-Si with 32 ns FWHM pulses from a ruby laser at (a) 0.20 Jcm^{-2} and (b) 0.46 Jcm^{-2} for $\zeta = 7$ K/(m/s), $\gamma \simeq 0.32$ Jm^{-2}, DZ = 5 nm, and dt = 0.02 ps. The cross-hatched region represents α-Si, the dotted area stand for FG p-Si and the shaded region for LG p-Si.

is $\simeq$ 9 m/s, slightly higher than in the simulation previously discussed. Unfortunately it is not possible to compare this value with an experimental one because the interferences from the self-propagating l-Si are shielded by the primary melt for this energy-density. This situation is also encountered in the simulations, XCR is already decaying at t = 25.4 ns while there is still a l-Si layer of more than 20 nm present at the surface. The simulated LG and the FG p-Si thicknesses are within the error margins of the values determined by RBS. The increase of the XCR velocity with increasing energy-density has also been observed in other experiments (Lowndes et al.1987).

The simulations show that heterogeneous nucleation could be the driving mechanism of explosive crystallization. The agreement between the ruby laser experiments and the simulations is good at higher energy-densities but not around 0.2 Jcm^{-2}. This is not surprizing if one considers that the reflectivity reduction measured at low energy-densities will greatly influence the experimental results. The effect of the reduced reflectivity diminishes at higher energy-densities as can be seen in figure III.23d. Moreover, the XCR front covers a large distance at low energy-densities. In the experiment this inevitably leads to the build up of a considerable Cu concentration at the solidification front of the explosively propagating l-Si layer, which can severely influence the final FG p-Si thickness. Experiments by Lowndes et al. (1987) clearly show that the secondary melt depth in Cu and Ge implanted samples can exceed that in Si implanted samples by more than 100 nm. The extension of XCR also depends on the value and behaviour of ζ. The use of a symmetrical relation for ζ in the simulations causes a superheating of several tens of Kelvin, which reduces the nucleation rate. A simulation with $\zeta_{melt} = 0$ K/(m/s) yielded a secondary melt depth of 190 nm and an average grain diameter of 11 nm for the conditions of figure V.14a. These results are in excellent agreement with the experiments, which indicates that the asymmetry in the velocity-superheating/undercooling relation is important for the simulation of XCR.

Apart from experimental and theoretical uncertainties there are also numerical difficulties involved in the simulation of XCR. It is clear that these simulations depend on a correct representation of the interfaces. Unfortunately

there is no real interface in a calculation with discrete slabs. The result will therefore be influenced by the slab size.

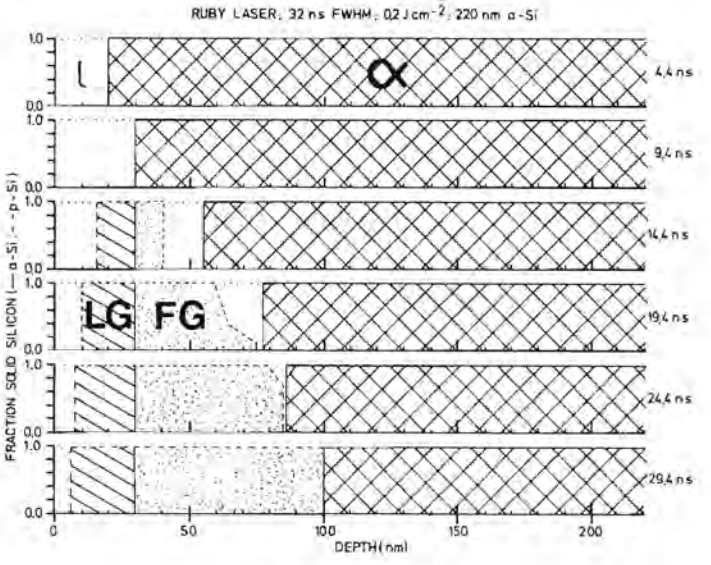

Figure V.15. Simulation of explosive crystallization for the circumstances of figure V.14a but now for a slab size DZ of 10 nm.

Figure V.15 shows a simulation equivalent to that in figure V.14a but now for a subdivision into elements of 10 nm instead of 5 nm. The solidification is rather different in this case. The FG p-Si extends 100 nm, 40 nm less than with the 5 nm slabs. The self-propagating l-Si layer is thinner and its velocity lower. A reduction of the slab size to 2.5 nm is very unpractical since this would give a total computation time of more than six hours for just one set of parameters values. Another difficulty is connected with the treatment of the substrate in the program in combination with the irradiation of a reasonably thin α-Si layer with a ruby laser. The optical penetration depth of the ruby laser wavelength in α-Si is about 200 nm. This means that a respectable fraction of the energy is absorbed in the c-Si substrate for layer thicknesses of this order. Therefore, one has to treat at least a part of the substrate in the same way as the α-Si layer (see section IV.3). This only makes sense if this c-Si layer is on the order of an absorption length which increases the total absorbing film thickness to a few

microns. This approach again leads to unrealistic computing times. The effect of the omission of absorption in the substrate is not very important at high energy-densities for which melting occurs at the beginning of the laser pulse. This abruptly changes the absorption depth from 200 nm to 10 nm, which screens off the substrate. At low energy-densities, however, melting takes place at the end of the laser pulse and the substrate is heated both directly via absorption and indirectly via diffusion. A simulation without direct heating therefore results in a temperature gradient which is too steep compared to reality. The usually large variation of the FG p-Si thickness for energy-densities just above the threshold for surface melting, see figures I.1 and III.24, implies that a slightly steeper temperature gradient can have a large effect on the extension of the XCR front.

How realistic are the basic assumptions and parameter values used? The model assumes that heterogeneous nucleation occurs at the melt front, starting from the moment of maximum melt depth, which gives FG p-Si. The LG p-Si nucleates on top of the FG p-Si. The evidence in favour of heterogeneous nucleation and the arguments against homogeneous nucleation have been given in several places in this thesis and in literature (Devaud and Turnbull, 1985; Tsao and Peercy, 1987; Peercy et al. 1987). The expressions used for heterogeneous nucleation are based on very crude assumptions. A more detailed description has been given by Tsao and Peercy (1987), however, also their model depends heavily on the value of the various parameters such as surface energy and pre-exponential factors. They used the Turnbull approach to obtain the surface energy for the c-Si/l-Si interface, giving $\simeq 0.26$ Jm^{-2}. This value is even less than the experimentally determined lower limit of 0.3 Jm^{-2} (Devaud and Turnbull, 1985). Our simulations yielded reasonable results for a γ reduction of 0.8, corresponding with $\gamma \simeq 0.32$ Jm^{-2} at the melting point of α-Si. The effective value during XCR is somewhat higher since nucleation takes place at the melt front where the temperature is above the melting point of α-Si because of superheating. Simulations in which the LG p-Si is also formed by heterogeneous nucleation did not give any reasonable results. The relatively high temperature in the primary melt prevents nucleation but does not severely reduce the growth

velocity. Without simultaneous growth of LG p-Si, the release of latent heat is not sufficient to sustain XCR except for very low values of the surface energy. In conclusion, the parameter values used are not unrealistic but the theory unfortunately contains too many uncertain factors in order to draw any decisive conclusions concerning the driving mechanism of XCR from the simulations.

The model of Wood and Geist (1986a, 1986b) has the same starting-point: the nucleation of FG p-Si, which acts as a seed for the LG p-Si. However, their model uses a nucleation temperature and nucleation timers to describe XCR, while our model uses physical expressions. Their approach has two disadvantages. Firstly, the values of the nucleation temperature and nucleation times must be universal to give the model any importance. This can hardly be expected, given the various temperature and velocity dependent expressions. Secondly, the formalism makes it possible that FG p-Si is nucleated at various places in the melt. This especially for large primary melt depths with weak temperature gradient in the l-Si.

V.5 Final Discussion

In the statement of the problem, section I.2, we have described many different experimental results on pulsed-laser annealing of α-Si: pure explosive crystallization, pure amorphous regrowth, a spatial mixture of XCR and amorphous regrowth, and internal melting. The results in chapter III have shown that this list must be extended by amorphous regrowth followed by XCR. However, this wide variety of melt and solidification phenomena can now be understood at least qualitatively. Low heating rates lead to bulk nucleation in the α-Si (Roth and Olson, 1987; Roorda et al. 1988). The thus formed c-Si nuclei initiate explosive crystallization upon melting of the remaining α-Si (Bruines et al. 1986b; Lowndes et al. 1987). The temperature gradient in the unmelted material determines whether the α-Si layer is completely or only partially transformed into p-Si by the XCR. High heating rates suppress bulk nucleation in the solid phase and the α-Si melts without showing explosive crystallization (Cullis et al. 1982, 1984; Campisano et al. 1985; Bruines et al. 1986a). In absence of a c-Si seed, solidification starts with growth of α-Si from the interior, followed by growth of α-Si from the surface. A solidification time which exceeds the incubation time, i.e. for low solidification velocities and/or large melt depths, results in the initiation of explosive crystallization during amorphous regrowth (Bruines et al. 1987a, 1987b). If it is the incubation time which exceeds the time to solidify, i.e. for high solidification velocities and/or small melt depths, one observes pure amorphous regrowth (Cullis et al. 1982, 1984; Campisano et al. 1985).

In first instance one would expect that the density of nuclei at the onset of melting scales linearly with time. It is therefore remarkable that the 32 ns FWHM pulses from the ruby laser were long enough to cause nucleation in the solid, while the quasi 18 ns pulses from the frequency-doubled Nd:YAG laser did not show any evidence for that. A shorter pulse duration, however, does not only result in a higher heating rate but also in a higher temperature during the melting phase which can cause the melting of the c-Si embryos. Relaxation ef-

fects as described by Sinke et al. (1987) could also play an important role on this time scale.

The understanding of amorphous regrowth from both the interior and the surface has increased in both a qualitative and a quantitative way. We have shown that the presence of segregating impurities is not necessary for the occurrence of the process. Furthermore a computer model has been developed to simulate amorphous regrowth. The comparison between model calculations and experiments yields a value of 6 ± 2 K/(m/s) for the velocity-undercooling parameter ζ of α-Si. Our experiments indicate that the effect of segregating impurities at the solidification front can be described by an increase in the effective value of ζ. This results in an increasing velocity from the front and a decreasing velocity from the rear. This process stops when both velocities are equal. Another interesting observation is that there is an incubation time for the nucleation of p-Si at the α-Si/c-Si interface of $\simeq$20 ns ($\simeq$10 ns) at an interface velocity of 1 m/s (0.5 m/s). It is the combination of this incubation time and the effect of segregating impurities on the solidification velocities, which caused the total absence of p-Si in the experiments by Cullis et al. (1982, 1984) and Campisano et al. (1985). The question why growth of α-Si can initiate from the surface is, however, still unresolved. It would e.g. be interesting to know if it is related with the presence of a native oxyde layer.

The generally good agreement in this thesis between the heat-flow calculations and the measurements show that heat-flow calculations have matured. It is now possible to extract the relevant parameters and thus be able to compare experiments performed under different experimental conditions. For instance, our calculations indicate that the solidification velocity is mainly determined by the thickness of the unmelted α-Si layer when working on substrates such as c-Si and sapphire, which act as a heat sink, and with pulses in the nanosecond regime. This means that the pulse duration has only a minor effect on the solidification velocity and that one must compare on basis of equal remaining α-Si layer thickness. If unknown, it can be calculated fairly accurately. Moreover, heat-flow calculations can be used to test theories concerning bulk nucleation, amorphous regrowth, and superheating/undercooling or to deter-

mine the constants associated with them. It is clear that a heat-rate dependent melting point of α-Si, as suggested by Sinke et al. (1987), would severely complicate matters. However, it could also be the solution to the different melting points found for pulsed- and cw-laser annealing.

In summary, the initiation of explosive crystallization and amorphous regrowth is now understood in a semi-quantitative way i.e. there are still parameters to be determined, such as the asymmetry in the velocity-undercooling/superheating relation, and the first principles are provided to model all of the melt and solidification phenomena encountered.

References Chapter V

Bruines, J.J.P., van Hal, R.P.M., Boots, H.M.J., Sinke, W., and Saris, F.W. (1986a); Appl. Phys. Lett. **48**, 1252.

Bruines, J.J.P., van Hal, R.P.M., Boots, H.M.J., Polman, A., and Saris, F.W. (1986b); Appl. Phys. Lett. **49**, 1160.

Bruines, J.J.P., van Hal, R.P.M., Koek, B.H., Viegers, M.P.A., and Boots, H.M.J. (1987a); Appl. Phys. Lett. **50**, 507.

Bruines, J.J.P., van Hal, R.P.M., Koek, B.H., Viegers, M.P.A., and Boots, H.M.J. (1987b); MRS Symp. Proc. Vol. **74**, 91.

Campisano, S.U., Jacobson, D.C., Poate, J.M., Cullis, A.G., and Chew, N.G. (1985); Appl. Phys. Lett. **46**, 846.

Cullis, A.G., Chew, N.G., Webber, H.C., Smith, D.J. (1984); J. Crystal Growth **68**, 624.

Cullis, A.G., Webber, H.C., and Chew, N.G. (1982); Appl. Phys. Lett. **40** , 998.

Devaud, G. (1986); private communication.

Devaud, G. and Turnbull, D. (1985); Appl. Phys. Lett. **46**, 844.

Lowndes, D.H., Pennycook, S.J., Jellison Jr., G.E.., Withrow, S.P., and Mashburn, D.N. (1987); J. Mat. Res. **2**, 648.

Narayan, J., Fathy, D., Oen, O.S., and Holland, O.W. (1984); Materials Letters **2**, 211.

Narayan, J., and White, C.W. (1984); Appl. Phys. Lett. **44**, 35.

Narayan, J., White, C.W., Aziz, M.J., Stritzker, B., and Walthuis, A. (1985); J. Appl. Phys. **57**, 564.

Roorda, S., Saito, S., and Sinke, W.C. (1988); submitted to Phys. Rev. Lett.

Peercy, P.S., Thompson, M.O., and Tsao, J.Y. (1987); Mat. Res. Soc. Symp. Proc. **74**, 15.

Sinke, W.C., Warabisako, T., Miyao, M., Tokuyama, T., Roorda, S., and Saris, F.W. (1988); Mat. Res. Soc. Symp. Proc., Boston U.S.A., December 1987, to be published.

Thompson, M.O., Galvin, G.J., Mayer, J.W., Peercy, P.S., Poate, J.M., Jacobson, D.C., Cullis, A.G., and Chew, N.G. (1984); Phys. Rev. Lett. **52** , 2360.

Tsao, J.Y. and Peercy, P.S. (1987); Phys. Rev. Lett. **58**, 2782.

Wood, R.F. and Geist, G.A. (1986); Phys. Rev. B **34**, 2606 & Phys. Rev. Lett. **57**, 873.

Wood, R.F., Lowndes, D.H., and Narayan, J. (1984); Appl. Phys. Lett. **44** , 770.

SUMMARY

Pulsed-lasers are frequently used nowadays for materials processing and data recording. These applications are often based on inducing phase changes such as melting, crystallization, and amorphization. The use of short light pulses, with correspondingly high heating and cooling rates, makes it possible to prepare and study materials in a state far from equilibrium. Silicon has since long been a model system for these studies because of its high purity, industrial use, and simplicity compared to compounds. Recently this interest concentrated on the annealing behaviour of the amorphous phase of silicon. This resulted in the discovery of a wide variety of melt and solidification phenomena, obtained under different experimental conditions, which were not well understood i.e. there was no framework which enabled the comparison between experiments or that could predict the outcome for given parameters. This thesis presents a systematic experimental study of pulsed-laser irradiation of mainly amorphous silicon, supported by phase change models and computer simulations.

Chapter I begins with a short general introduction, which is followed by a description of the basic, and often apparently contradictory, experimental observations found in literature. Two phenomena are discussed at length: explosive crystallization, a self-sustained crystallization process, and amorphous regrowth whereby solidification proceeds via growth of amorphous silicon from both the interior and the surface. The chapter continues with a presentation of the relevant optical and thermophysical properties of silicon, of which the melting point and latent heat of the amorphous phase are still under discussion. Finally we give a description of the kinetic theory for phase changes. The velocity-superheating/undercooling relation is introduced and its symmetry properties with respect to melting or solidification are discussed. Furthermore we present the fundamentals for bulk and interface nucleation in an undercooled melt or a metastable solid. It is shown that bulk nucleation in the undercooled melt of amorphous silicon is completely negligible. Both other mechanisms can not be ruled out a-priori.

In chapter II we give a description of the experimental set-up used. At first we give the basic considerations and elements for melting silicon. The importance of having a uniform spatial energy-density profile is discussed as well as the way in which we obtained this goal. The second part of the chapter presents the time-resolved reflectivity set-up. We discuss the necessity and difficulties of nanosecond time resolution, single-frequency probe lasers and absolute reflectivity measurements. The discussion of the temporal resolution returns in the description of the electronics used to record the fast phenomena in real-time. This is followed by the measurement of the overall time resolution of the system by recording the response after excitation with a 120 picosecond light pulse. The chapter ends with a discussion of the preparation and characterization of amorphous silicon.

The third chapter starts with the presentation of our conceptual framework describing the importance of the various experimental parameters and their consequences. It is shown that the thickness of the unmelted amorphous

silicon must be used as a reference for comparing experiments. The bulk of chapter III consists of the presentation of the experimental data. Firstly the irradiation with a 7.5 ns FWHM pulse from a frequency-doubled Nd:YAG laser of 225 nm, Cu implanted, and 230 nm, Si implanted, amorphous silicon. The measurements indicate that solidification proceeds via amorphous regrowth from the interior and the surface, followed by the formation of polycrystalline silicon from within the layer. The segregating Cu effectively hampers crystallization.

Secondly we present the results upon irradiation of 230 nm, Si implanted, amorphous silicon with an 18 ns pulse from again the frequency-doubled Nd:YAG laser. The more than doubled pulse duration has only a small effect on the solidification; for this layer thickness the heat-flow is dominated by the amorphous silicon layer and not by the pulse duration of the laser. Once more, solidification proceeds via amorphous regrowth from the interior and the surface followed by nucleation of polycrystalline silicon.

The experiments with the Nd:YAG laser are concluded by the discussion of the data on the irradiation of 440 nm, Cu implanted, amorphous silicon on 60 nm crystalline silicon on sapphire. The transparency of the sapphire enabled us to record the onset of amorphous regrowth from both the front and the rear, as well as the moment of nucleation of explosive crystallization.

The last section describes the annealing of 225 nm, Cu implanted amorphous silicon with 32 nm FWHM pulses from a ruby laser. The data show only explosive crystallization. From the behaviour of the reflectivity, both in time and with energy-density, it is inferred that this explosive crystallization is ignited by crystalline silicon nuclei in the primary melt, presumably formed in the solid phase during heating by the relatively long ruby laser pulse.

Chapter IV is devoted to the concept of heat-flow calculations as well as to melting and solidification models. It starts with the presentation of the general differential equation and several of its approximative solutions. The differential equation is transformed into a finite difference form to cope with phase changes and temperature and/or position dependent parameters. Moreover we present the basic expressions for the incorporation of superheating and undercooling. This section is followed by various test performed to verify the algorithm used. The chapter continues with a description of the models for amorphous regrowth from the surface and for bulk respectively interface nucleation in the melt i.e. for explosive crystallization, developed by us. It is shown that the outcome of these models depends rather strongly on the slab size, so that it is sometimes necessary to extrapolate. Finally we discuss and test the computer model developed by Wood and Geist to describe explosive crystallization, which was given to us.

The fifth and final chapter gives the synthesis of the experiments and the calculations. It starts with a comparison between the measured and the simulated time-resolved reflectivity signals for amorphous regrowth from the surface. The experiments can be simulated rather well for a velocity-undercooling parameter ζ of 6 ± 2 K/(m/s). Furthermore it can be concluded that the segregating Cu increases the effective value of ζ, either directly or via a melting point depression. It is very likely that all segregating elements will show this effect.

Next, the derived value for ζ is used to calculate the solidification velocity, both from the rear and the surface, versus time. The combination of the experimental data with the simulations reveals the presence of a barrier for the nucleation of crystalline silicon at a moving liquid-/amorphous silicon interface. This so called incubation time amounts 10 ns at 0.5 m/s and 20 ns at 1 m/s. It is therefore unlikely that interface nucleation can initiate explosive crystallization without a preceeding amorphous regrowth phase.

The existence of a nucleation barrier is further elucidated by an experiment on crystalline silicon on sapphire. The sapphire act as an amorphous substrate at total melt-through, and the liquid silicon is forced to cool down below its crystalline melting point. It is shown that amorphous regrowth starts at a temperature of 1470±40 K, in excellent agreement with the 1460±25 K previously found for the melting point of amorphous silicon. The amorphous regrowth is followed by explosive crystallization after a certain incubation time. TEM pictures show fine-grain polycrystalline silicon at the front and large-grain polycrystalline material at the rear of the sample. This order, which is reversed with respect to "normal" explosive crystallization, points towards nucleation at the upper front, with the lowest solidification velocity.

Chapter V ends with the presentation of the simulation of explosive crystallization via interface nucleation in absence of an incubation time. It is stated that, after initiation by another mechanism, interface nucleation could be the driving process for explosive crystallization. The symmetry of the velocity-superheating/undercooling relation is of importance here, the experiments are simulated perfectly for a superheating which is negligible, i.e. for $\zeta_{melt} \simeq 0\ K/(m/s)$. Finally we discuss the basic differences between our model and the one presented by Wood and Geist.

SAMENVATTING

Gepulste lasers worden tegenwoordig vaak ingezet bij het bewerken van materialen en het opslaan van gegevens. Deze toepassingen zijn meestal gebaseerd op het induceren van fase-overgangen zoals smelten, kristalliseren en amorfiseren. Het gebruik van korte laserpulsen en de daarmee gepaard gaande hoge opwarm- en afkoelsnelheden, maakt het mogelijk om materialen in een toestand te brengen en te bestuderen die ver uit evenwicht is. Sinds lange tijd wordt silicium als een modelsysteem beschouwd voor de bestudering van deze toestand vanwege zijn zuiverheid, industrieel belang en relatief eenvoudige kristalstructuur. Recentelijk heeft het onderzoek zich geconcentreerd op silicium in zijn amorfe toestand. Dit heeft geleid tot de ontdekking van vele verschillende smelt- en stolverschijnselen, verkregen onder evenzovele experimentele omstandigheden en ogenschijnlijk zonder enig verband bij gebrek aan een referentiekader. Dit proefschrift bevat de resultaten van een systematisch uitgevoerde experimentele studie van de bestraling van voornamelijk amorf silicium met een laserpuls, ondersteund door modelvorming en computersimulaties.

Het eerste hoofdstuk begint met een korte algemene introduktie die gevolgd wordt door een historisch overzicht van de, soms tegenstrijdig lijkende, resultaten in de literatuur. Twee phenomenen komen daarbij uitvoerig aan bod: (1) explosieve kristallisatie, een zichzelf in stand houdend kristallisatieproces, en (2) amorfe teruggroei waarbij stolling plaatsvindt middels groei van amorf silicium vanaf de ondergrens en de bovengrens van de smelt. Hoofdstuk I gaat verder met een opsomming en analyse van de relevante optische en thermodynamische parameters van silicium, waarbij opgemerkt dient te worden dat de smelttemperatuur en smeltwarmte van amorf silicium nog steeds ter discussie staan. Als laatste wordt de kinetische theorie voor fase-overgangen uitvoerig beschreven. De relatie tussen de snelheid van het grensvlak waar de fase-overgang plaatvindt en de daar optredende oververhitting of onderkoelings wordt geintroduceerd en we bespreken zijn symmetrie ten opzichte van smelten of stollen. Bovendien presenteren we de fundamenten van volume- en grensvlaknucleatie in zowel een onderkoelde vloeistof als in een metastabiele vaste stof. Het zal worden aangetoond dat men volumenucleatie in de onderkoelde smelt van amorf silicium volkomen kan verwaarlozen. De andere mogenlijkheden kunnen niet a-priori uitgesloten worden.

Hoofdstuk II beschrijft de manier waarop de experimenten zijn uitgevoerd. In het eerste deel worden de belangrijkste facetten van de opstelling voor het smelten van silicium besproken. Speciale aandacht krijgt daarbij het belang van een ruimtelijk uniforme energieverdeling en de manier waarop dat door ons verwezenlijkt is. Het tweede deel van het hoofdstuk bevat de bespreking van de opstelling voor het meten van het verloop van de reflectie in de tijd. Met name wordt uitgelegd dat dit soort experimenten een tijdresolutie in het nanosecondegebied vereist, hetgeen hoge eisen aan de electronica stelt en de inzet van z.g. één-frekwentie testlasers noodzakelijk maakt. Bovendien worden de mogelijkheden en moeilijkheden van het doen van absolute reflectie metingen besproken. De kwestie van de tijdresolutie komt weer terug in de beschrijving

van het electronische gedeelte van de opstelling. De uiteindelijke tijdsresolutie van het totale systeem wordt getest door de respons na excitatie met een lichtpuls van 120 picoseconde te analyseren. Het hoofdstuk wordt afgesloten met een bespreking van de productie en karakterisering van de gebruikte amorf siliciumpreparaten.

Het derde hoofdstuk begint met de presentatie van een referentiekader waarmee al onze experimenten met elkaar vergeleken kunnen worden. Zo moet bijvoorbeeld de dikte van de ongesmolten amorfe siliciumlaag als basis genomen moet worden bij het vergelijken van de verschillende metingen. Vervolgens worden alle experimenten uitvoerig beschreven. Ten eerste de resultaten verkregen door bestraling met een 7.5 ns puls van een frequentie verdubbelde Nd:YAG laser van 225 nm, met Cu geimplanteerd en 230 nm, met Si geimplanteerd, amorf silicium. De resultaten wijzen erop dat stolling in eerste instantie plaats vindt door groei van amorf silicium aan zowel het achtervlak als het voorvlak van de smelt. Dit proces wordt gevolgd door de vorming van polykristallijn silicium vanuit het binnenste van de laag. Het Cu, dat zich ophoopt aan de stolfronten, remt de vorming van het polykristallijne materiaal.

De tweede klasse van experimenten betreft het bestralen van het reeds eerder genoemde Si geimplanteerde materiaal met de Nd:YAG laser doch nu voor een pulsduur van 18 ns. Deze meer dan verdubbelde pulsduur heeft slechts een gering effect op de stolling. Voor de gegeven omstandigheden wordt de afvoer van warmte gedomineerd door de dikte van de amorfe silicium laag en niet door de pulsduur van de laser.

De serie metingen met de Nd:YAG laser wordt afgesloten met de bestraling van 440 nm, Cu geimplanteerd, amorf silicium op 60 nm kristallijn silicium op saffier, met een 7.5 ns puls. Weer vindt de stolling plaats via groei van amorf silicium vanaf onder- en bovenkant, zij het met een snelheid die ongeveer gehalveerd is t.o.v. de twee voorgaande situaties. Ook nu wordt de groei onderbroken door de vorming van polykristallijn silicium. Het is mogelijk om beide stolverschijnselen van twee kanten in de tijd vast te leggen, aangezien het saffieren substraat transparant is. Op deze wijze zijn de verschillende tijdstippen van amorfe teruggroei en de vorming van polykristallijn silicium bepaald.

Hoofdstuk III wordt afgesloten met de presentatie van 225 nm Cu geimplanteerd amorf silicium met een 32 ns puls van een robijn laser. De stolling verloopt hierbij meteen via explosieve kristallisatie, zonder dat daar amorfe teruggroei aan voorafgaat. Uit het gedrag van de reflectie, zowel in de tijd als versus energiedichtheid, valt af te leiden dat er zich kristallijne kiemen in de vloeistof bevinden. Deze kiemen, die waarschijnlijk nog in de vaste stof gevormd zijn tijdens de opwarmfase van de relatief lange laserpuls, zijn verantwoordelijk voor het starten van explosieve kristallisatie.

Hoofdstuk IV is gewijd aan warmtestroom berekeningen en fase-overgang modellen. Eerst wordt de algemene differentiaalvergelijking voor het warmtestroomprobleem gegeven, gevolgd door enige analytische oplossingen die onder sterk vereenvoudigde omstandigheden gevonden kunnen worden. Om het probleem in zijn volle complexiteit aan te kunnen moet gebruik gemaakt worden van computersimulaties. Daartoe wordt de differentiaalvergelijking omgezet in

een eindige elementen vorm. Daarbij horen nog additionele vergelijkingen om fase-overgangen te beschrijven, met name die in aanwezigheid van oververhitting en onderkoeling aan het fasefront. Daarna volgt een sectie waarin de diverse aspecten van het computer model getest worden.

Het hoofdstuk wordt voortgezet met de beschrijving van de door ons ontwikkelde modellen voor amorfe teruggroei van het oppervlak en volume- respectievelijk grensvlaknucleatie d.w.z. voor explosieve nucleatie. De bereikte resultaten hangen sterk af van de stapgrootte in de diepte zodat soms van een extrapolatie gebruik gemaakt moet worden. Tenslotte bespreken we het computermodel voor explosieve kristallisatie dat wij van de heren Wood en Geist gekregen hebben.

Het vijfde en laatste hoofdstuk geeft de synthese tussen de experimenten en de berekeningen. Eerst wordt een vergelijking gemaakt tussen het gemeten en het berekende verloop van de reflectie in de tijd. De experimenten zonder Cu kunnen redelijk goed gesimuleerd worden voor een snelheids-onderkoelings parameter ζ van 6 ± 2 K/(m/s). Bovendien kan er geconcludeerd worden dat het zich aan het stolfront ophopende Cu ogenschijnlijk de waarde van ζ verhoogd. Dat laatste kan zowel een echte verhoging zijn als een effectieve verhoging ten gevolge van een smeltpuntsverlaging. Het is zeer waarschijnlijk dat alle zich aan het stolfront ophopende elementen eenzelfde effect vertonen.

De in het eerste gedeelte van hoofdstuk V bepaalde waarde van ζ wordt vervolgens gebruikt om beide stolsnelheden, zowel die van het voorvlak als die van het achtervlak, uit te kunnen zetten tegen de tijd. Een vergelijking tussen de experimenten en de berekeningen laat zien dat er een barriere bestaat voor nucleatie van kristallijn silicium aan een bewegend vloeibaar/amorf silicium grensvlak. Deze z.g. incubatietijd bedraagt 10 ns bij 0.5 m/s en loopt op tot 20 ns bij 1 m/s. Het kan daarom uitgesloten worden dat grensvlaknucleatie verantwoordelijk is voor het starten van explosieve nucleatie, zonder dat daar amorfe teruggroei aan vooraf is gegaan.

Het bestaan van een nucleatiebarriere wordt verder aangetoond d.m.v. een experiment met kristallijn silicium op saffier. Saffier is als een amorf substraat bij totaal doorsmelten, het vloeibare silicium wordt daardoor gedwongen om af te koelen tot beneden zijn kristallijne smeltpunt. Uiteindelijk vindt stolling plaats via amorfe terugggroei bij een temperatuur van 1470 ± 40 K, in goede overeenstemming met het gevonden smeltpunt voor amorf silicium van 1460 ± 25 K. Na een zekere incubatietijd wordt het stolproces overgenomen door explosieve kristallisatie. TEM foto's tonen fijnkorrelig silicium aan het oppervlak met daaronder grofkorrelig materiaal. Deze volgorde, die geinverteerd is t.o.v. het "normale" explosieve kristallisatie proces, wijst op nucleatie aan het bovenste grensvlak, met de laagste stolsnelheid.

Hoofdstuk V wordt afgesloten met de bespreking van de simulatie van explosieve kristallisatie middels nucleatie aan het grensvlak, zonder incubatietijd. Aangetoond wordt dat, na ontsteking door een ander mechanisme, nucleatie aan het vloeibaar/amorf grensvlak de drijvende kracht achter explosieve nucleatie zou kunnen zijn. De symmetrie van de relatie tussen de snelheid van het fasegrensvlak en de daar optredende oververhitting of onderkoeling is van belang voor een correcte weergave van de werkelijkheid. De experimenten worden perfect gesimuleerd als de oververhitting verwaarloosbaar

is, ofwel $\zeta_{melt} \simeq 0\ K/(m/s)$. Als laatste worden de belangrijkste verschillen tussen ons model voor explosieve kristallisatie en dat verkregen via de heren Wood en Geist besproken.

DANKWOORD

Allereerst gaat mijn dank uit naar de directie van het Natuurkundig Laboratorium van de N.V. Philips Gloeilampenfabrieken te Eindhoven voor haar toestemming de resultaten van het onderzoek in een proefschrift te verwerken. In het bijzonder wil ik dr. A.R. Miedema bedanken voor zijn voortdurende aanmoediging en ondersteuning.

Dr. Q.H.F. Vrehen dank ik voor de vele uren die hij aan het uitpluizen van de experimenten, het corrigeren van het proefschrift en mijn vorming als physicus besteed heeft. Steeds wist hij mijn aanvallen van jeugdig enthousiasme te doorstaan en op de juiste wijze te temperen en te relativeren. Daarenboven zag hij telkens weer kans om de grote lijn vast te houden en de waardevolle dingen uit de rijstebrijberg van resultaten te halen als ik de moed al had opgegeven.

Theoretische ondersteuning kwam van de kant van dr. Henk Boots. De vele, vele uren van discussie zijn een wezenlijke bijdrage geweest tot het welslagen van het onderzoek. Bovendien nam hij steeds op meesterlijke wijze de rol van advokaat van de duivel op zich.

De vele experimenten zijn deskundig en zorgvuldig uitgevoerd door ing. René van Hal waarvoor ik hem van harte wil bedanken. In de vijf jaren van onze samenwerking heb ik steeds gebruik kunnen maken van zijn experimentele vaardigheden en kritische geest.

Verder is er steeds een vruchtbare samenwerking geweest met dr. Wim Sinke, drs. Albert Polman, drs. Sjoerd Roorda en prof. dr. F.W. Saris van het F.O.M. instituut voor Atoom en Molecuul Physica (AMOLF) te Amsterdam, hun enthousiasme en collegialiteit heeft mij altijd veel goed gedaan.

Dr. ir. J. Politiek en Dr. H.J. Ligthart ben ik zeer erkentelijk voor de vaak langdurige implantaties die zij voor mij gedaan hebben. De heren van de RBS, dr. Leo van IJzendoorn en ing. Martin Willemsen, waren altijd behulpzaam bij de karakterisatie. Dr. Thijs Viegers, ing. Bert Koek en Corrie Bulle verdienen mijn dank voor het vaak moeilijke TEM werk dat zij hebben uitgevoerd.

Al de leden van de koffiehoek en de literatuurgroep ben ik dank verschuldigd voor de "education permanente" die mij voor een (verdere) vernauwing van het bewustzijn heeft behoed en als laatste wil ik diegenen bedanken die achter de schermen van het Nat. Lab. hebben meegewerkt aan het onderzoek. Zonder hen was het onmogelijk geweest dit resultaat te bereiken.

LEVENSLOOP

11 januari 1958:	geboren in Alphen a/d Rijn
1976:	atheneum-B diploma van het Bonaventura College te Leiden
4 januari 1980:	getrouwd met Johanna Maria de Klerk
28 januari 1982:	natuurkundig ingenieur aan de Technische Hogeschool te Delft
4 april 1982:	in dienst als wetenschappelijk medewerker bij het Natuurkundig Laboratorium van de N.V. Philips Gloeilampenfabrieken in Eindhoven
12 juli 1984:	geboorte van Abraham Johannes Bruines
15 oktober 1986:	geboorte van Anna Elisabeth Maria Bruines
15 februari 1988:	ingénieur de recherche bij de Laboratoires d'Electronique et de Physique Appliquée in Limeil-Brévannes, Frankrijk

Stellingen

behorende bij het proefschrift

TIME-RESOLVED STUDY OF SOLIDIFICATION PHENOMENA ON PULSED-LASER ANNEALING OF AMORPHOUS SILICON

door

Johannes Josef Pancrasius (Joop) Bruines

in het openbaar te verdedigen op
dinsdag 25 oktober 1988 te 16.00 uur
in het Auditorium van de T.U. Eindhoven

I

De aanname voor de distributiefunctie van hete electronen in halfgeleiders van Hänsch en Miura-Mattausch leidt er onbedoeld toe dat alle stromen evenwijdig aan het electrische veld staan. Gelukkig is dat niet van invloed op de gepresenteerde resultaten.

W. Hänsch en M. Miura-Mattausch, Journal of Applied Physics **60** , 650 (1986).

II

Tränkle et al. (1987) gebruiken ten onrechte een tweedimensionale theorie in hun artikel over de bandgap renormalisatie in quantumputten.

G. Tränkle, H. Leier, A. Forschel, H. Haug en C. Ell, Physical Review Letters **58**, 419 (1987).

III

Bij de bepaling van de invloed van As en In verontreinigingen op het smelt- en stolgedrag van Si onder bestraling met een laserflits door Peercy et al. (1985), wordt het effect van de hoge As en In concentraties op de absorptie ten onrechte onvermeld gelaten.

P.S. Peercy, M.O. Thompson en J.Y. Tsao, Applied Physics Letters **47** , 244 (1985)

P.S. Peercy, M.O. Thompson, J.Y. Tsao en J.M. Poate, Materials Research Society Symposium Proceedings **51**, 125 (1985)

IV

De bewering van Kobayashi et al. (1982) dat de variatie in de Hall mobiliteit van de electronen in Si op saffier een gevolg is van het effect van spanningen op de effectieve massa is fout.

Y. Kobayashi, M. Nakamura en T. Suzuki, Applied Physics Letters **40** , 1040 (1982)

V

Het gebruik van een diffusieprofiel voor de Al concentratie tussen een GaAs en een AlAs laag in een superrooster door Jusserand et al. (1985) is in strijd met hun eigen conclusies.

B. Jusserand, F. Alexandre, D. paquet en G. Le Roux, Applied Physics Letters **47**, 301 (1985)

VI

Sapriel et al. (1983) houden geheel ten onrechte geen rekening met de oxidatie van het AlGaAs oppervlak bij de bepaling van de elastische konstantes voor oppervlakte golven.

J. Sapriel, J.C. Michel, J.C. Toledano, R. Vacher, J.Kervarec en A. Regreny, Physical Review B **28**, 2007 (1983)

VII

De instelling van nog meer mogelijkheden tot het verkrijgen van reductie op een treinkaartje zal leiden tot minder in plaats van tot meer rendement voor de Nederlandse Spoorwegen.